



D I S S E R T A T I O N

Lattice Boltzmann Modeling and Simulation
of Incompressible Flows in Distensible
Tubes for Applications in Hemodynamics

ausgeführt zum Zwecke der Erlangung des akademischen Grades eines
Doktors der technischen Wissenschaften unter Leitung von

Ao.Univ.Prof. Dipl.-Ing. Dr.techn. Felix Breitenecker
Institut für Analysis und Scientific Computing

eingereicht an der Technischen Universität Wien
bei der Fakultät für Mathematik und Geoinformation

von

Dipl.-Ing. Xenia Descovich

Matrikelnummer: 0126114

Hadikgasse 146/6

1140 Wien

Wien, im Oktober 2012

Kurzfassung

Aufgrund der Zunahme von kardiovaskulären Erkrankungen in Industrieländern in den letzten Jahren besteht starkes Interesse daran, die hämodynamischen Vorgänge im Herzkreislaufsystem zu verstehen. Viele Forschungsarbeiten befassen sich mit den Charakteristiken des Blutflusses und versuchen, diese mit dem Entstehen und der Entwicklung von Gefäßkrankheiten in Verbindung zu bringen. Nachdem experimentelle Methoden schwierig, oft invasiv und teilweise nicht durchführbar sind, greift man auf mathematische Modellierung und numerische Simulation zurück, um ein besseres Verständnis von Auswirkungen verschiedenster hämodynamischer Faktoren auf den Blutfluss zu erhalten.

Die Mehrheit der Studien in numerischer Strömungsmechanik nimmt starre Gefäßwände an. Speziell bei Untersuchungen des Blutflusses in großen Arterien sollten die Elastizität der Blutgefäße sowie die Wechselwirkung zwischen Fluid und Gefäßwand jedoch miteinbezogen werden. Die Behandlung solcher Fluid-Struktur-Interaktionen stellt eine große Herausforderung dar.

Die vorliegende Arbeit stellt eine präzise und effiziente Methode zur Modellierung und Simulation von inkompressiblem Fluss in dehnbaren Rohren und der Interaktion zwischen Fluss und Rohrwand vor, mit speziellem Fokus auf hämodynamische Anwendungen. Die Lattice Boltzmann Methode wurde verwendet als Alternative zu klassischen Verfahren zur Lösung strömungsmechanischer Probleme. Eine neue Randbedingung wurde eingeführt, welche eine kontinuierliche Verschiebung der Gefäßwand ermöglicht und somit Diskretisierungsfehler reduziert. Des Weiteren wurde die Methode weiterentwickelt, um den Blutfluss in Stents und die Auswirkungen unterschiedlicher Stenteigenschaften untersuchen zu können. Der gesamte Algorithmus wurde in der Programmiersprache C implementiert. Die durchgeführten numerischen Experimente an artifiziellen Gefäßsegmenten lieferten qualitative Aussagen über den Blutfluss.

Die erhaltenen Resultate zeigen das erwartete physikalische Verhalten und bestätigen die Anwendbarkeit und die Effizienz der Methode. In den Simulationen wurde eine konstante Austrittsrandbedingung verwendet. Auch wenn diese Randbedingung für stationäre Probleme akzeptabel ist, so kann sie für zeitabhängigen Fluss störende Reflexionen hervorrufen, welche die Lösung verfälschen. Um dieses Problem zu umgehen, wird eine realistischere Randbedingung, welche den Lattice Boltzmann Algorithmus mit einem Windkesselmodell koppelt, vorgeschlagen.

Vorbereitende numerische Experimente beinhalten eine Anwendung, die von klinischem Interesse ist, nämlich die Änderung des Flussfeldes aufgrund eines eingesetzten Stents.

Die entwickelte Methodik überzeugt durch ihre Einfachheit und Effizienz, während sie gleichzeitig ermöglicht, Druck und Fluss in elastischen Gefäßen zu ermitteln. Bevor die Methode jedoch für medizinische Prognosen oder zur Optimierung von Stentdesigns verwendet werden kann, muss sie weiter verfeinert werden. Des Weiteren muss das Modell durch Vergleich mit realen Messdaten validiert werden.

Abstract

Due to the increase of cardiovascular diseases in industrialized countries in the past years, there is a strong interest in understanding the hemodynamic processes in the cardiovascular system. A lot of research has been done to study the characteristics of the blood flow and to correlate these to the development of vascular diseases. Since experimental methods are difficult, limited, and often invasive, mathematical modeling and numerical simulations are used to better understand the effects of several hemodynamic factors on the blood flow.

Most studies in computational fluid dynamics assume that the vessel walls are rigid. However, especially when studying the blood flow in large arteries, it is of particular importance to incorporate the elasticity of the vessel and its interaction with the fluid. The treatment of such fluid-structure interaction problems is a real challenge.

This thesis presents an accurate and computationally efficient approach for modeling and simulating incompressible flow in distensible tubes and its interaction with the tube wall, with particular focus on applications in hemodynamics. The developed lattice Boltzmann method has been used as a competitive alternative approach to conventional numerical methods. A novel boundary condition is introduced allowing a continuous displacement of the wall, which reduces discretization errors. The method has been extended to model the blood flow through stents and to study the effect of different stent properties. The overall algorithm has been implemented in the programming language C and numerical experiments on artificial vessel segments have been extensively carried out providing qualitative results.

The results show the expected physical behavior and prove the feasibility and the efficacy of the methodology. In the simulations, a constant outflow boundary condition has been used. Even if this condition is reasonable for steady-state problems, in time-dependent flows it may cause spurious reflections spoiling the solution. In order to circumvent this problem, a more realistic boundary condition coupling the lattice

Boltzmann algorithm with a Windkessel model is suggested. Preliminary numerical experiments include a case of clinical interest: the modification of the flow field due to stent insertion.

The presented methodology offers a valuable tool: it is simple and computationally efficient while at the same time able to predict waveforms and pressure fields in arteries. However, before the elaborated method can be used to study physiological flows in a predictive way, an additional effort is required and the parameters contained in the model have to be identified by validation against measurement data.

Acknowledgments

I would like to thank Prof. Felix Breitenecker, my supervisor at the Vienna University of Technology, for being supportive throughout my doctoral studies. I deeply appreciated the combination of scientific work and community building events within his research group.

I am very grateful to Siegfried Wassertheurer and Manfred Bammer from the AIT Austrian Institute of Technology GmbH for giving me the opportunity to work on my thesis within the AIT, for providing me an effective work environment, and for supporting my scientific exchange abroad. I wish to express my special thanks to my colleagues at the AIT, especially to Johannes Kropf, Bernhard Hametner, Gregor König, Martin Bachler, and Christopher Mayer. They have constantly been a pleasant company throughout the last years.

During my doctoral studies, I had the chance to spend several months in Rome and to appreciate a scientific exchange with researchers at the Consiglio Nazionale delle Ricerche. It was an unforgettable time and a wonderful experience. I would like to express my most sincere gratitude to Giuseppe Pontrelli from the IAC-CNR who guided me throughout this thesis. His continued and friendly support, patience, excellent supervision, and critical reading of my work have been crucial for the progress and the completion of my thesis. Furthermore, I wish to thank Sauro Succi and Simone Melchionna for the fruitful discussions and their constructive feedback.

I am more than grateful to my parents and my family for their love and support. I also would like to thank my friends for offering me many enjoyable and relaxing moments counterbalancing my research work.

Finally, I wish to express my deep gratitude to my boyfriend Lukas Pilat for believing in me and supporting me in many ways throughout my thesis. I would not have made it without his love, patience, and continued encouragement and support.

This research was accomplished within the context of the project 'BioCompatible Materials and Applications - BCMA' initiated by the AIT Austrian Institute of Technology GmbH. It was partly funded by AIT and the federal state of Lower Austria and co-financed by the EC (EFRE).

Contents

| | | |
|----------|---|-----------|
| 1 | Introduction | 1 |
| 1.1 | Motivation and overview of related work | 1 |
| 1.2 | Objective of the thesis | 4 |
| 1.3 | Outline of the thesis | 5 |
| 2 | Fluid dynamics and elasticity theory | 6 |
| 2.1 | Basic equations of fluid dynamics | 6 |
| 2.1.1 | Fundamental parameters | 6 |
| 2.1.2 | The Navier-Stokes equations | 7 |
| 2.1.3 | Analytical solutions of the Navier-Stokes equations for special cases | 8 |
| 2.1.3.1 | Poiseuille flow | 9 |
| 2.1.3.2 | Womersley flow | 11 |
| 2.2 | One-dimensional blood flow simulation with the Navier-Stokes equations | 13 |
| 2.3 | Elasticity theory | 16 |
| 2.3.1 | Mechanics of the wall | 17 |
| 2.3.2 | Linear pressure-radius relationship | 20 |
| 3 | The lattice Boltzmann method | 22 |
| 3.1 | The Boltzmann equation | 23 |
| 3.1.1 | Description of fluids on different scales | 23 |
| 3.1.2 | The Boltzmann equation | 24 |
| 3.2 | The lattice Boltzmann equation | 26 |
| 3.2.1 | The LBGK equation | 27 |
| 3.2.2 | Chapman-Enskog procedure: from LBGK equation to Navier-Stokes equations | 31 |
| 3.2.3 | Applications and advantages of the LBM | 32 |
| 3.3 | Boundary conditions | 34 |
| 3.3.1 | Periodic boundary conditions | 34 |
| 3.3.2 | No-slip boundary conditions | 35 |
| 3.3.3 | Continuous bounce-back boundary condition | 37 |

| | | |
|----------|---|-----------|
| 3.3.4 | Inflow and outflow boundary conditions | 38 |
| 3.3.4.1 | Pressure boundary conditions | 39 |
| 3.3.4.2 | Velocity boundary conditions | 42 |
| 4 | Fluid-wall interaction | 44 |
| 4.1 | Modeling elastic walls in lattice Boltzmann simulations | 45 |
| 4.1.1 | Modeling the elastic wall | 45 |
| 4.1.1.1 | Displacement of vessel wall based on node type changes | 45 |
| 4.1.1.2 | Initialization of new fluid nodes | 46 |
| 4.1.2 | Population rescaling methods | 48 |
| 4.1.2.1 | Local rescaling | 48 |
| 4.1.2.2 | Rescaling by columns | 49 |
| 4.1.3 | Continuous bounce-back boundary condition | 49 |
| 4.2 | Pressure thresholds | 51 |
| 4.3 | The moving wall mechanism: coupling between pressure threshold and parameter q | 52 |
| 5 | Simulations and results | 54 |
| 5.1 | Computational aspects | 54 |
| 5.1.1 | Computational domain | 55 |
| 5.1.2 | Structure of the program | 55 |
| 5.1.3 | Memory requirements | 56 |
| 5.1.3.1 | Fundamental and derived variables in memory | 56 |
| 5.1.3.2 | Examples for memory usage | 58 |
| 5.2 | Numerical experiments | 59 |
| 5.2.1 | Simulations with periodic boundary conditions | 59 |
| 5.2.1.1 | Simulation parameters | 60 |
| 5.2.1.2 | Comparison between analytical and numerical solution | 61 |
| 5.2.1.3 | Approach for testing the modeling of elasticity using local rescaling | 62 |
| 5.2.1.4 | Approach for testing the modeling of elasticity using rescaling by columns | 66 |
| 5.2.1.5 | Recovery time | 69 |
| 5.2.2 | Simulations with inlet/outlet pressure boundary conditions . . . | 73 |
| 5.2.2.1 | Simulation parameters | 73 |
| 5.2.2.2 | Results with halfway bounce-back on the link boundary condition | 74 |
| 5.2.2.3 | Results with continuous bounce-back boundary condition | 78 |

| | | |
|----------|--|------------|
| 5.2.3 | Sensitivity analysis with inlet/outlet pressure boundary conditions | 85 |
| 5.2.3.1 | Influence of the compliance parameter α | 86 |
| 5.2.3.2 | Influence of the amplitude A | 89 |
| 5.2.3.3 | Influence of the pulse period T_{pulse} | 89 |
| 5.2.4 | Coupling between Windkessel model and lattice Boltzmann method | 91 |
| 5.2.4.1 | The Windkessel model | 92 |
| 5.2.4.2 | Coupling LBM/WK | 93 |
| 5.2.4.3 | Preliminary results from first test simulations | 95 |
| 6 | Towards physiological experiments: blood flow simulation through stents | 99 |
| 6.1 | Arterial stents: an overview | 100 |
| 6.2 | Modeling blood flow through a stented artery | 103 |
| 6.3 | Preliminary numerical experiments | 104 |
| | Summary and conclusions | 108 |
| | List of Figures | 110 |
| | List of Tables | 116 |
| | Bibliography | 117 |
| | Curriculum Vitae | 138 |

Chapter 1

Introduction

1.1 Motivation and overview of related work

Cardiovascular diseases are the most common cause of death in the European Union [50]. There is considerable evidence that the development of such diseases are, to a great extent, linked to the characteristics of the blood flow [150]. Since experimental methods in the cardiovascular system are difficult and limited, mathematical models and numerical methods to simulate the hemodynamic processes have gained importance in the past years.

Research in that domain includes studies incorporating the whole arterial tree [90] as well as studies of only parts of it, e.g., a segment of an artery [99]. This thesis aimed at developing a simple method for the simulation of blood flow in a vessel segment and hence focuses on the investigation of local flow behavior.

Many applications of fluid dynamics consider rigid boundaries as for example in hydraulics (flows through pipes). In some other applications, for instance in hemodynamics, it is important to include the wall compliance. Since arteries are elastic and change in diameter depending on the blood pressure inside (which oscillates due to the periodic pumping of the heart), it is of particular importance to include this elasticity in models of physiological flows in blood vessels. This means that appropriate models for both the fluid and the structure bounding this fluid have to be developed. Furthermore, relations describing the interaction between the fluid and the elastic wall have to be found.

Modeling the interaction between fluid and structure is a great challenge. Examples for which the interaction is not negligible are flow around airfoils, fish swimming, and blood flow in the cardiovascular system [106]. Many existing works deal with fluid-structure interaction problems [23, 24, 31, 46, 89, 106, 151, 152, 192, 198]. They differ by the method by which the set of equations for the fluid part (e.g., Navier-Stokes equations) and those for the solid part (e.g., wall equations) are solved. Different coupling algorithms exist as for example the coupled approach, the weakly coupled approach, or the uncoupled approach where the two set of equations are computed separately. A short description of each of these approaches can be found in [106].

Some of the cited works dealing with fluid-structure interaction problems use independent grids for the fluid part and the solid part. This requires appropriate mappings between the variables describing those two parts. A commonly used approach is the Arbitrary Lagrangian Eulerian (ALE) approach [198] which provides a mapping between the Lagrangian system (in which the structure is commonly described) and the Eulerian system (in which the fluid is generally described). In the ALE approach, the physical boundary is moving while the fictitious boundary (e.g., inlet/outlet section of a blood vessel) is kept fixed and is not deformed [106]. In the ALE approach, the grid is moving. An approach based on a non-moving grid is the Cartesian Cut Cells approach [106]. In this approach, no remeshing is needed. The wall enclosing the fluid domain moves through the grid which is kept fixed. A drawback of this method is that the computational domain can be quite large and that idle cells (cells outside of the fluid domain) are constantly visited in the computations. However, in simulations of blood flow in vessels, this method is applicable because wall deformations are small compared to the vessel diameter.

The algorithm for solving a fluid-structure interaction problem could be as follows [192]: (a) solve the structure problem (determine the wall position), (b) update the domain configuration and boundary conditions for the fluid model, (c) solve the fluid equations, (d) calculate the pressure and forcing terms for the structure model.

In the cardiovascular framework, the immersed fibers method proposed by C.S. Peskin in 1977 [147] can be regarded as the first attempt to study fluid-structure interaction problems in this domain [192]. Since then, other methods have been developed. Conventional numerical schemes for fluid-structure interaction problems couple the finite element method for solving the governing equations of the structure with a finite difference, finite element or finite volume method for the fluid description. The solid and fluid subsystems can be solved simultaneously [167] or separately [146, 189]. A com-

petitive alternative approach to these conventional numerical methods is the lattice Boltzmann (LB) method [180, 181] which has widely been applied to fluid-structure interactions problems in different forms [23, 24, 31, 46, 51, 52, 80, 89].

The method proposed by H. Fang et al. [51, 52] provides boundary conditions for elastic and moving boundaries. In this approach, virtual distribution functions at the boundary are introduced. The velocity at boundary nodes required to compute these virtual distribution functions is obtained by quadratic interpolation or extrapolation. The method of H. Fang has been successfully applied to lattice Boltzmann simulations in two-dimensional elastic tubes by A.G. Hoekstra et al. [80]. It is accurate but not appropriate for large simulations running in parallel because of the quadratic extrapolations and the fact that nodes change from the solid domain to the fluid domain and vice versa [46]. Another modification of the LB scheme to model coupled fluid-structure problems has been proposed by M. Krafczyk et al. [89]. It is based on the work of A.J.C. Ladd [93] who presented a general technique for the simulation of fluid-particle interactions (momentum exchange algorithm). The method is a combination of the lattice Boltzmann equation for the fluid domain and Newtonian dynamics of the solid particles. It allows to determine the interaction between fluid and solid boundary by directly using the lattice Boltzmann variables. M. Krafczyk et al. [89] applied the method to study the fluid-structure system of moving leaflets of an artificial heart valve driven by physiological blood flow. Also other numerical simulations using the method of A.J.C. Ladd have been carried out [94, 102, 122]. A theoretical investigation of the momentum exchange algorithm has been performed by A. Caiazzo [24]. Also B. Chopard and S. Marconi [31] modeled the fluid-wall interaction based on local exchange of momentum between solid and fluid particles. Their method differs from the approach of A.J.C. Ladd [93], in which the solid particles immersed in the fluid are rigid, and allows to model solid, deformable particles suspended in a fluid by using the LB method for both the fluid and the solid phase. An approach coupling the lattice Boltzmann model (for the fluid) with a lattice spring model (for the compliant boundary enclosing the fluid) has been proposed by G.A. Buxton et al. [23]. A network of 'springs' which are connected to each other describe the interaction. A major advantage of a lattice springs model is its computational efficiency [23]. Efficient computing is also provided by the approach of G.M. Doctors et al. [46] who performed LB simulations of pulsatile fluid flow in three-dimensional elastic pipes. Their method is "based on estimating the distances from sites at the edge of the simulation box to the wall along the lattice directions from the displacement of the closest point on the wall and the curvature there, followed by application of a nonequilibrium extrapolation method" [46].

Recently, D. Leitner [99] proposed a simple method for modeling elastic vessel walls in lattice Boltzmann simulations of arterial blood flow. The method is similar to the Cartesian Cut Cells approach mentioned above. The wall displacement is based on the local pressure and involves pressure thresholds corresponding to the pressure needed to balance the restoring forces from the elastic wall and to maintain this wall in equilibrium. The method presented by D. Leitner does not treat a ‘real’ fluid-structure interaction because it does not include the feedback from the wall to the fluid. Nevertheless, it provides good results for simulations of blood flow in artery segments by keeping the numerical algorithm simple and robust. However, the method has some drawbacks. One limitation of the approach of D. Leitner is for example that the wall cannot be displaced by less than one lattice unit of the underlying grid of the lattice Boltzmann simulations. This stepwise wall displacement can cause discretization errors that make the computed flow field inaccurate.

1.2 Objective of the thesis

This thesis presents an improvement of the method of D. Leitner. The objective is to elaborate a simple and accurate method for incompressible flow through distensible tubes that can be used for applications in hemodynamics. As in the work of D. Leitner, the LB method has been used for the simulations. The thesis introduces a novel boundary condition allowing a continuous displacement of the wall. The modeling of the elastic wall is kept simple as in the method of D. Leitner in order to preserve the efficiency of the LB algorithm. By developing a method acting strictly locally as the LB method itself, the complexity of the numerical algorithm is not increased.

An advantage of the developed approach is that it can also be used for simulating the blood flow through stents, which are wire metal meshes inserted into a narrowed artery to prevent its occlusion [109, 153]. Due to the geometry and the different stiffness properties of the stent, the behavior of the blood flow changes in a stented artery and thus, turbulences can occur. It is assumed that those turbulences can cause a renewed narrowing of the artery, so-called *in-stent restenosis*, which is a pathological process prevalently occurring after stent implantation [107]. For a deeper understanding of the flow field around stents and in order to understand the hemodynamic processes in the stent region, a simple method to simulate the blood flow through stents is of particular interest.

1.3 Outline of the thesis

The thesis starts with a motivation and an overview of related work in Chapter 1. The objective of the thesis is presented in this first chapter followed by an overview of the following chapters.

Chapter 2 gives an overview of fluid dynamics and elasticity theory. It summarizes the main principles in fluid dynamics, presents the mechanics of the boundaries, and provides the corresponding equations and relations important for this work.

The numerical method used for the simulations that have been carried out for this work is the lattice Boltzmann method. This mesoscale approach uses a statistical description of the fluid particles and has developed to a valuable alternative to classical numerical methods for solving problems of computational fluid dynamics. The method is presented in detail in Chapter 3. Besides describing the general method and its governing equations, this chapter also gives an overview of the main boundary conditions supplementing the basic algorithm and needed for the computation of the solution of a given problem.

Chapter 4 describes how the elasticity of the considered tube or vessel is modeled in the LB framework. After presenting two different rescaling methods that have been developed to ensure mass conservation, it introduces a new boundary condition that allows the wall to move continuously. Furthermore, a detailed description of the overall algorithm representing the fluid-wall interaction is given.

Based on the theory and the methods presented in Chapters 2 to 4, numerical experiments have been carried out to show the feasibility of the developed approach for modeling the elastic wall. The results of these test simulations are given in Chapter 5. The chapter concludes with an outlook on future work concerning the coupling between the LB algorithm and a Windkessel model to account for physiologically more correct boundary conditions at the termination of a vessel.

Chapter 6 presents a possible application of the developed methods in hemodynamics: the simulation of blood flow through stents.

Finally, a short summary and conclusions are given.

Chapter 2

Fluid dynamics and elasticity theory

This chapter gives an overview of the basic principles in fluid dynamics and elasticity theory. A more detailed introduction to fluid dynamics can be found in [1] and with focus on biomechanics in [60, 61, 137, 168].

2.1 Basic equations of fluid dynamics

The focus of this thesis is on the simulation of incompressible fluids for applications in hemodynamics. The developed methods aim at modeling the blood flow inside large arteries whilst taking into account the elasticity of the vessel wall. The blood flow inside a vessel can be described with the Navier-Stokes equations which are presented in this section.

2.1.1 Fundamental parameters

The fundamental parameters for the description of a fluid are the *fluid velocity* \vec{u} and the *pressure* p . Thus, a physical flow can be characterized by a velocity field $\vec{u}(\vec{x}, t)$ and a pressure field $p(\vec{x}, t)$, where t denotes the time and \vec{x} the position in space.

Flows for which $\frac{\partial \vec{u}}{\partial t} = \frac{\partial p}{\partial t} = 0$ are called *steady*. An example for a steady flow is the Poiseuille flow which is the solution of the Navier-Stokes equations under certain assumptions, see Section 2.1.3.1.

2.1.2 The Navier-Stokes equations

Blood is almost incompressible, which means that it is a fluid of nearly constant density. Even though it is a suspension of plasma and cellular constituents [85], it can be assumed to be homogeneous and Newtonian in arteries whose diameter is large. Newtonian fluids are fluids in which the shear stress is linearly proportional to the velocity gradient perpendicular to the direction of the shear. The proportionality constant is called dynamic viscosity and will be denoted by μ in the following.

For the description of the blood flow, the Navier-Stokes equations for incompressible fluids can be used. They apply for homogeneous and Newtonian fluids. The Navier-Stokes equations consist of two nonlinear partial differential equations of second order and are based on the principles of conservation of mass and momentum.

Let \vec{f} be the vector of external forces (e.g., gravitational force) acting on the fluid and let Δ denote the Laplace operator. Then, the Navier-Stokes equations for incompressible fluids are

$$\frac{\partial \vec{u}}{\partial t} + (\vec{u} \cdot \nabla) \vec{u} + \nabla p - \nu \Delta \vec{u} = \vec{f} \quad (2.1)$$

$$\operatorname{div} \vec{u} = 0 \quad (2.2)$$

with initial condition

$$\vec{u}(\vec{x}, t_0) = \vec{u}_0(\vec{x}).$$

Here, ν is the kinematic viscosity and is assumed to be constant. In a bounded domain, the Navier-Stokes equations have to be supplemented with convenient boundary conditions.

Eq. (2.1) is called *momentum equation*. It is based on the principle of momentum conservation which is an extension of Newton's second law. $(\vec{u} \cdot \nabla) \vec{u}$ are inertial forces and $\nu \Delta \vec{u}$ viscous forces (inner friction).

Eq. (2.2) is called *continuity equation*. It is based on the principle of mass conservation.

2.1.3 Analytical solutions of the Navier-Stokes equations for special cases

Under certain assumptions, the Navier-Stokes equations can be solved analytically. This section presents two analytical solutions, one for a plane steady flow and one for a pulsatile flow. These solutions can be used to validate numerical methods in blood flow simulation.

In this section, a straight and sufficiently long tube with circular cross section is considered, see Fig. 2.1. The focus is on the fully developed region of the flow. This is the region in which the velocity profile has reached equilibrium, that is when the influence of the no-slip boundary condition (i.e., zero velocity at the wall) effects the entire cross section of the tube [213].

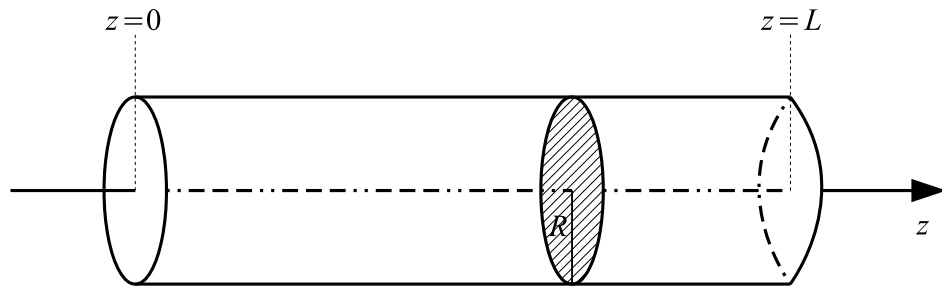


Figure 2.1: *Straight tube with circular cross section*

It can be shown [213] that, considering these simplifications and assuming that there are no external forces that would provoke flow rotation, the momentum equation reduces to

$$\rho \frac{\partial u}{\partial t} + \frac{\partial p}{\partial z} = \mu \left(\frac{\partial^2 u}{\partial r^2} + \frac{1}{r} \frac{\partial u}{\partial r} \right) \quad (2.3)$$

Here, cylindrical polar coordinates have been used. r denotes the radius of the tube and $u = u_z = u_z(r, t)$. The radial and angular component of the velocity are zero. Furthermore, the pressure $p = p(z, t)$ is a function of z and t only. This and the fact that the velocity does not change along the tube implies that the tube is rigid. Otherwise, if the pressure changed locally, the cross section of the tube and hence the velocity would change locally as well.

In Eq. 2.3, ρ denotes the density of the fluid. It is linked to the dynamic viscosity μ and the kinematic viscosity ν through

$$\nu = \frac{\mu}{\rho}. \quad (2.4)$$

2.1.3.1 Poiseuille flow

In the following, a steady-state solution for flow in a rigid tube will be derived.

If the velocity $u = u_z$ and the pressure p are independent of time, i.e.,

$$u_z = u_z(r), \quad p = p(z), \quad (2.5)$$

Eq. 2.3 becomes an ordinary differential equation and reduces to

$$\frac{dp}{dz} = \mu \left(\frac{d^2 u_z}{dr^2} + \frac{1}{r} \frac{du_z}{dr} \right). \quad (2.6)$$

Since the left-hand side of Eq. 2.6 is a function of z only and the right-hand a function of r only, the equation can be satisfied only if both sides are equal to a constant. Let k denote this constant. Thus

$$\frac{dp}{dz} = k \quad (2.7)$$

and

$$\mu \left(\frac{d^2 u_z}{dr^2} + \frac{1}{r} \frac{du_z}{dr} \right) = k. \quad (2.8)$$

The first equation (Eq. 2.7) has the solution

$$p(z) = p(0) + kz. \quad (2.9)$$

Let L be the length of the considered tube. Then,

$$p(L) = p(0) + kL. \quad (2.10)$$

and thus the constant k is given by

$$k = \frac{p(L) - p(0)}{L}. \quad (2.11)$$

The second equation (Eq. 2.8) has the solution

$$u_z(r) = \frac{k}{4\mu} r^2 + A \ln r + B \quad (2.12)$$

where A and B are integration constants. Taking into account the boundary conditions, A and B can be determined. At the center of the channel ($r = 0$), the velocity is finite, thus $|u_z(0)| < \infty$. This condition gives $A = 0$. At the wall ($r = R$), the no-slip

condition prevails, i.e., $u_z(R) = 0$, which gives $B = -\frac{kR^2}{4\mu}$. Finally, the solution of the ordinary differential equation 2.6 is given by

$$u_z = \frac{p(L) - p(0)}{4\mu L} (r^2 - R^2). \quad (2.13)$$

This solution gives a parabolic velocity profile, see Fig. 2.2. The corresponding flow is referred to as Poiseuille flow. It is often used to validate numerical methods.

Integrating u_z over a cross section gives the volumetric flow rate through the tube

$$Q = \int_0^R 2\pi r u_z(r) dr = -\frac{\pi R^4 (p(L) - p(0))}{8\mu L}. \quad (2.14)$$

The minus sign in equation 2.14 indicates that a negative pressure gradient induces flow in positive z direction. The equation is referred to as the Poiseuille equation [132]. The average velocity \bar{u}_z is obtained by dividing the volume flow Q by the cross-sectional area and is one half of the maximum velocity on the tube axis, thus

$$\bar{u}_z = \frac{Q}{\pi R^2} = \frac{-R^2 (p(L) - p(0))}{8\mu L}. \quad (2.15)$$

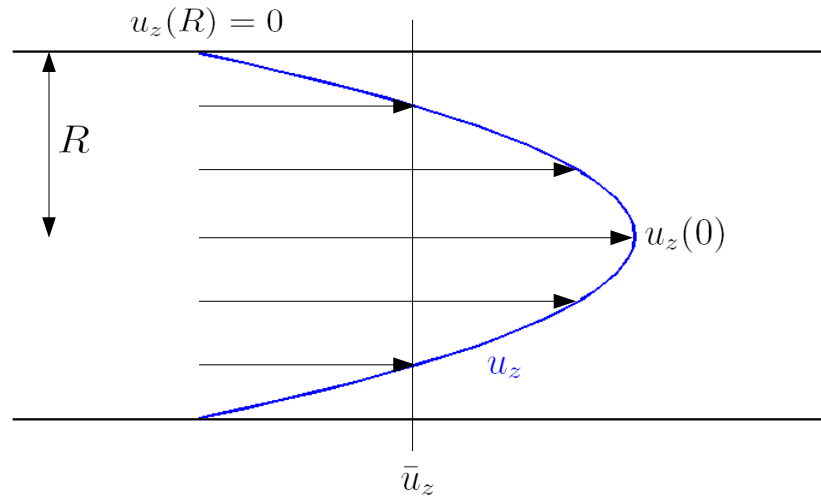


Figure 2.2: The parabolic velocity profile (u_z) of a fully developed steady Poiseuille flow. The average velocity \bar{u}_z is one half of the maximum velocity. At the wall, the velocity is zero (no-slip condition).

2.1.3.2 Womersley flow

Blood flow in arteries is not steady but pulsatile due to the periodic pumping of the heart. The following derivation accounts for a time-dependent pressure gradient. The starting point for deriving a solution is again the simplified momentum equation in cylindrical polar coordinates (Eq. 2.3) in which the velocity is a function of r and t while the pressure depends on z and t . Remember that this equation is valid only for the assumptions cited at the beginning of section 2.1.3 (straight, rigid, sufficiently long tube with circular cross section and axial symmetry, focus only on fully developed region of the flow).

For simplicity, the form of the time-dependent pressure gradient will be taken as a simple harmonic motion

$$\frac{\partial p(t)}{\partial z} = k e^{i\omega t} \quad (2.16)$$

where ω is the angular frequency of the motion and $i = \sqrt{-1}$. Taking the amplitude equal to the constant pressure gradient k (Eq. 2.7) allows for a comparison with the steady Poiseuille flow. A discussion about this comparison can be found in [213].

Note that, with the aid of Fourier series, any periodic function can be expressed as sum of harmonics as the one used in Eq. 2.16. Therefore, the solution for the made choice of the pressure gradient is of particular importance because it can be used to represent the arterial pulse which is a periodic function.

With this choice of the time-dependent pressure gradient, the governing equation for pulsatile flow becomes

$$\frac{\partial^2 u_z}{\partial r^2} + \frac{1}{r} \frac{\partial u_z}{\partial r} - \frac{\rho}{\mu} \frac{\partial u_z}{\partial t} = \frac{k}{\mu} e^{i\omega t} \quad (2.17)$$

A solution of Eq. 2.17 can be found by separation of variables. For this, u_z is decomposed into one part depending on r only and one depending on t only, i.e.,

$$u_z(r, t) = U(r) e^{i\omega t} \quad (2.18)$$

Substituting the decomposition of u_z in Eq. 2.17 gives, by cancellation of $e^{i\omega t}$ throughout the equation, an ordinary differential equation for $U(r)$

$$\frac{d^2 U}{dr^2} + \frac{1}{r} \frac{dU}{dr} - \frac{i\Omega^2}{R^2} U = \frac{k}{\mu} \quad (2.19)$$

which is a form of Bessel equation. Ω is a nondimensional parameter and is given by

$$\Omega = \sqrt{\frac{\rho\omega}{\mu}}R = \sqrt{\frac{\omega}{\nu}}R. \quad (2.20)$$

It is referred to as Womersley number, after J.R. Womersley who studied incompressible flows through a rigid tube with an oscillating pressure gradient, see for example [203], [204], and [205]. The Womersley number characterizes the kinematic properties of the fluid.

Another important nondimensional number characterizing the kinematic properties of a fluid flow is the Reynolds number. It is represented as the ratio between inertial forces and viscous forces. If V designates the characteristic flow speed and L the characteristic length, the Reynolds number Re is defined as

$$Re = \frac{VL}{\nu} \quad (2.21)$$

where ν is the kinematic viscosity. A flow with a low Reynolds number is termed *laminar*, whereas a flow with a high Reynolds number is called *turbulent*.

The solution of equation 2.19, appropriate to the boundary conditions of no-slip at the wall ($U(R) = 0$) and finite velocity along the tube axis ($|U(0)| < \infty$), reads [213]

$$U(r) = \frac{ikR^2}{\mu\Omega^2} \left(1 - \frac{J_0(\Omega i^{3/2} r/R)}{J_0(\Omega i^{3/2})} \right). \quad (2.22)$$

where J_0 is a Bessel function of order zero of the first kind [148].

Finally, using Eqs. 2.18 and 2.22, the solution of Eq. 2.17 for the pulsatile flow in a rigid tube is given by

$$u_z(r, t) = \frac{ikR^2}{\mu\Omega^2} \left(1 - \frac{J_0(\Omega i^{3/2} r/R)}{J_0(\Omega i^{3/2})} \right) e^{i\omega t}. \quad (2.23)$$

Fig. 2.3 shows the time-dependent Womersley profile in a rigid tube. A detailed discussion about Womersley flow can be found in [118] and [126].

The volumetric flow rate can be obtained by integrating the velocity profile $u_z(r, t)$

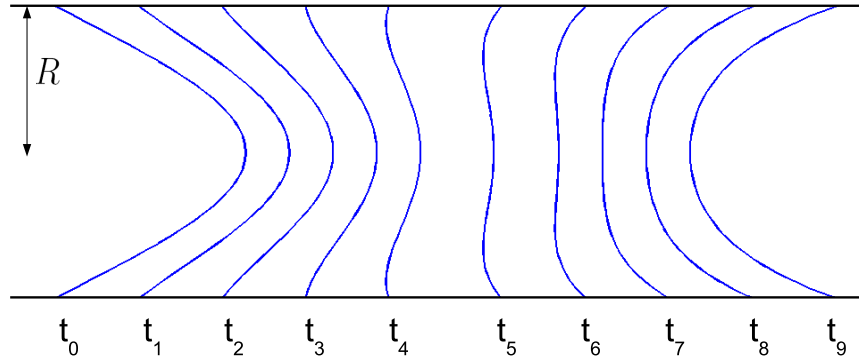


Figure 2.3: *Time-dependent Womersley flow with $\Omega \approx 0.056$ ($\omega = \frac{2\pi}{5000}$, $\nu = 0.4$, $R = 1$, in arbitrary units)*

over a cross section of the tube, which yields [213]

$$Q(t) = \int_0^R 2\pi r u_z(r, t) dr = \frac{i\pi k R^4}{\mu \Omega^2} \left(1 - \frac{2J_1(\Omega i^{3/2})}{\Omega i^{3/2} J_0(\Omega i^{3/2})} \right) e^{i\omega t}. \quad (2.24)$$

Here, J_1 is a Bessel function of first order and first kind.

In 1955, J.R. Womersely derived the analytical solution of the equation of motion of an elastic tube, assuming (similarly to the rigid case) an infinite long tube with circular cross section and an oscillating pressure gradient. The detailed derivation and the exact formulas of the solution can be found in [204].

2.2 One-dimensional blood flow simulation with the Navier-Stokes equations

As preparation for the next section, in which an introduction to the theory of the wall mechanics will be given, a one-dimensional model for the simulation of blood flow in large arteries is presented in this section. The model is based on the Navier-Stokes equations for a homogeneous incompressible fluid.

Considering a distensible axisymmetrical tube of length L and with a circular section of radius R (see Fig. 2.4), the one-dimensional cross averaged momentum equation

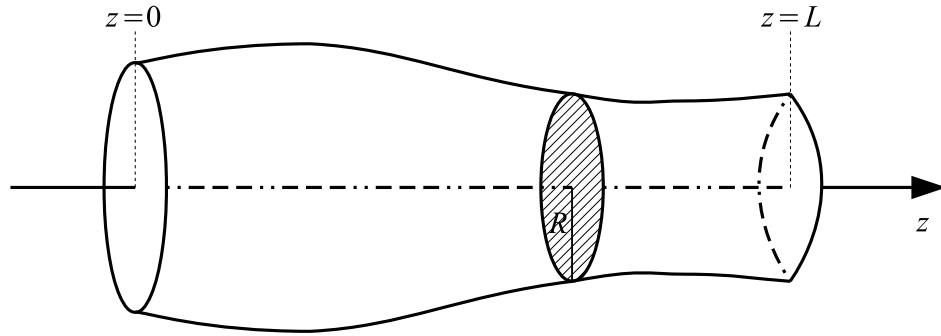


Figure 2.4: *Distensible axisymmetric tube of length L with circular cross section*

reads [151]

$$\frac{\partial \bar{u}}{\partial t} + \bar{u} \frac{\partial \bar{u}}{\partial z} + \frac{1}{\rho} \frac{\partial p}{\partial z} = 0 \quad (2.25)$$

where z denotes the axial coordinate, \bar{u} is the mean axial velocity, t is the time, and $p = p(z, t)$ is the pressure which is assumed to be constant on every cross section. The viscous term is supposed to be negligible and hence does not appear in the momentum equation.

With A denoting the cross sectional area, the continuity equation reads

$$\frac{\partial A}{\partial t} + \frac{\partial (A\bar{u})}{\partial z} = 0. \quad (2.26)$$

When linearizing the previous equations (Eqs. 2.26 and 2.25) supposing that

$$A = A_0 + \tilde{A} \quad (2.27)$$

$$p = p_0 + \tilde{p} \quad (2.28)$$

$$\bar{u} = u_0 + \tilde{u} \quad (2.29)$$

where \tilde{A} , \tilde{p} , and \tilde{u} are small perturbations ($|\tilde{A}| \ll 1$, $|\tilde{p}| \ll 1$, $|\tilde{u}| \ll 1$) and assuming furthermore that $u_0 = 0$, one obtains

$$\frac{\partial \tilde{A}}{\partial t} + A_0 \frac{\partial \tilde{u}}{\partial z} = 0 \quad (2.30)$$

$$\frac{\partial \tilde{u}}{\partial t} + \frac{1}{\rho} \frac{\partial \tilde{p}}{\partial z} = 0. \quad (2.31)$$

The cross sectional area A and the pressure p being related through a state equation

$A = A(p)$ which will be specified in the next section, one can write

$$\frac{\partial A}{\partial t} = \frac{dA}{dp} \frac{\partial p}{\partial t} = A' \frac{\partial p}{\partial t} \quad (2.32)$$

with $A' = \frac{dA}{dp}$. Substituting $\frac{\partial \tilde{A}}{\partial t}$ in Eq. 2.30 using Eq. 2.32, then differentiating Eq. 2.31 with respect to z and Eq. 2.30 with respect to t and dividing the latter by A_0 , and finally subtracting the obtained equations yields

$$\frac{\partial^2 \tilde{p}}{\partial t^2} - c_0^2 \frac{\partial^2 \tilde{p}}{\partial z^2} = 0. \quad (2.33)$$

Similarly, one can obtain

$$\frac{\partial^2 \tilde{u}}{\partial t^2} - c_0^2 \frac{\partial^2 \tilde{u}}{\partial z^2} = 0. \quad (2.34)$$

Eqs. 2.33 and 2.34 are classical wave equations of a traveling wave with wave speed

$$c_0 = \sqrt{\frac{A_0}{\rho A'(p_0)}} = \sqrt{\frac{A_0}{\rho} \frac{dp}{dA}(p_0)} = \sqrt{\frac{1}{\rho D_0}} \quad (2.35)$$

with $D_0 = \frac{A'(p_0)}{A_0}$. In the general case, still for small perturbations, one can define locally

$$c(z) = \sqrt{\frac{A_0}{\rho} \frac{dp}{dA}(z)} = \sqrt{\frac{1}{\rho D(z)}} \quad (2.36)$$

where

$$D(z) = \frac{1}{A} A'(p(z)) \quad (2.37)$$

is called *distensibility coefficient*.

Note that the wave propagation speed does not depend on the viscosity of the fluid but only on the deformability of the arteries, so the mechanical properties of the vessel wall. When the distensibility coefficient D decreases, which corresponds to a more rigid wall, the wave speed increases. In the limit case of a perfectly rigid channel ($D = 0$), the wave would propagate with infinite speed.

The deformability coefficient of arteries is of the order of 1 bar^{-1} ($1 \text{ bar} = 10^5 \text{ N m}^{-2}$) and corresponds, in normal physiological conditions, to an increase of the cross sectional area A of 10% for a pressure change of the order of 10^{-1} bar [103, 104]. The wave propagation speed in larger arteries is in the range of $3 - 10 \text{ m s}^{-1}$, whereas the fluid velocity is, with about 20 cm s^{-1} , much lower [85].

2.3 Elasticity theory

The main focus of elasticity theory are relations between forces acting on a body and its consequent deformation. The ratio of deformation to its initial configuration is called *strain*; the force per unit area of a surface producing the deformation is called *stress* [132]. Since stress is connected to a plane and a direction, it is a tensor [44]. The stress tensor σ is defined at any point in space and has nine components. In the three-dimensional Cartesian coordinate system, it is represented by the matrix

$$\sigma = \begin{bmatrix} \sigma_{xx} & \sigma_{xy} & \sigma_{xz} \\ \sigma_{yx} & \sigma_{yy} & \sigma_{yz} \\ \sigma_{zx} & \sigma_{zy} & \sigma_{zz} \end{bmatrix} \quad (2.38)$$

where the first subscript of σ_{ij} corresponds to the plane and the second subscript is the direction connected to this plane, e.g., σ_{xy} is the stress acting on the ‘ x -plane’ (parallel to the y - z -plane) in direction y . Fig. 2.5 shows the stresses σ_{ij} acting on an infinitesimal cubic element with faces parallel to the coordinate axes. Because angular momentum must be conserved on each differential volume element, $\sigma_{ij} = \sigma_{ji}$ [168]. Hence, the stress tensor is symmetrical and only six components are independent.

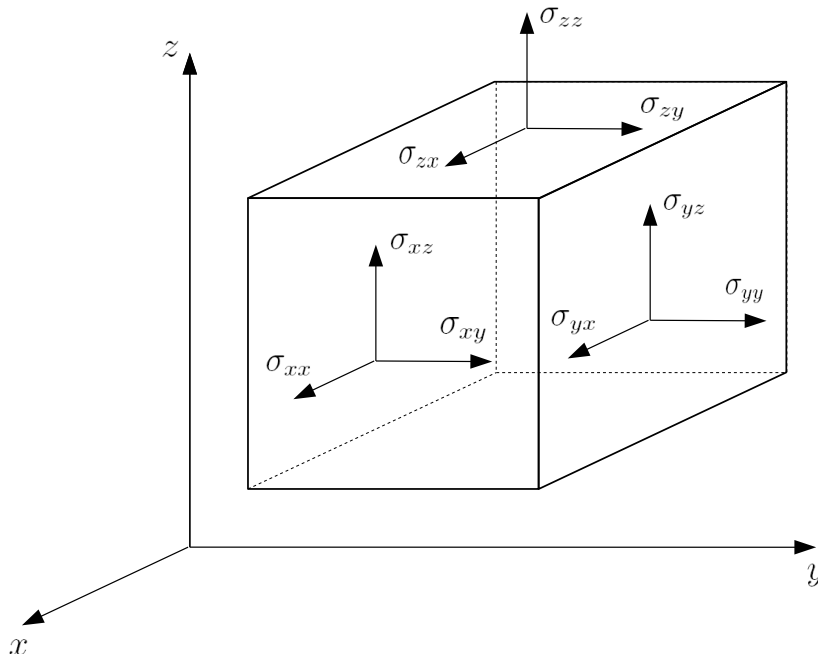


Figure 2.5: Components of the stress tensor on an infinitesimal cubic element in the Cartesian coordinate system

The off-diagonal components σ_{ij} , $i \neq j$, of the stress tensor are the shear stresses acting tangentially on the surface element parallel to the ' i -plane', whereas σ_{ii} are the normal stresses acting on this surface element in normal directions.

The shear stress is an important quantity, especially when studying the blood flow in arteries and the vascular response to it. As blood flows along the endothelial surface layer, a shear stress is generated which slows down the flow [91]. The shear stress at the wall is equal to the product of the fluid viscosity and the velocity gradient at the wall. Many authors mention the connection between the wall shear stress (WSS) and the pathogenesis of atherosclerosis [7, 21, 72, 128, 129, 130, 145, 170]. Several studies give significant evidence that low WSS and highly oscillating WSS cause intimal wall thickening [58, 59, 92, 144, 183, 214]. A review of the concepts and principles of WSS measurements can be found in [170].

The knowledge of the quantities \vec{u} and p allows the calculation of the forces that the arterial wall is exposed to due to the movement of the blood. The vessel wall is not stiff but elastic and expands if the pressure inside the vessel increases. This section gives an overview of elasticity theory with focus on the mechanics of the wall. In order to describe how the vessel reacts to a pressure change, a relationship between the pressure inside the vessel and its radius (or its cross sectional area) is needed.

2.3.1 Mechanics of the wall

The pressure wave generated by the beating of the heart induces a pressure change inside the vessel to which corresponds a change of the cross section. In this section, a relationship between the pressure p and the area A or, when considering a tube with circular cross section, the radius R will be derived. The obtained relation $A = A(p)$ (or $R = R(p)$) can be used to specify the ratio $\frac{dA}{dp}$ in the equations in the previous section (Eqs. 2.32, 2.35, and 2.37).

The wall of a blood vessel is not homogeneous but consists of different materials (elastin, collagen, and smooth muscle) which are responsible for the mechanical properties of the wall [85]. An overview of the mechanical properties of the single vessel wall components can be found in [44]. Due to the inhomogeneity, the relation between stress σ and strain e is nonlinear and complex. However, since the deformation of the wall is small in physiological conditions, this relation is commonly assumed to be linear if the following

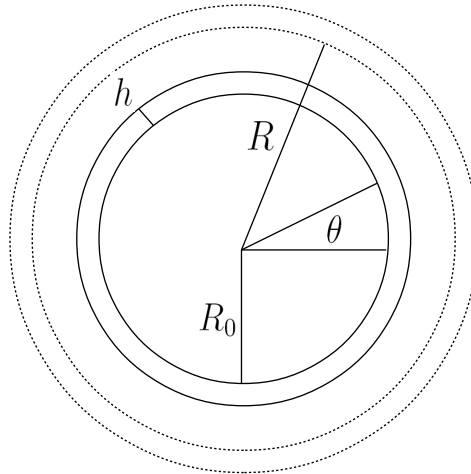


Figure 2.6: *Transversal section of a tube of thickness h*

assumptions and simplifications are made.

In the following, a distensible tube with circular cross section is assumed and cylindrical polar coordinates (r, θ, z) are used where r indicates the radial component, θ the angular component, and z the axial component. The radius of the tube in equilibrium corresponding to a reference pressure p_0 is denoted by R_0 . p_0 is the pressure for which the restoring forces from the elasticity of the wall are balanced. The wall of the tube is supposed to be homogeneous and to have a thickness h that is small compared to the reference radius R_0 of the channel, i.e., $h \ll R_0$, see Fig. 2.6. When the pressure p increases, $p > p_0$ with $p \approx p_0$, the tube deforms and its radius increases, i.e., $R > R_0$ with $R \approx R_0$ where R denotes the new radius. Assuming furthermore that the components of the stress along the directions r and z , σ_r and σ_z , are negligible, one can write for the component of the stress in azimuthal direction

$$\sigma_\theta = E e_\theta \quad (2.39)$$

where $e_\theta = \frac{R - R_0}{R_0}$ is the strain corresponding to the stress σ_θ and E is the Young's modulus. The linear relation $\sigma = E e$ is known as Hooke's law and is valid for purely elastic materials [44]. The Young's modulus E describes the stiffness of the material in direction of the deformation [137]. It has the dimension of force/surface. For arteries, the value of E ranges between $2 \cdot 10^5$ and $10 \cdot 10^5 \text{ N/m}^2$ [132].

From the balance of the forces acting on the tube wall, one obtains that the tension T in direction θ is proportional to the pressure difference $p - p_0$ causing the deformation and is given by the Laplace law which states a relationship between the surface tension,

the pressure, and the curvature of a surface [60].

$$T = (p - p_0) R \quad (2.40)$$

In absence of a pressure change, the tension T is zero. Assuming that σ_θ is constant and dividing Eq. 2.40 by the wall thickness h yields

$$\sigma_\theta = \frac{(p - p_0) R}{h}. \quad (2.41)$$

When multiplying Eq. 2.41 by h and differentiating it, one obtains

$$h d\sigma_\theta = R dp + (p - p_0) dR. \quad (2.42)$$

From Eqs. 2.39 and $e_\theta = \frac{R - R_0}{R_0}$ it follows that

$$d\sigma_\theta = E de_\theta = E \frac{dR}{R_0}. \quad (2.43)$$

Finally, combining Eqs. 2.42 and 2.43 yields

$$\frac{dR}{dp} = \frac{R R_0}{E h - (p - p_0) R_0}. \quad (2.44)$$

Assuming that $p - p_0 \ll \frac{E h}{R_0}$ and that deformations are small, i.e., $R \approx R_0$ (and correspondingly $p \approx p_0$), Eq. 2.44 can be simplified yielding the approximation

$$\frac{dR}{dp} = \frac{R^2}{E h}. \quad (2.45)$$

This is an ordinary differential equation and can be solved by separation of variables. With the initial condition $R(p_0) = R_0$, the solution is

$$R(p) = R_0 \left(1 - \frac{R_0(p - p_0)}{E h} \right)^{-1}. \quad (2.46)$$

Eq. 2.46 is a nonlinear relation between the radius R and the pressure p .

Eq. 2.45 is a relation of the form

$$dR = \frac{\beta}{2} dp \quad (2.47)$$

Here, β is the compliance of the tube. It is inversely proportional to the Young's

modulus E . To obtain the corresponding relation between dp and the change of the cross-sectional area $A = \pi R^2$, dR in Eq. 2.45 is replaced using $dA = 2\pi R dR$, which, after rearrangement of the terms, results in

$$\frac{dp}{dA} = \frac{E h}{2\pi R^3}. \quad (2.48)$$

This ratio can now be substituted in Eq. 2.36 which yields

$$c = \sqrt{\frac{1}{\rho D}} = \sqrt{\frac{A dp}{\rho dA}} = \sqrt{\frac{A E h}{\rho 2\pi R^3}} = \sqrt{\frac{E h}{2R \rho}}. \quad (2.49)$$

The relation

$$c = \sqrt{\frac{E h}{2R \rho}}. \quad (2.50)$$

is known as the *Moens-Korteweg* equation [132]. It can be used to determine experimentally the Young's modulus E . When knowing h and R and measuring c , E can be calculated by using Eq. 2.50. Note that the Moens-Korteweg equation is valid presuming small perturbations and a linear elastic material.

Combining Eqs. 2.37 and 2.48 gives a relation between the distensibility coefficient D and the Young's modulus E :

$$E = \frac{2R}{h D}. \quad (2.51)$$

2.3.2 Linear pressure-radius relationship

Under normal circumstances, the thickness h of the vessel wall is small compared to the reference radius R_0 [116]. As a consequence, the vessel wall can be treated as a thin elastic membrane.

The relation between pressure and radius in Eq. 2.46 is nonlinear. For the simulations in chapter 5, a linear pressure-radius relationship is assumed. A similar approximation has been assumed by Y.C. Fung in his book *Biodynamics: Circulation* [61].

Using the notation from above, the assumed relationship is

$$p - p_0 = \alpha(R - R_0) \quad (2.52)$$

where α is a compliance constant. In other words, $(p - p_0)$ is the excess pressure needed

to induce the wall displacement $(R - R_0)$.

The relation in Eq. 2.52 is similar to that of the pulmonary blood vessels [52, 61] and a good approximation for large arteries [80].

Chapter 3

The lattice Boltzmann method

The Navier-Stokes equations can be solved analytically only in special cases. In Section 2.1.3, two analytic solutions for steady and pulsatile incompressible flow in a rigid cylindrical tube have been presented (Poiseuille and Womersley flow). In more general cases, the Navier-Stokes equations can be solved by using numerical methods. Conventional approaches, as the finite element method, are top-down approaches which discretize the underlying partial differential equations in time and space. The finite element method is implemented in many solvers for problems of computational fluid dynamics and has widely been applied to blood flow simulations [2, 97, 146, 182, 187, 188].

This chapter presents an alternative method to classical numerical schemes. It is a bottom-up approach based on the molecular behavior of the fluid. The starting point is the Boltzmann equation of statistical mechanics which will be introduced in the next section. The resulting lattice Boltzmann (LB) method is a mesoscopic approach based on the Boltzmann equation and can be used to solve various problems of computational fluid dynamics. For a detailed overview of theory and applications of the lattice Boltzmann method (LBM), the reader is referred to [16].

A short discussion about top-down versus bottom-up approaches (see Fig. 3.1) can be found in the book of D.A. Wolf-Gladrow [202].

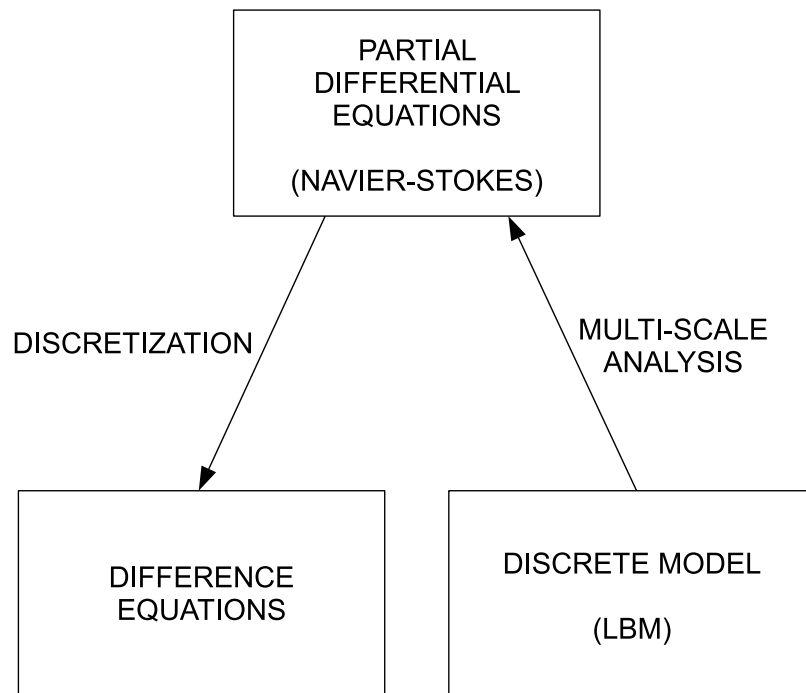


Figure 3.1: *Top-down versus bottom-up approach*

3.1 The Boltzmann equation

When applying numerical methods, it is important to consider the properties of the underlying equations. There are physical constraints, e.g., conservation of mass and momentum, that have to hold also for the derived equations of the numerical method. Furthermore, there are complex boundary conditions in fluid dynamics, e.g., a complex geometry or complex dynamic boundary values [99]. In blood flow simulations, these complex boundary conditions are for example the geometry of the vessels, the properties of the vessel wall and its interaction with the fluid, and the dynamic nature of pressure and flow.

3.1.1 Description of fluids on different scales

The description of fluids can be done on different scales [99]:

- **Microscopic scale:** On the smallest scale, the molecules of the fluid are described by structureless particles moving along trajectories. The underlying equations are the Newton equations. The simulations can be performed with lattice

gas cellular automata (LGCA).

- **Mesoscopic scale:** On the mesoscopic scale, a statistical description of the fluid particles is used (Liouville and Boltzmann equation). The lattice Boltzmann method provides a numerical scheme to solve the discretized Boltzmann equation.
- **Macroscopic scale:** On the largest scale, the macroscopic scale, the fluid is described by relations between macroscopic variables (e.g., fluid density, fluid velocity) and by using the theory of continuum mechanics. Nonlinear partial differential equations as the Navier-Stokes equations are discretized and solved with classical numerical methods (finite differences [127], finite elements [217], finite volumes [22], spectral methods [108]).

3.1.2 The Boltzmann equation

For the description of blood flow, the microscopic scale with the Newton equations is not appropriate because of the large number of molecules. It is more convenient to use a statistical description with the help of the Boltzmann equation. The main variables of the underlying equations are distribution functions $f(\vec{x}, \vec{v}, t)$ which give the ensemble averaged quantity of molecules at the position \vec{x} in space with the velocity \vec{v} at time t . The evolution over time of these distribution functions is given by the Boltzmann equation [202]

$$\left(\frac{\partial}{\partial t} + \vec{v} \cdot \nabla \right) f(\vec{x}, \vec{v}, t) = Q(f, f) \quad (3.1)$$

where Q denotes the collision integral describing the physical interaction of the particles. Thus, Eq. 3.1 is an integro-differential equation. External forces have been neglected.

The macroscopic variables (density ρ , momentum \vec{j} , and momentum flux tensor Π) can be calculated in the following way.

$$\rho(\vec{x}, t) = \int m f(\vec{x}, \vec{v}, t) d\vec{v} \quad (3.2)$$

$$\vec{j}(\vec{x}, t) = \rho(\vec{x}, t) \vec{u}(\vec{x}, t) = \int m \vec{v} f(\vec{x}, \vec{v}, t) d\vec{v} \quad (3.3)$$

$$\Pi_{\alpha\beta}(\vec{x}, t) = \int m v_{\alpha} v_{\beta} f(\vec{x}, \vec{v}, t) d\vec{v} \quad (3.4)$$

Here, m denotes the particle mass, \vec{v} the particle velocity and \vec{u} is the fluid velocity.

A distribution function that remains unchanged by the collision operator, i.e., $Q(f, f) = 0$, is defined as equilibrium distribution function f^{eq} . Such an equilibrium distribution function is given by the Maxwell-Boltzmann distribution [202]

$$f^{eq}(\vec{x}, \vec{v}, t) = \rho \left(\frac{m}{2\pi k_B T} \right)^{D/2} e^{-\frac{m(\vec{v}-\vec{u})^2}{2k_B T}} \quad (3.5)$$

where k_B is the Boltzmann constant, T the temperature, and D the spatial dimension. Note that the equilibrium distribution function depends on \vec{x} and t only implicitly through the macroscopic variables $\rho(\vec{x}, t)$ and $\vec{u}(\vec{x}, t)$. In 1872, L. Boltzmann showed with the famous Boltzmann theorem [19] that every initial distribution function satisfying the Boltzmann equation decays to the Maxwell-Boltzmann distribution.

Historically, the lattice Boltzmann method has developed from the lattice gas cellular automata (LGCA) [202] with the goal to overcome one of the major drawbacks of LGCA: statistical noise [180]. In 1988, G.R. McNamara and G. Zanetti [119] introduced the LB method for the first time [215] to eliminate statistical noise. The new method used particle distribution functions instead of individual particles of the LGCA. Later, it has been shown that the LB equation can also be derived from the continuous Boltzmann equation [73].

In analogy to the LGCA, a nonlinear collision operator has been used for first applications of the lattice Boltzmann equation, having the drawback that the simulations are computationally expensive [119]. F.J. Higuera and J. Jimenez [76] presented a linear collision operator by approximating the collision term by a linearization about a local equilibrium f^{eq} . This results in a quasilinear LB equation. The detailed construction of the collision operator can be found in [180]. P.L. Bhatnagar, E.P. Gross, and M. Krook [18] presented a coarser approximation for the collision operator Q . The resulting equation of the BGK model uses single-time relaxation towards a local equilibrium:

$$\left(\frac{\partial}{\partial t} + \vec{v} \cdot \nabla \right) f(\vec{x}, \vec{v}, t) = -\omega (f(\vec{x}, \vec{v}, t) - f^{eq}(\vec{x}, \vec{v}, t)) \quad (3.6)$$

Here, f^{eq} is the Maxwell-Boltzmann distribution (see Eq. 3.5). $\omega = \frac{1}{\tau}$ denotes the collision frequency and τ the collision time. The BGK approximation fulfills two important properties of the collision operator [99]. Firstly, mass and momentum are conserved. Secondly, the distribution function decays to a Maxwell-Boltzmann distribution.

3.2 The lattice Boltzmann equation

Discretization of the Boltzmann equation in time and space leads to the lattice Boltzmann equation [74]. For this, the phase space is reduced to a limited set of allowed velocities \vec{c}_i , $i = 0, \dots, q - 1$, where q is the number of allowed directions of the velocity vector \vec{c}_i . The resulting lattice Boltzmann equation describes the evolution of fictitious particles on nodes of a regular lattice. In the following, Δt and $\Delta \vec{x}$ denote the temporal resolution and the lattice spacing corresponding to the discretization of the Boltzmann equation, respectively. Temporal and spatial resolution are related through $\Delta \vec{x} = \vec{c}_i \Delta t$ to guarantee Lagrangian behavior [176]. Using the abbreviating notation $f_i(\vec{x}, t) \equiv f(\vec{x}, \vec{c}_i, t)$ for the distribution functions (also called *populations*), the lattice Boltzmann equation reads

$$f_i(\vec{x} + \vec{c}_i \Delta t, t + \Delta t) - f_i(\vec{x}, t) = -\Delta t Q_i \quad (3.7)$$

where Q_i is the collision operator. As for the Boltzmann equation, the distribution functions $f_i(\vec{x}, t) = f(\vec{x}, \vec{c}_i, t)$ model the dynamics of the flow field and describe the probability of finding at time t a particle located at site \vec{x} and traveling along the lattice in direction i with the speed \vec{c}_i . Starting from an initial state, the populations evolve at every time step in two consecutive sub-steps: (a) *collision*, describing the interaction of particles at a node, and (b) *streaming (propagation)*, in which each particle is propagated to the neighboring node based on the direction of its velocity, see Fig. 3.2.

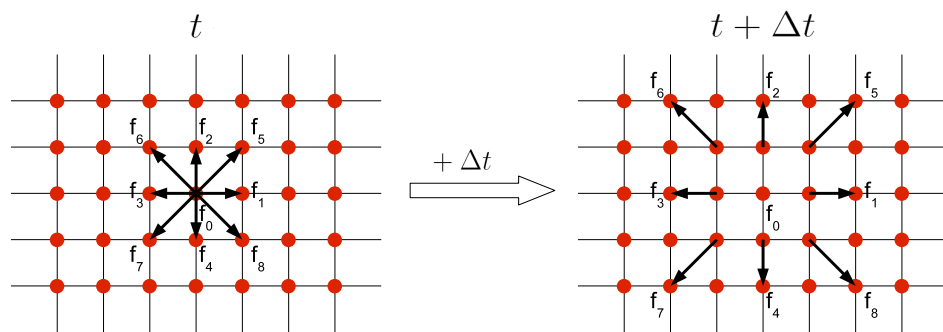


Figure 3.2: *Propagation step: each population is propagated to the neighboring node corresponding to the direction of its velocity.*

In analogy to Eqs. 3.2, 3.3, and 3.4, the macroscopic variables are the zeroth, first,

and second hydrodynamic moments of the distribution functions f_i :

$$\rho(\vec{x}, t) = \sum_i f_i(\vec{x}, t) \quad (3.8)$$

$$\vec{j}(\vec{x}, t) = \rho(\vec{x}, t) \vec{u}(\vec{x}, t) = \sum_i \vec{c}_i f_i(\vec{x}, t) \quad (3.9)$$

$$\Pi_{\alpha\beta}(\vec{x}, t) = \sum_i c_{i\alpha} c_{i\beta} (f_i(\vec{x}, t) - f_i^{eq}(\vec{x}, t)) \quad (3.10)$$

3.2.1 The LBGK equation

The lattice Boltzmann equation with BGK approximation (single-time relaxation) reads

$$f_i(\vec{x} + \vec{c}_i \Delta t, t + \Delta t) - f_i(\vec{x}, t) = -\omega \Delta t (f_i - f_i^{eq})(\vec{x}, t) \quad (3.11)$$

with Δt being the temporal resolution and ω being the relaxation frequency.

The equilibrium distribution functions f_i^{eq} are given by a second-order expansion of the Maxwell-Boltzmann distribution.

$$f_i^{eq}(\rho, \vec{j}) = \frac{w_i}{\rho_0} \left(\rho + \frac{m}{k_B T} \vec{c}_i \cdot \vec{j} + \frac{m}{2\rho k_B T} \left(\frac{m}{k_B T} (\vec{c}_i \cdot \vec{j})^2 - |\vec{j}|^2 \right) \right) \quad (3.12)$$

ρ_0 denotes the mass density, m the particle mass, k_B the Boltzmann constant, and T the temperature. The parameters w_i are weighting factors and depend on the chosen lattice. Note that f_i^{eq} depends only on ρ and \vec{j} . Using $\vec{j} = \rho \vec{u}$, Eq. 3.12 can be rewritten to

$$f_i^{eq}(\rho, \vec{u}) = \frac{w_i \rho}{\rho_0} \left(1 + \frac{m}{k_B T} \vec{c}_i \cdot \vec{u} + \frac{m}{2k_B T} \left(\frac{m}{k_B T} (\vec{c}_i \cdot \vec{u})^2 - |\vec{u}|^2 \right) \right) \quad (3.13)$$

The equilibrium distribution functions are derived by using the principle of maximum entropy under the constraints of conservation of mass, momentum, and momentum flux [86]. As a consequence, the f_i^{eq} 's fulfill the following relations:

$$\rho(\vec{x}, t) = \sum_i f_i^{eq}(\rho, \vec{j}) \quad (3.14)$$

$$\vec{j}(\vec{x}, t) = \sum_i \vec{c}_i f_i^{eq}(\rho, \vec{j}) \quad (3.15)$$

The weighting factors w_i have to be chosen in accordance with the velocities c_i such

| Direction i | Length of \vec{c}_i | Weighting factor w_i |
|---------------|-----------------------|------------------------|
| 0 | 0 | 4/9 |
| 1, 2, 3, 4 | c | 1/9 |
| 5, 6, 7, 8 | $\sqrt{2}c$ | 1/36 |

Table 3.1: *Weighting factors of the D2Q9 LBGK lattice*

that for $\vec{j} = \vec{0}$, the hydrodynamic moments up to the fourth order of the equilibrium distribution function equal the hydrodynamic moments of the Maxwell-Boltzmann distribution (Eq. 3.5) [99]. The resulting equations are generally under-constrained and hence admit several solutions [180]. Several solutions for w_i and $\frac{m}{k_B T}$ for different lattices can be found in [162] and [163].

The lattices of the LB method are commonly called $DdQq$ where d indicates the spatial dimension and q the number of lattice velocities \vec{c}_i . The lattice speed

$$c = \frac{\Delta x}{\Delta t} \quad (3.16)$$

relates the temporal resolution Δt and the spatial resolution Δx .

In two spatial dimensions, a widely used lattice is the $D2Q9$ lattice, see Fig. 3.3. The velocity \vec{c}_0 corresponds to a resting particle. $\vec{c}_1, \dots, \vec{c}_8$ are the velocities with directions pointing towards the eight neighboring nodes. For the $D2Q9$ LBGK lattice, $\frac{m}{k_B T} = \frac{3}{c^2}$. The corresponding weighting factors are listed in Table 3.1.

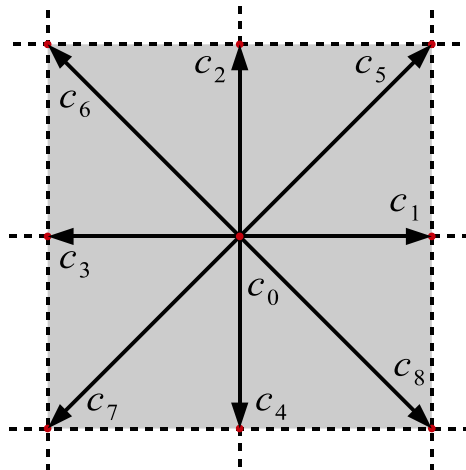


Figure 3.3: *D2Q9 lattice*

In three dimensions, the most popular choices are the $D3Q15$ and the $D3Q19$ lattices,

| Direction i | Length of \vec{c}_i | Weighting factor w_i |
|---------------|-----------------------|------------------------|
| 0 | 0 | 2/9 |
| 1 – 6 | c | 1/9 |
| 7 – 14 | $\sqrt{3}c$ | 1/72 |

Table 3.2: Weighting factors of the $D3Q15$ LBGK lattice

| Direction i | Length of \vec{c}_i | Weighting factor w_i |
|---------------|-----------------------|------------------------|
| 0 | 0 | 3/9 |
| 1 – 6 | c | 1/18 |
| 7 – 18 | $\sqrt{2}c$ | 1/36 |

Table 3.3: Weighting factors of the $D3Q19$ LBGK lattice

see Figures 3.4 and 3.5, respectively, with the corresponding weighting factors listed in Tables 3.2 and 3.3, respectively. For both these lattices, $\frac{m}{k_B T} = \frac{3}{c^2}$. Compared to the $D3Q19$ model, the $D3Q15$ model is computationally less expensive and needs less memory. An advantage of the $D3Q19$ model instead is that its stability range is larger [99].

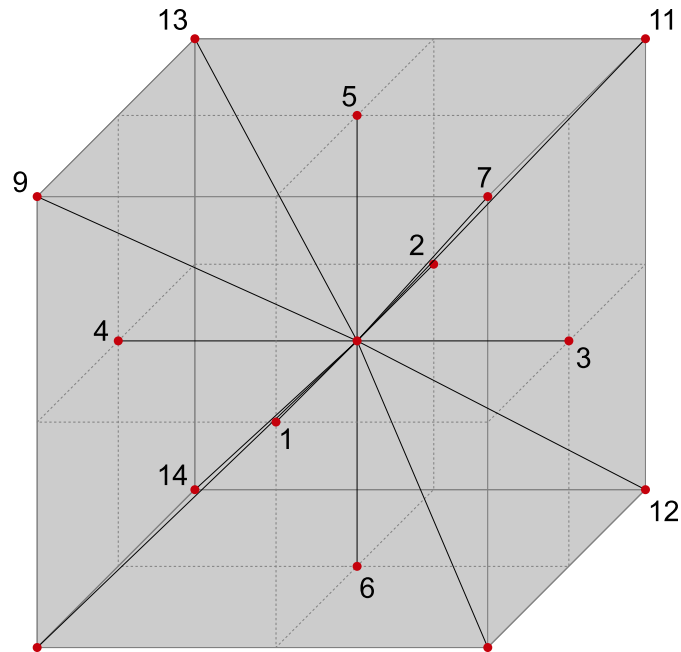


Figure 3.4: $D3Q15$ lattice

For the presented $DdQq$ lattices of the LBGK method, the pressure p is linearly related

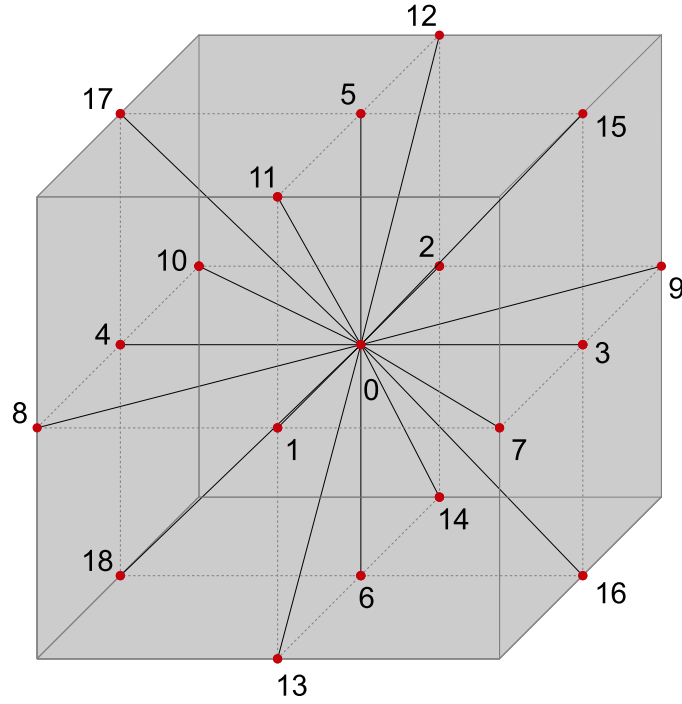


Figure 3.5: *D3Q19 lattice*

to the density ρ through a state equation:

$$p(\vec{x}, t) = \frac{k_B T}{m} \rho(\vec{x}, t) = \frac{c^2}{3} \rho(\vec{x}, t) \quad (3.17)$$

Thus, the pressure field can easily be obtained from the density field. Density and velocity field are determined by using Eqs. 3.8 and 3.9.

The viscosity ν is given by

$$\nu = \frac{c^2}{3} \left(\frac{1}{\omega} - \frac{1}{2} \right) \Delta t = \frac{c^2}{3} \left(\tau - \frac{1}{2} \right) \Delta t \quad (3.18)$$

and the speed of sound c_s by

$$c_s = \sqrt{\frac{dp}{d\rho}} = \frac{c}{\sqrt{3}}. \quad (3.19)$$

3.2.2 Chapman-Enskog procedure: from LBGK equation to Navier-Stokes equations

With the help of the Chapman-Enskog procedure [26], it can be shown that the LBGK method presented in the previous section approximates the Navier-Stokes equations for incompressible fluids in the limit of low Mach numbers.

The Chapman-Enskog procedure is an asymptotic expansion relating the statistical mechanics with the theory of continuum fluid dynamics. It solves the Boltzmann equation by successive approximations [136]. The expansion parameter ϵ is the *Knudsen number* K_n which is defined as the ratio between the mean free path length (mean distance between two consecutive collisions) and the characteristic length scale of the system [202]. In the following, a short overview of the derivation of the Navier-Stokes equations from the LBGK equation is given.

The first step of the Chapman-Enskog procedure is to consider a multi-scale expansion of the time and space derivatives, ∂_t and ∂_{x_α} for $\alpha = 1, 2, 3$, in the parameter ϵ [176]:

$$\partial_t = \epsilon \partial_t^{(1)} + \epsilon^2 \partial_t^{(2)} + \dots \quad (3.20)$$

$$\partial_{x_\alpha} = \epsilon \partial_{x_\alpha}^{(1)} + \dots \quad (3.21)$$

As a next step, the distribution functions f_i are expanded around the equilibrium distribution functions f_i^{eq} as follows

$$f_i = f_i^{eq} + \epsilon f_i^{(1)} + \epsilon^2 f_i^{(2)} + O(\epsilon^3) \quad (3.22)$$

where $f_i^{(1)}$ and $f_i^{(2)}$ do not contribute to mass and momentum, i.e.,

$$\sum_i f_i^{(1)} = 0, \quad \sum_i \vec{c}_i f_i^{(1)} = 0 \quad (3.23)$$

$$\sum_i f_i^{(2)} = 0, \quad \sum_i \vec{c}_i f_i^{(2)} = 0. \quad (3.24)$$

Next, the term $f_i(\vec{x} + \vec{c}_i \Delta t, t + \Delta t)$ in the LBGK equation (Eq. 3.11) is expanded into a Taylor series up to second order and the multi-scale expansions of the time and space derivatives (see Eqs. 3.20 and 3.21) are inserted into this Taylor expansion. Then, inserting the Taylor expansion of $f_i(\vec{x} + \vec{c}_i \Delta t, t + \Delta t)$ and the expansion of f_i (see Eq.

3.22) into the LBGK equation, the kinetic equation takes the form

$$\epsilon E_i^{(0)} + \epsilon^2 E_i^{(1)} + O(\epsilon^3) = 0. \quad (3.25)$$

For the exact form of $E_i^{(0)}$ and $E_i^{(1)}$, the reader is referred to [99].

Finally, the Navier-Stokes equations can be obtained by taking the zeroth and first moments of $E_i^{(0)}$ and $E_i^{(1)}$. A more detailed derivation of the Navier-Stokes equations from the LBGK equation can be found in [202] and [176].

3.2.3 Applications and advantages of the LBM

The lattice Boltzmann approach has developed to a valuable method for solving problems of fluid dynamics. It has been applied to a broad range of problems, e.g.:

- particle suspensions in a fluid (C.K. Aidun et al. [3], D.S. Clague and P.J. Cornelius [32], E.J. Ding and C.K. Aidun [42, 43], Z.G. Feng and E.E. Michaelides [53], J. Horbach and D. Frenkel [81], N.Q. Nguyen and A.J.C. Ladd [131])
- single-component hydrodynamics (F.J. Higuera et al. [76, 77], G.R. McNamara and G. Zanetti [119])
- multi-phase and multi-component flows (A.D. Angelopoulos et al. [5], Q. Kang et al. [84], X. Nie et al. [133], D. Qi [158, 159], D. Qi and L. Luo [160, 161], M.A.A. Spaid and F.R. Phelan [174], J. Tölke et al. [191])
- reaction-diffusion systems (S.P. Dawson et al. [36], Y.H. Qian and S.A. Orszag [164])
- magnetohydrodynamics (S. Chen et al. [28])
- flows through porous media (Z.L. Guo and T.S. Zhao [69], C. Manwart et al. [111], B. Manz et al. [112], N.S. Martys and H. Chen [114], C. Pan et al. [143], R. Verberg and A.J.C. Ladd [194], J. Wang et al. [199])
- combustion (O. Filippova and D. Hänel [55], K. Yamamoto et al. [209])
- crystallization (W. Miller et al. [124, 125])

- hemodynamics (A.M. Artoli [7], A.M. Artoli et al. [8, 9, 10, 11, 12], J. Boyd et al. [21], C. Chen et al. [27], G. Doctors [45], H. Fang et al. [52], M. Hirabayashi et al. [78, 79], A.G. Hoekstra et al. [80], M. Krafczyk et al. [89], D. Leitner et al. [100, 101], D. Leitner [99], S. Melchionna et al. [123], G. Pontrelli [157], M. Tamagawa and S. Matsuo [185], X. Xu and J.S. Lee [208])

The lattice Boltzmann method has been successfully applied to hemodynamics by many authors (see list above), which has proven its value as an alternative approach to numerical methods based on the discretization of the Navier-Stokes equations of continuum mechanics for the simulation of blood flow. The growing application of the LBM in many fields in the last years is related to the advantages that this approach has, also in comparison to conventional computational fluid dynamics methods:

- The LBM is an explicit numerical method, which allows a simple, straight-forward implementation.
- The LBM is numerical stable for many applications. Several authors have investigated the numerical stability of this method (A.M. Artoli [7], G. Doctors [45], M. Junk et al. [83], P. Lallemand and L.S. Luo [95], J.D. Sterling and S. Chen [176], R. Verberg and A.J.C. Ladd [196], D. Yu et al. [211]).
- The LBM acts strictly locally and hence is suitable for parallelization. Studies on parallelization and code optimization have been performed by some authors of the LB community (C. Körner et al. [87], M.D. Mazzeo and P.V. Coveney [117], C. Pan et al. [143], T. Pohl et al. [149], J. Wang et al. [199], J. Wilke et al. [201], X. Wu et al. [207]).
- Compared to Navier-Stokes solvers, in which the nonlinear convective term ($\vec{u} \cdot \nabla \vec{u}$) has to be treated, the LBM does not include this term because convection is replaced by simple advection (propagation to the neighboring nodes) [211].
- In the LBM, the shear stress is calculated directly from the density distribution functions [13], see Eq. 3.10. This allows to easily determine the wall shear stress which is a crucial quantity related to the development of atherosclerosis [170].
- In LB simulations, the pressure is obtained through a state equation (see Eq. 3.17) instead of solving the Poisson equation as it is needed for solvers for the incompressible Navier-Stokes equations [211].

3.3 Boundary conditions

The lattice Boltzmann method offers a simple scheme for solving various problems of computational fluid dynamics. A difficulty, however, is to formulate boundary conditions (BC) because these are usually given for macroscopic variables (pressure or velocity) in hydrodynamic problems instead of the main LB variables which are the distribution functions f_i . At the boundary, the incoming distribution functions (pointing into the fluid domain) are not known after the propagation step and need to be determined [35]. Therefore, appropriate relations between the incoming and outgoing (known) distribution functions have to be defined in a way that the desired macroscopic behavior on the boundary of the domain is reproduced.

S. Succi [180] distinguishes between *elementary* and *complex* boundary conditions. Elementary boundary conditions are conditions where the boundary is aligned with the coordinates of the grid, whereas complex boundaries can cut mesh cells. In this work, only elementary boundary conditions (staircase boundaries) are applied. In the following sections, the boundary conditions used in this work will be presented. These include periodic BC, no-slip BC, and inflow/outflow BC. Several other BC exist (free-slip, frictional slip, sliding walls) whose treatment can be found elsewhere [180].

For the treatment of complex boundary conditions, one of the two following approaches can be applied:

- Extrapolation of the distribution functions near the curved wall (see Z. Guo et al. [67], R. Mei et al. [120, 121], or R. Verberg and A.J.C. Ladd [195, 196])
- Local grid refinement near the curved wall (see O. Filippova and D. Hänel [54, 56], D. Yu et al. [212], or W. Guo et al. [66]). A drawback of this approach is that the complexity of the implementation is increased because the different lattices have different time scales due to the coupling of the temporal and spatial resolution of the LBGK method [99].

3.3.1 Periodic boundary conditions

Periodic boundaries are often used to study fully developed flow in a theoretically infinite long tube. Their implementation is simple: the outward distribution functions

f_i^{out} (populations f_i pointing out of the fluid domain) are copied and assigned to the inward populations f_i^{in} of the opposite side of the domain, see Fig. 3.6. In the LB formalism, this means

$$f_i^{\text{in}}(\vec{x}_0, t + \Delta t) = f_i^{\text{out}}(\vec{x}_{N-1}, t) \quad (3.26)$$

$$f_i^{\text{in}}(\vec{x}_{N-1}, t + \Delta t) = f_i^{\text{out}}(\vec{x}_0, t) \quad (3.27)$$

where \vec{x}_0 and \vec{x}_{N-1} correspond to the coordinates of the first and last layer of fluid nodes in a given direction, respectively.

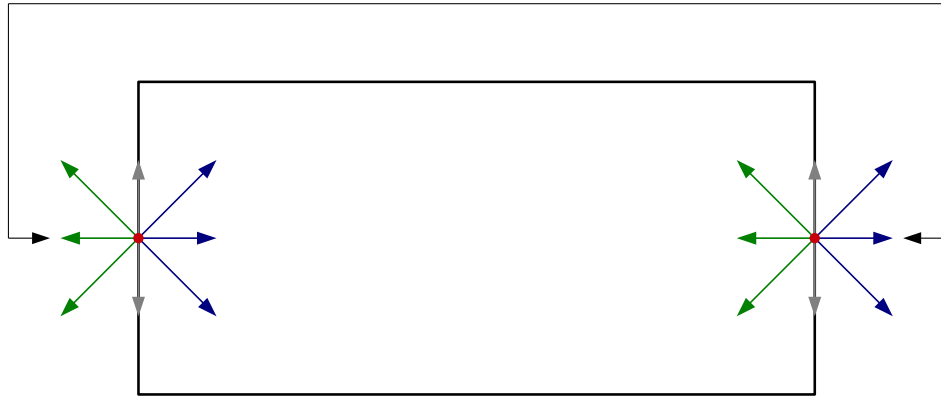


Figure 3.6: *Periodic boundary conditions*

For the implementation strategy, there are several options. One option is to use buffer nodes saving the populations of the last fluid nodes in a given direction. Once the buffers are filled, the particles can be moved at the propagation step to the appropriate location. A detailed description about the buffer strategy for a two-dimensional lattice can be found in [180]. Another option is to copy the populations directly in the physical domain without using buffer nodes. This strategy saves memory but requires much attention to the order in which the LB operations are processed in order to not overwrite values that are still needed for other computations.

In this work, periodic boundary conditions have been used for first simulations in order to prove that the implemented model provides correct physical behavior, see Section 5.2.1.

3.3.2 No-slip boundary conditions

A no-slip situation occurs at the solid boundary of a domain when the fluid velocity is zero at that boundary. There are two common ways of implementing the no-slip

condition

- bounce-back on the nodes (BBN), see for example [134] or [173]
- bounce-back on the link (BBL), see for example [93]

The bounce-back approach is a simple scheme to determine the unknown populations at a boundary node. The unknown populations f_i at the wall (those pointing inward) are determined by simply reflecting the known outward populations pointing into the opposite direction \bar{i} ($\vec{c}_i = -\vec{c}_{\bar{i}}$). For the BBN condition, the physical boundary lies on a lattice node, whereas for the BBL, the physical boundary is located between two lattice nodes (but aligned with the grid lines), see Fig. 3.7.

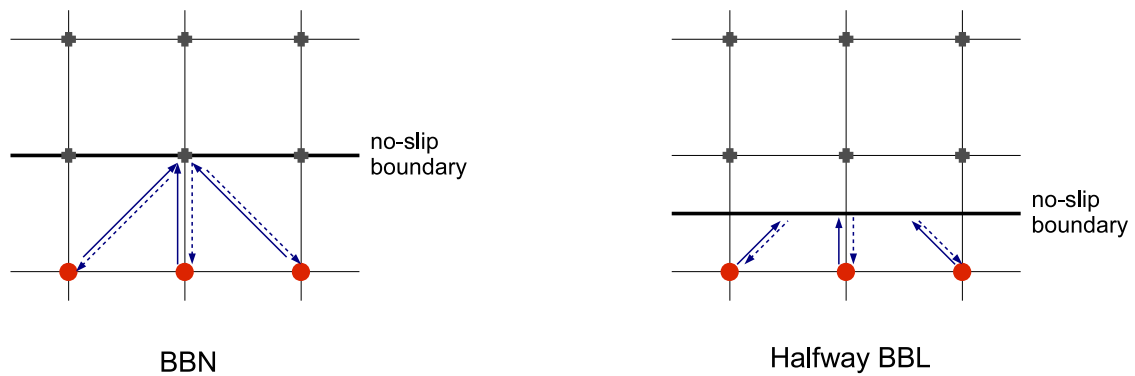


Figure 3.7: *No-slip boundary condition: bounce-back on the node (left) and halfway bounce-back on the link (right). The red filled circles represent fluid nodes; the gray crosses describe solid nodes. Full arrows indicate outgoing populations; dashed arrows denote reflected incoming populations*

R. Cornubert et al. [34] noticed that the numerical accuracy of the BBN condition is only first order at the boundary. This downgrades the LB algorithm because the LB equation is second-order in numerical accuracy for the interior lattice nodes [29]. Several methods for the treatment of boundary conditions have been proposed to improve the numerical accuracy of the LB method, see for example the methods proposed by P.A. Skordos [173], D.R. Noble et al. [134, 135], T. Inamuro [82], S. Chen et al. [30], and R.S. Maier et al. [110]. M.A. Gallivan [62] evaluated the bounce-back condition for LB simulations and showed that it provides a computationally efficient scheme for curved surfaces. For a comparison between some of the mentioned methods for the boundary treatment, the reader is referred to [98].

In the first simulations carried out in this thesis, the BBL condition has been used. In the LB formalism, this condition can be expressed as

$$f_i^{\text{in}}(\vec{x}, t + \Delta t) = f_{\bar{i}}^{\text{out}}(\vec{x}, t) \quad (3.28)$$

where f_i^{in} and $f_{\bar{i}}^{\text{out}}$ denote the unknown inward populations and corresponding known outward populations in opposite direction, respectively. \bar{i} indicates the direction opposite to i .

D.P. Ziegler [216] noticed that the BBL condition is second-order in numerical accuracy if the physical boundary is located halfway between two lattice nodes. This condition will be termed as ‘halfway bounce-back on the link’ or ‘halfway BBL’ condition in Chapter 5.

3.3.3 Continuous bounce-back boundary condition

The continuous bounce-back boundary condition is based on the simple bounce-back scheme and spatial interpolations. This method has first been introduced by M. Bouzidi et al. [20] and extended by P. Lallemand and L.S. Luo [96]. With the presented boundary condition, the wall can be placed arbitrarily between fluid and solid nodes, i.e., at an arbitrary distance from the last fluid node in a given direction. The unknown distribution functions are then calculated by using interpolations and the bounce-back rule.

The interpolation can be linear or quadratic. In this work, only the linear interpolation formulas will be described and used in the simulations to determine the unknown distribution functions near the wall with directions pointing into the fluid domain. For the quadratic interpolation formulas, the reader is referred to [20] and [96].

The wall is imagined to be located at a certain distance q from the last fluid node, see Fig. 3.8. It will be termed ‘virtual wall’ in the following because it only represents the interface between solid and fluid domain. The lattice spacing Δx is set to one; thus, q ranges between zero and one. If $q = 1/2$, the normal bounce-back rule is recovered (halfway bounce-back on the link). The following scheme is applied to all links that cross the imaginary wall. Let \vec{x}_j be a fluid node such that $\vec{x}_s = \vec{x}_j + \vec{c}_i \Delta t$ is a solid node and let \bar{i} denote the opposite direction of i (thus, $\vec{c}_{\bar{i}} = -\vec{c}_i$). For the unknown

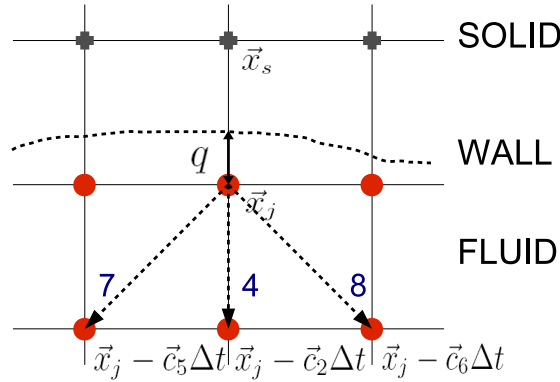


Figure 3.8: Continuous bounce-back boundary condition for a virtual wall located at distance q from the last fluid node \vec{x}_j . Gray crosses indicate solid nodes, red filled circles denote fluid nodes. The lattice spacing Δx is set to one. Dashed blue arrows represent directions i of unknown populations f_i which are determined using the linear interpolation in Eqs. 3.29 or 3.30.

distribution functions at node \vec{x}_j , the following linear interpolation is used.

$$f_i(\vec{x}_j, t+1) = 2q f_i^*(\vec{x}_j, t) + (1-2q) f_i^*(\vec{x}_j - \vec{c}_i \Delta t, t), \quad q < \frac{1}{2} \quad (3.29)$$

$$f_i(\vec{x}_j, t+1) = \frac{1}{2q} f_i^*(\vec{x}_j, t) + \frac{(2q-1)}{2q} f_i^*(\vec{x}_j, t), \quad q \geq \frac{1}{2} \quad (3.30)$$

Here, the superscript $*$ denotes the post-collisional state and Δt has been set to one.

For an application of this boundary condition, the reader is referred to the next chapter.

3.3.4 Inflow and outflow boundary conditions

For the simulation of arterial blood flow, it is often more convenient to use inflow/outflow (inlet/outlet) boundary conditions. By this, a velocity profile or a given pressure can be prescribed at the boundary.

A simple way to prescribe an inlet flow is to set the incoming (unknown) populations to their equilibrium value corresponding to the density ρ_{in} and velocity \vec{u}_{in} that one desires to prescribe:

$$f_i^{\text{in}} = f_i^{\text{eq}}(\rho_{\text{in}}, \vec{u}_{\text{in}}). \quad (3.31)$$

In blood flow simulation, a possible velocity profile for the inlet is for example a Poiseuille flow or a Womersley flow, see Section 2.1.3.

The outlet boundary condition is more complicated because one can have only a guess of the values to be prescribed at the outlet. Furthermore, the outflow boundary condition affects the flow field because of possible perturbations reflecting backwards into the fluid domain. If the tube is long enough, this effect can be neglected. In this case, a zero-gradient condition can be imposed; that is, the values of last layer of fluid nodes are the same as the values in the last but one layer of fluid nodes.

Setting the inward (unknown) populations to the equilibrium values as in Eq. 3.31 requires the prescription of both density and velocity. However, it is possible that in some applications only one of these values can be provided. In this case, the method of Q. Zou and X. He [220] is useful to prescribe either pressure (density) or velocity boundary conditions. It is based on the idea of bounce-back of the non-equilibrium part of the distribution functions. Using this idea, it is possible to calculate the missing (unknown) populations from the prescribed pressure (or velocity) and the populations known from the streaming step. The two following subsections give a detailed overview of the Zou/He method and of how the unknown populations are computed. Another method for pressure and velocity boundary conditions is described in [68] where the authors use a non-equilibrium extrapolation scheme for the boundaries.

3.3.4.1 Pressure boundary conditions

Due to the linear state equation between pressure and density (see Eq. 3.17) it is equivalent to prescribe pressure or density. Since the main physical variables in the LB method are density and velocity (as the hydrodynamic moments of the distribution functions), it will be written in the remainder of this work that ‘a certain density’ rather than ‘a certain pressure is prescribed’, keeping in mind that the two formulations are equivalent.

With the pressure boundary condition, it is possible to impose a pressure gradient between inlet and outlet. Note that this can cause a problem because the pressure gradient is the result of small density fluctuations, whereas the density fluctuations should actually be negligible in an incompressible fluid. Thus, it is important to keep the density fluctuations (and hence the pressure gradient) small.

The following calculations are based on the work of Q. Zou and X. He [220]. A $D2Q9$ lattice is considered and the computations shall be exemplarily performed for a node at the inlet of a two-dimensional channel. After propagation, the distribution functions

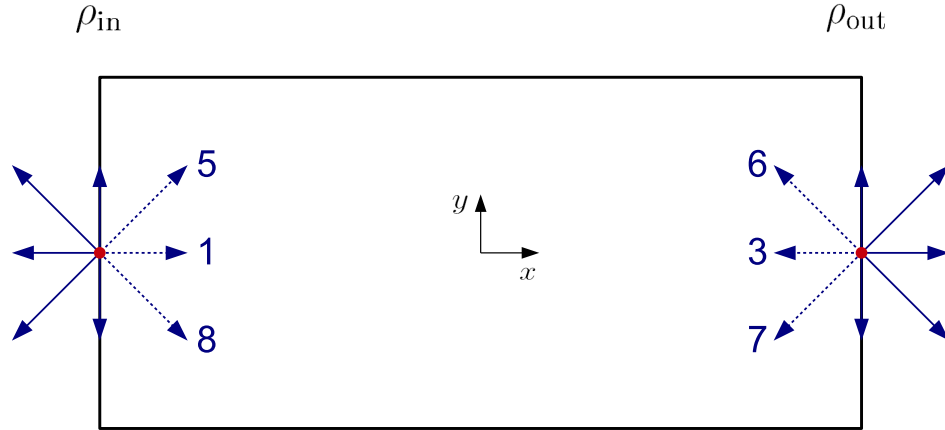


Figure 3.9: Inlet/outlet boundary conditions. Dashed arrows indicate unknown populations; full arrows denote known particles.

$f_0, f_2, f_3, f_4, f_6,$ and f_7 are known, whereas the populations $f_1, f_5,$ and f_8 have to be determined, see Fig. 3.9. Furthermore, the prescribed pressure - or equivalently the prescribed density ρ_{in} - at the inlet is known as well. It is assumed that u_y , the y -coordinate of the velocity vector \vec{u} , is specified too, e.g., $u_y = 0$ at the inlet. With the help of Eqs. 3.8 and 3.9, it is now possible to determine the velocity component u_x and the unknown populations $f_1, f_5,$ and f_8 .

From Eq. 3.8, it follows that

$$f_1 + f_5 + f_8 = \rho_{\text{in}} - (f_0 + f_2 + f_3 + f_4 + f_6 + f_7). \quad (3.32)$$

Rearrangement of Eq. 3.9, considering the components c_{ix} and c_{iy} of the lattice velocities \vec{c}_i separately, and keeping in mind that $u_y = 0$, yields

$$f_1 + f_5 + f_8 = \rho_{\text{in}} u_x + (f_3 + f_6 + f_7) \quad (\text{from } \sum c_{ix} f_i = \rho_{\text{in}} u_x) \quad (3.33)$$

and

$$f_5 - f_8 = -f_2 + f_4 - f_6 + f_7 \quad (\text{from } \sum c_{iy} f_i = \rho_{\text{in}} u_y = 0). \quad (3.34)$$

Consistency of Eqs. 3.32 and 3.33 and rearrangement of the terms gives u_x :

$$u_x = 1 - \frac{(f_0 + f_2 + f_4 + 2(f_3 + f_6 + f_7))}{\rho_{\text{in}}}. \quad (3.35)$$

The unknown population normal to the inlet, f_1 , can be determined by applying the bounce-back rule for the non-equilibrium part, i.e., $f_1 - f_1^{eq} = f_3 - f_3^{eq}$. By using

furthermore Eq. 3.13 (inserting for f_i^{eq}), one obtains

$$\begin{aligned}
f_1 &= f_3 + (f_1^{eq} - f_3^{eq}) \\
&= f_3 + \rho_{\text{in}} \left(\frac{1}{9} + \frac{1}{3}u_x + \frac{1}{3}u_x^2 - \left(\frac{1}{9} - \frac{1}{3}u_x + \frac{1}{3}u_x^2 \right) \right) \\
&= f_3 + \frac{2}{3}\rho_{\text{in}}u_x
\end{aligned} \tag{3.36}$$

Finally, ‘adding’ Eqs. 3.33 and 3.34 and rearranging the terms yields

$$f_5 = f_7 - \frac{1}{2}(f_2 - f_4) + \frac{1}{6}\rho_{\text{in}}u_x \tag{3.37}$$

and, analogously, ‘subtracting’ Eq. 3.34 from Eq. 3.33 and rearrangement of the terms results in

$$f_8 = f_6 + \frac{1}{2}(f_2 - f_4) + \frac{1}{6}\rho_{\text{in}}u_x. \tag{3.38}$$

Eqs. 3.36, 3.37, and 3.38 with u_x from Eq. 3.35 give the unknown populations for a lattice node at the inlet. In a similar way, the unknown populations f_3 , f_6 , and f_7 for a node at the outlet of the channel can be derived:

$$\begin{aligned}
f_3 &= f_1 - \frac{2}{3}\rho_{\text{out}}u_x \\
f_6 &= f_8 - \frac{1}{2}(f_2 - f_4) - \frac{1}{6}\rho_{\text{out}}u_x \\
f_7 &= f_5 + \frac{1}{2}(f_2 - f_4) - \frac{1}{6}\rho_{\text{out}}u_x
\end{aligned} \tag{3.39}$$

with

$$u_x = \frac{(2(f_1 + f_5 + f_8) + f_0 + f_2 + f_4)}{\rho_{\text{out}}} - 1 \tag{3.40}$$

where ρ_{out} denotes the density imposed at the outlet.

The corner nodes need to be treated separately. In the following, a rough derivation for the top node at the inlet is given. The equations for the three other corner nodes can be obtained in an analogous way. The derivation for the unknown populations at a corner node is similar to the one for an ‘inner’ inlet nodes. At the top inlet corner, ρ_{in} is specified, $u_x = u_y = 0$ and the distributions functions f_0 , f_2 , f_3 , and f_6 are known after propagation, whereas f_1 , f_4 , f_5 , f_7 , and f_8 have to be determined, see Fig. 3.10. The unknown populations normal to the boundary, f_1 and f_4 , can be obtained

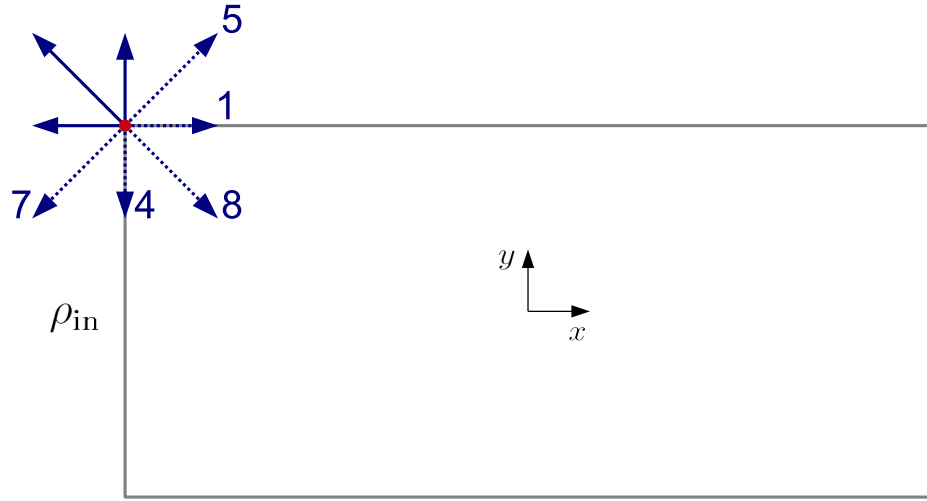


Figure 3.10: Inlet/outlet boundary conditions for a corner node. Dashed arrows indicate unknown populations; full arrows denote known populations.

by applying the bounce-back rule for the non-equilibrium parts, i.e.,

$$\begin{aligned} f_1 &= f_3 + (f_1^{eq} - f_3^{eq}) = f_3, \\ f_4 &= f_2 + (f_4^{eq} - f_2^{eq}) = f_2. \end{aligned} \quad (3.41)$$

The difference $(f_i^{eq} - f_{\bar{i}}^{eq})$ vanishes for $i = 1, 4$ because $u_x = u_y = 0$. f_1 and f_4 can now be inserted in Eqs. 3.37 and 3.38 yielding

$$\begin{aligned} f_5 &= f_7, \\ f_8 &= f_6. \end{aligned} \quad (3.42)$$

Finally, substituting f_7 for f_5 in Eq. 3.32 and rearranging the terms gives

$$f_7 = \frac{1}{2} (\rho_{in} - (f_0 + f_1 + f_2 + f_3 + f_4 + f_6 + f_8)) \quad (3.43)$$

3.3.4.2 Velocity boundary conditions

In a way similar to the pressure boundary conditions, velocity boundary conditions can be prescribed. The derivation is analogous to the one in the previous subsection. For an ‘inner’ outlet node, for example, the prescribed velocity as well as all populations except for f_3 , f_6 and f_7 are known. Using again Eqs. 3.8 and 3.9 and the bounce-back rule for the non-equilibrium part, the density ρ and the missing populations can be

determined. The formulas to impose velocity boundary conditions at the outlet are

$$\rho = \frac{1}{1 + u_x} (f_0 + f_2 + f_4 + 2(f_1 + f_5 + f_8)) \quad (3.44)$$

$$f_3 = f_1 - \frac{2}{3}\rho u_x \quad (3.45)$$

$$f_6 = -\frac{1}{6}\rho u_x + \frac{1}{2}u_y + \frac{1}{2}(f_4 - f_2) + f_8 \quad (3.46)$$

$$f_7 = -\frac{1}{6}\rho u_x - \frac{1}{2}u_y - \frac{1}{2}(f_4 - f_2) + f_5. \quad (3.47)$$

Similar formulas can be derived for the ‘inner’ inlet nodes and the four corner nodes.

The pressure and velocity boundary conditions can also be applied in three dimensions. A derivation of the corresponding formulas for a $D3Q15$ model can be found in [220].

Chapter 4

Fluid-wall interaction

In hemodynamics, the fluid-structure interaction is a real challenge. The walls of a blood vessel are not stiff but show a complex elastic behavior and have a layered inhomogeneous structure (elastin, collagen, and smooth muscle) [85]. The vessel diameter changes in time depending on the pulsatile blood pressure inside which oscillates due to the periodic pumping of the heart. The elastic property of the wall is also essential for the propagation of waves. Therefore, it is of particular importance to include the elasticity of the vessel in models of physiological flows, especially when considering large vessels.

In the case of large arteries, the flow in the vessel can be assumed to be Newtonian. Investigation of non-Newtonian flows in hemodynamics can be found elsewhere [138, 157].

This chapter describes how the elasticity of the vessel is modeled in the lattice Boltzmann framework presented in this work. The results of these simulations will be presented in Chapter 5. The modeling is based on a relation between the pressure and the displacement of the vessel wall, which gives the interaction between fluid and wall. In fact, the flow inside the vessel exerts a force (pressure) on the wall which responds to this force by expanding. It should be noted that the presented modeling of the wall elasticity is not a ‘real’ fluid-structure interaction problem as for example in [23] or [24] because no response from the wall back to the fluid (forces exerted from the wall on the fluid) is included in the model.

4.1 Modeling elastic walls in lattice Boltzmann simulations

In simulations of the blood flow in larger vessels, it is important to include the compliance of the wall. A simple approach has been developed to model the elastic vessel which does not need a parametrization of the wall as for example used in the method of H. Fang et al. [51, 52]. The present modeling is based on the work of D. Leitner [99] and is a local approach as the LB method itself. By this, the complexity of the algorithm is not increased.

4.1.1 Modeling the elastic wall

4.1.1.1 Displacement of vessel wall based on node type changes

For the simulations, the considered computational domain is fixed of dimensions $N_x \times N_y$, where N_x and N_y are the number of lattice nodes in direction x and y , respectively. In the modeling of the vessel wall, the nodes of the lattice can have two different states: *fluid*, representing the blood inside the vessel, and *solid*, denoting the tissue of the vessel. Contrary to the modeling described by D. Leitner [99], the vessel wall is generally not located on the solid nodes but in between fluid and solid nodes. All nodes that are not fluid are by default solid. The approach does not require cellular automata used in Leitner's method to avoid a rupture of the vessel wall. The displacement of the wall is modeled by changing the type of a node - from solid to fluid for an outwards displacement (expansion) and vice versa for an inwards displacement (contraction). The change of node type is dependent on the local pressure of the surrounding fluid nodes. Fig. 4.1 illustrates the concept of wall displacement based on node type changes.

The presented method is an implementation of the hemoelastic feedback system described by Y.C. Fung [61] which consists of two functional units: an elastic body and a pressure induced fluid mechanism. The vessel is considered as a rigid fluid conduit having a certain shape. The pressure corresponding to the given flow is applied as load on the elastic vessel which is treated as an elastic body in terms of elasticity theory. The result of the computation is then used to update the wall shape of the vessel.

In the following, the terms *destruction* and *creation* of nodes are used to signify the

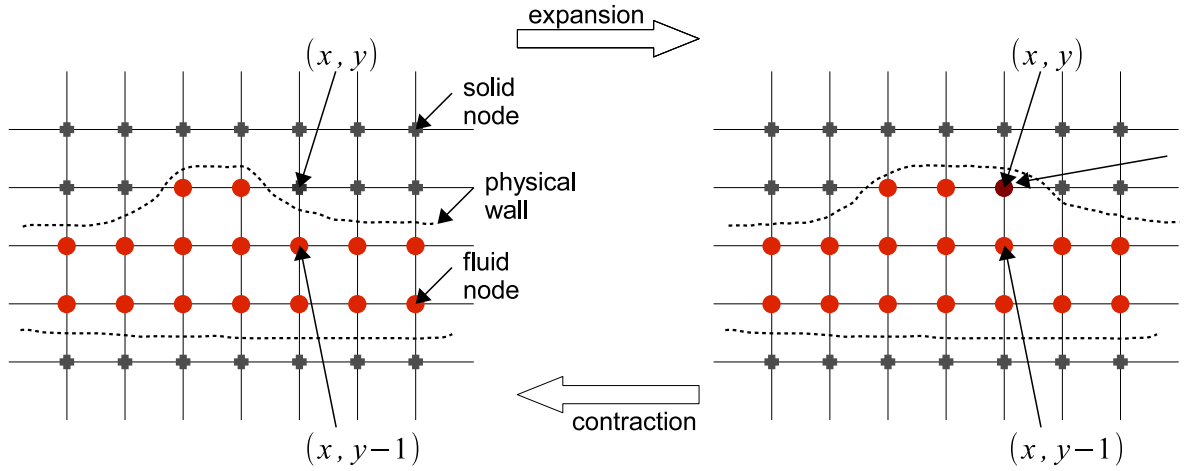


Figure 4.1: Sketch of lattice illustrating the concept of wall displacement based on node type changes. Gray crosses indicate solid nodes; red filled circles denote fluid nodes. The dark red disk designates a node that has changed its type. The virtual wall (dashed line) separates the solid and the fluid domain.

state change of a node. It must be clear that in this type of modeling, nodes are neither destroyed nor created - the geometrical domain being fixed of dimensions $N_x \times N_y$ - but that nodes change only their type. The state change ‘fluid to solid’ will be termed as *destruction* and ‘solid to fluid’ as *creation*.

4.1.1.2 Initialization of new fluid nodes

New fluid nodes need to be initialized with values of the density ρ and the velocity \vec{u} which are computed based on the populations f_i from the neighboring fluid nodes. Fig. 4.2 illustrates this initialization procedure. When determining the populations f_i at the new fluid node (x, y) , three cases can occur:

- If the neighboring nodes of (x, y) in direction i and opposite direction \bar{i} are both solid, f_i and $f_{\bar{i}}$ are set to their equilibrium value f_i^{eq} and $f_{\bar{i}}^{eq}$, respectively.
- If the neighboring nodes of (x, y) in direction i and \bar{i} are both fluid, f_i and $f_{\bar{i}}$ are gained from propagation.
- If the neighboring node of (x, y) in direction i is fluid and the neighboring node of (x, y) in direction \bar{i} is solid, $f_{\bar{i}}$ is gained from propagation and f_i is calculated using the bounce-back rule for the non-equilibrium part of the distribution function f_i ($f_i = f_{\bar{i}} + (f_i^{eq} - f_{\bar{i}}^{eq})$, see [220]).

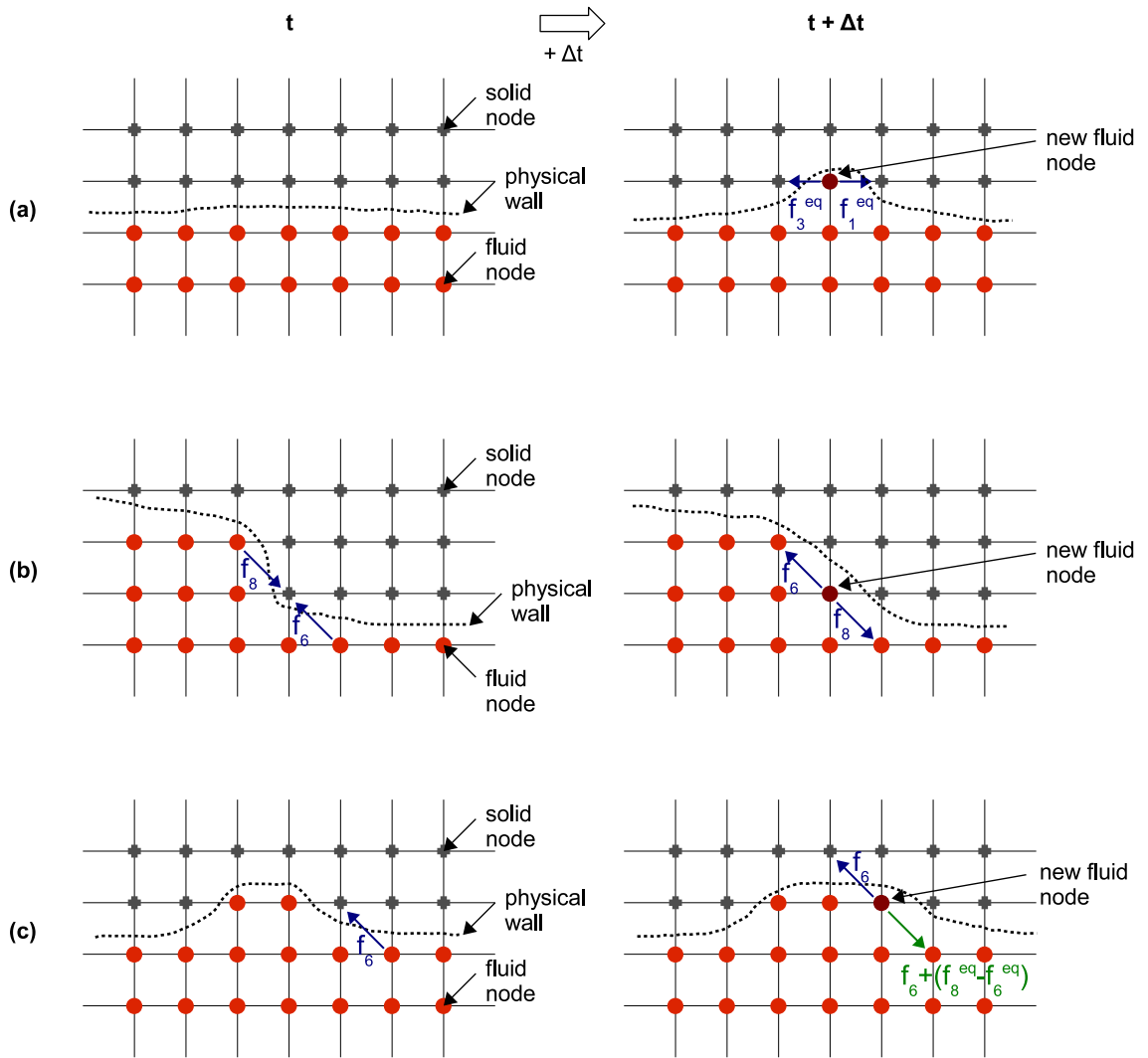


Figure 4.2: Sketch of the initialization of new fluid nodes (dark red disks). (a) Example of a new fluid node having solid neighbors in direction 1 and 3. f_1 and f_3 at the new fluid node are set to their equilibrium values. (b) Example of a new fluid node having fluid neighbors in direction 6 and 8. f_6 and f_8 at the new fluid node are gained from propagation. (c) Example of a new fluid node having a fluid neighbor in direction 8 and a solid neighbor in the opposite direction (6). At the new fluid node, f_6 is gained from propagation and f_8 using the bounce-back rule for the non-equilibrium part.

Compared to the method of D. Leitner [99], who initializes new fluid nodes with an equilibrium distribution function, this procedure includes also the non-equilibrium part of the populations, which is not negligible in proximity of the wall.

4.1.2 Population rescaling methods

A mass conservation problem arises when nodes change their type because the total number of fluid nodes changes. Mass is a priori not conserved as mass is added when initializing new fluid nodes or subtracted when a node changes its state from fluid to solid. Leitner [99] does not address this issue, and it is not clearly evidenced how this is circumvented. In order to ensure mass conservation in an isolated system, methods have been developed [40] that rescale the LB populations in a part of the domain when a node type change occurs and so ensure mass conservation.

Mass conservation is imposed each time fluid nodes change their type (from solid to fluid in the case of expansion and vice versa in the case of contraction of the vessel). Two methods to rescale the populations are presented below.

4.1.2.1 Local rescaling

The local rescaling (LR) takes into account only the nearest neighbors of the node changing its state. Fig. 4.3 shows in which domain (blue frame) the LB populations are rescaled when using the LR method. At expansion, mass (density) is redistributed in the following way: Let (x, y) be a node changing its state from solid to fluid and $\sum \rho_{nb}$ the sum of the densities at fluid nodes neighboring node (x, y) . After initializing the new fluid node (x, y) , its populations and those from the neighboring fluid nodes are rescaled by the factor

$$\frac{\sum \rho_{nb}}{\sum \rho_{nb} + \rho(x, y)}.$$

Density and velocity are computed based on these new populations. In this way, mass is conserved. The scaling factor is equal to the fraction

$$\frac{\text{old local mass}}{\text{new local mass}}$$

and is smaller than 1. This approach models the transfer of mass to a new fluid node from the neighboring nodes.

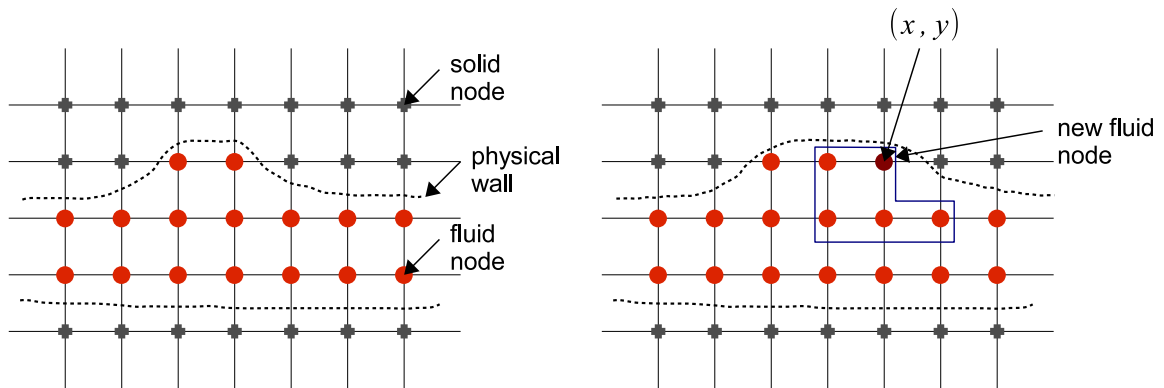


Figure 4.3: Sketch of lattice showing which nodes (domain inside the blue frame) are affected by the local rescaling method

In a similar way, mass is redistributed locally when a fluid node is destroyed, i.e., when a node changes its state from fluid to solid (contraction). The scaling factor is in this case greater than 1. All fluid nodes surrounding the disappearing fluid node are rescaled by this scaling factor. By this procedure, mass is transferred from the destroyed node to the neighboring fluid nodes.

The local rescaling influences the flow field in the vessel only locally. Depending on the fluid viscosity and the vessel geometry, it takes a certain time until this perturbation of the flow field is damped in the simulation, see Chapter 5.

4.1.2.2 Rescaling by columns

As an alternative to the LR approach, the rescaling by columns (CR) method has been developed. This method of rescaling takes into account the whole column of nodes - the vessel can be considered as a sequence of 'rings' adjoint to each other - in which a node type change occurs, see Fig. 4.4. When a node next to the wall changes its state (from solid to fluid or vice versa), the populations of every node in the same column are rescaled to ensure mass conservation (with a rescaling factor similar to the one above).

4.1.3 Continuous bounce-back boundary condition

For the exact wall boundary location, the bounce-back scheme in combination with spatial interpolation (continuous bounce-back boundary condition, see Section 3.3.3)

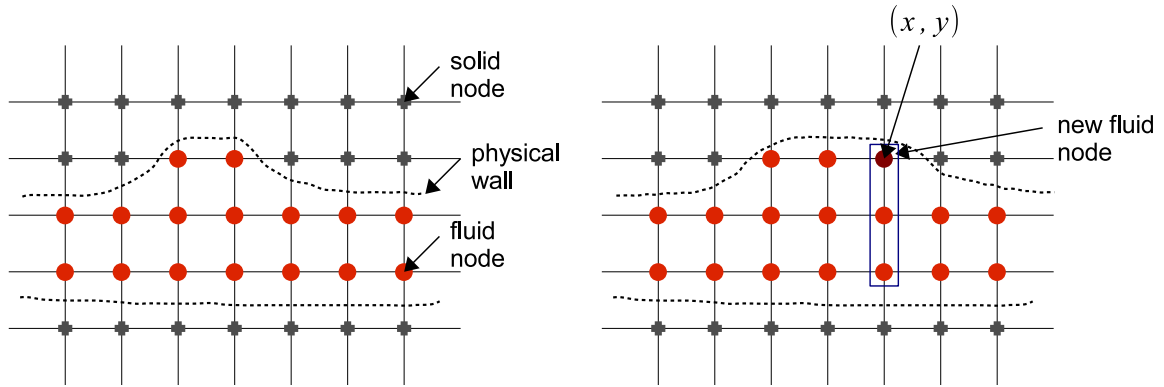


Figure 4.4: Sketch of lattice showing which nodes (domain inside the blue frame) are affected by the rescaling by columns method

is applied to reduce discretization errors. The linear interpolation given by Eqs. 3.29 and 3.30 is used to determine the unknown distribution functions near the wall with directions pointing into the fluid domain. It is applied to all lattice links that cross the virtual wall. The method allows a continuous displacement of the wall because the wall can be placed arbitrarily between fluid and solid nodes.

As in Section 3.3.3, let q denote the distance of the wall from the last fluid node (see Fig. 4.5). With $\Delta x = 1$, q ranges between zero and one. The continuous bounce-back boundary condition allows that the value of q is different at every node \vec{x}_j .

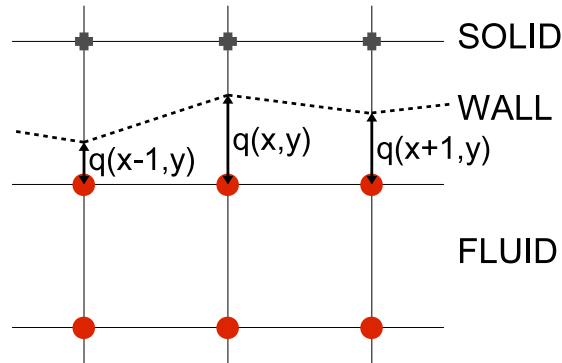


Figure 4.5: Continuous bounce-back boundary condition for a virtual wall located at distance q from the last fluid node. To every fluid node next to the wall a different q is assigned. Gray crosses indicate solid nodes; red filled circles denote fluid nodes. The lattice spacing Δx is set to one.

In the simulations, two arrays of q -values are used, one for the lower and one for the upper boundary. Thus, for every fluid node (x, y_b) next to a boundary, $q_b(x) = q(x, y_b)$ determines the distance from node (x, y_b) to the wall. Here, the subscript in y_b specifies whether the lower boundary ($b = \text{lower}$) or the upper boundary ($b = \text{upper}$)

is considered. For the sake of simplicity, the subscript is omitted in cases in which it is not necessary to specify which boundary is considered.

The parameter q of a certain node next to the boundary is linked to the pressure at this node. More details about the exact relationship between q and the pressure are described further down. The approach of coupling q with the pressure and using continuous bounce-back boundary conditions at the wall allows a more gradual displacement of the (virtual) wall instead of moving the vessel wall by one lattice unit within a single time step [39].

The virtual radius $R(x)$ at a position x of the channel is introduced to specify the exact distance of the wall from the centerline of the channel. It can be calculated in the following way:

$$R(x) = \frac{q_{\text{upper}}(x) + (y_{\text{upper}}(x) - y_{\text{lower}}(x)) + q_{\text{lower}}(x)}{2} \quad (4.1)$$

where q_{upper} and q_{lower} denote the distance of from upper/lower wall to the fluid nodes directly next to this virtual wall.

4.2 Pressure thresholds

The change of node type is dependent on the local pressure surrounding a considered node. Subject to this pressure, the wall is displaced. Pressure thresholds are assigned to each node, increasing with the distance from the vessel centerline. Nodes located further away from the center of the vessel have a higher threshold so that a higher pressure is needed for an outwards displacement of the wall, i.e., for changing the type of a node from solid to fluid.

For the simulations described in Chapter 5, a linear relationship between the pressure p and the radius R is assumed (see Section 2.3.2), similar to the one of the pulmonary blood vessels (see Y.C. Fung [61]), and the pressure thresholds p_{th} are computed based on this relationship:

$$p_{th} = p_0 + \alpha(R - R_0) \quad (4.2)$$

Here, α is a compliance constant. R_0 is the radius when the transmural pressure ($p - p_0$) is zero and $p_0 = p(R_0)$. The relation given by Eq. 4.2 is a good approximation for

large arteries [80].

The pressure thresholds are assigned to each node. Relation 4.2 means that the pressure threshold is equal to the pressure necessary to balance the restoring forces from the elastic vessel wall [46]. The criterion for changing the type of a node is related to the parameter q of the continuous bounce-back boundary condition and will be explained in the next section.

In literature, other nonlinear relations between pressure and radius are available, see for example Eq. 2.46. The advantage of the presented method for modeling elastic walls is that any linear or nonlinear relationships between p and R can apply provided that they are explicit. Eq. 2.46 for example can be rearranged giving an explicit nonlinear relation between p and R :

$$p = p_0 + E h \left(\frac{1}{R_0} - \frac{1}{R} \right) \quad (4.3)$$

Here, E denotes the Young's modulus and h is the wall thickness.

4.3 The moving wall mechanism: coupling between pressure threshold and parameter q

The parameter q is related to the pressure in the following way. Let $p(x, y_b)$ denote the current pressure at a fluid node (x, y_b) directly next to the wall and $p_{th}(x, y_b)$ the pressure threshold at this node. The difference to the pressure threshold of the neighboring node (in y -direction) is given by the parameter α in the linear pressure-radius relationship, see Eq. 4.2. At every time step, the parameter q is updated based on the following relationship.

$$q(x, y_b) = \frac{p(x, y_b) - p_{th}(x, y_b)}{\alpha} \quad (4.4)$$

q changes at every time step at each x because it is related to the pressure which varies in time. q increases as p increases and, vice versa, q decreases as p decreases. The value of q determines whether a node type change occurs or not. If q becomes greater than one because of a large pressure increase (thus, $p(x, y_b) - p_{th}(x, y_b) > \alpha$), the solid node next to the considered fluid node (x, y_b) changes its state to fluid. On the other way around, if q falls below zero because of a large pressure decrease ($p(x, y_b) < p_{th}(x, y_b)$), the node (x, y_b) changes its state from fluid to solid.

As soon as a node type change occurs (which happens when $q > 1$ or $q < 0$), q has to be reset to a value between zero and one. This is done in the following way. If q exceeds one, thus $q = 1 + \Delta q$ with $\Delta q > 0$, the new q is set to Δq if $\Delta q < 1$ and set to one if $\Delta q > 1$. In a similar way, if q falls below zero, thus $q = -\Delta q$ with $\Delta q > 0$, the new q is set to $(1 - \Delta q)$ if $\Delta q < 1$ and to zero if $\Delta q > 1$.

Compared to the method of D. Leitner [99] with which wall displacements of less than one lattice unit were not possible, the described approach allows a continuous displacement of the vessel wall. The populations at a node next to the wall are corrected many times before the node changes its state. As a consequence, the system is less perturbed when a node type change occurs (see Chapter 5).

Chapter 5

Simulations and results

This chapter starts with the computational aspects of the simulations that have been performed for this work and which are based on what has been described in the previous chapters. The structure of the implemented program including the lattice Boltzmann algorithm and the modeling of the elastic wall is given as well as some details about the memory requirements.

The main part of the chapter is dedicated to numerical experiments that have been carried out to show the feasibility and physical correctness of the developed approach for modeling incompressible flow in distensible tubes. Several results are presented corresponding to simulations including the theory and methods described in the previous chapters.

The last section of this chapter presents the concept of Windkessel. In order to better reproduce physiological cases, the lattice Boltzmann method has been coupled with a Windkessel model for the outlet boundary condition. Preliminary results from first test simulations will be given at the end of this chapter.

5.1 Computational aspects

A simulation software for the LB algorithm combined with the elastic wall model has been implemented using the programming language C. The code includes the rescaling methods and the pressure threshold algorithm described in Chapter 4. Using this software program, numerical experiments have been conducted to show the effectiveness

of the presented approach. It should be noted that the focus in the simulations is not on the computational efficiency of the method but on the feasibility of the algorithm. Readers interested in code optimization and performance are referred to other authors (R. Argentini et al. [6], W. Guo et al. [66], C. Pan et al. [143], M.D. Mazzeo and P.V. Coveney [117], G. Wellein et al. [200]). These references treat other LB algorithms, not to the one described here, but anyway the reader can borrow some ideas of code optimization for LB algorithms in the cited literature.

For the simulations, a so-called D2Q9 model (two spatial dimensions, nine directions i , see Fig. 3.3) is considered and calculations are based on the lattice Boltzmann equation with single-time relaxation (LBGK approximation), see Eq. 3.11.

The figures in this chapter have been generated with MATLAB from the data resulting from the simulations in C. The units in the plots are LB units (non-dimensionalized) if not otherwise specified.

5.1.1 Computational domain

The computational domain is a Cartesian lattice of dimensions $N_x \times N_y$. As already mentioned in the previous chapter, every node can have two different states: fluid or solid. Solid nodes indicate the tissue of the vessel, fluid nodes refer to the blood inside the vessel. The wall of the vessel can be imagined to be a moving interface between solid and fluid nodes. The vessel under investigation is incorporated in the computational domain with fixed dimensions $N_x \times N_y$, see Fig. 5.1.

5.1.2 Structure of the program

The flow chart in Fig. 5.2 illustrates the implemented lattice Boltzmann algorithm. After initialization of the lattice, the steps in the flow chart are processed at every time instant. It should be noted that there exists a parameter q for every node (every x) at the lower and upper boundary of the channel.

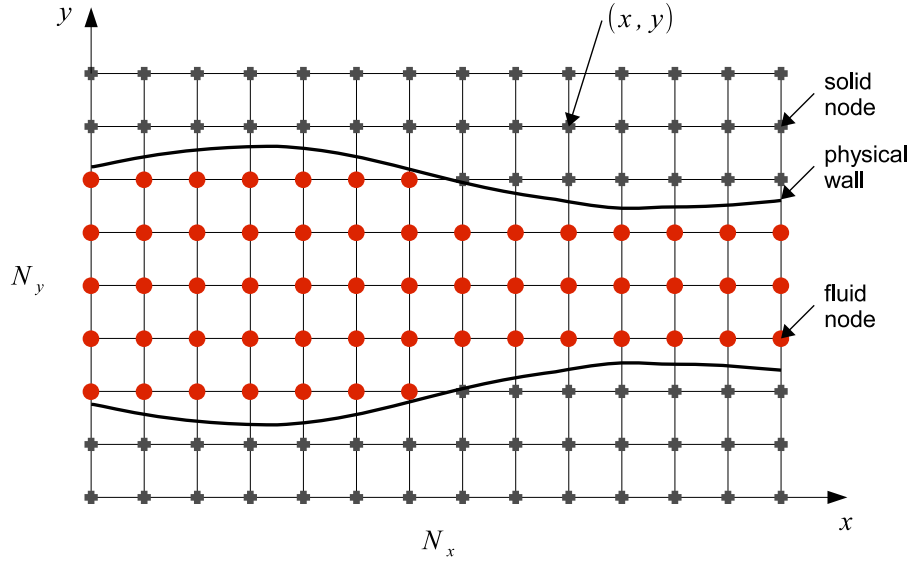


Figure 5.1: *Sketch of lattice with embedded vessel*

5.1.3 Memory requirements

For the simulations, values for many variables (density ρ , velocity components u_x and u_y , the distribution functions f_i , etc.) have to be stored for every node. In order to facilitate the data access, the values are stored sequentially in a vector. Helper functions are used to get the position in this linear vector corresponding to the value needed. Fig. 5.3 illustrates the access of memory.

5.1.3.1 Fundamental and derived variables in memory

Many variables have to be stored for each node. Thus, it is important to allocate memory for each of them. The fundamental and main derived variables are listed below.

Fundamental (primary) variables:

- *node type* (fluid, solid) \Rightarrow defines the geometry of the vessel
- *distribution functions* f_i (nine directions per node) \Rightarrow define the fluid dynamics

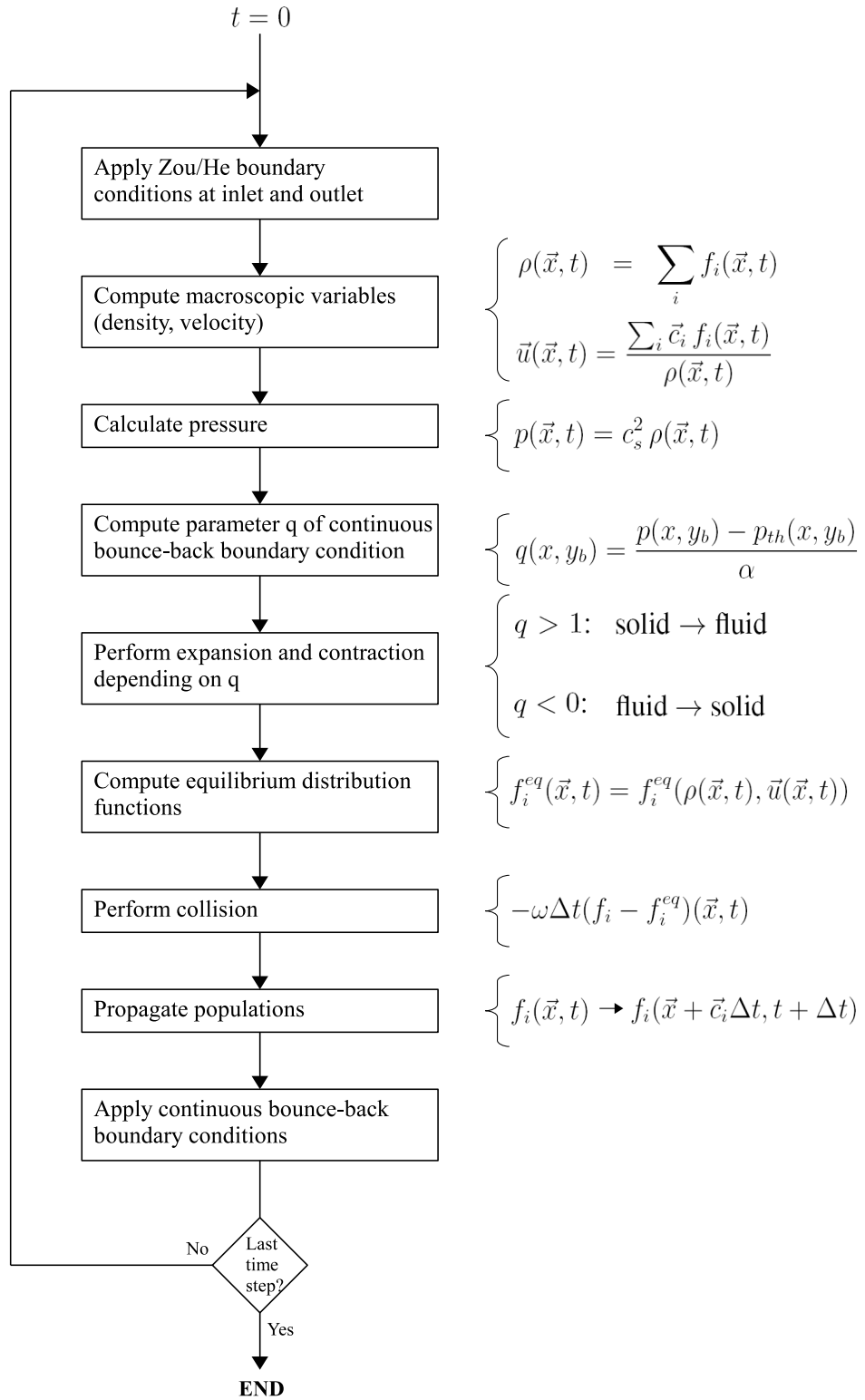


Figure 5.2: Flow chart of the implemented lattice Boltzmann algorithm

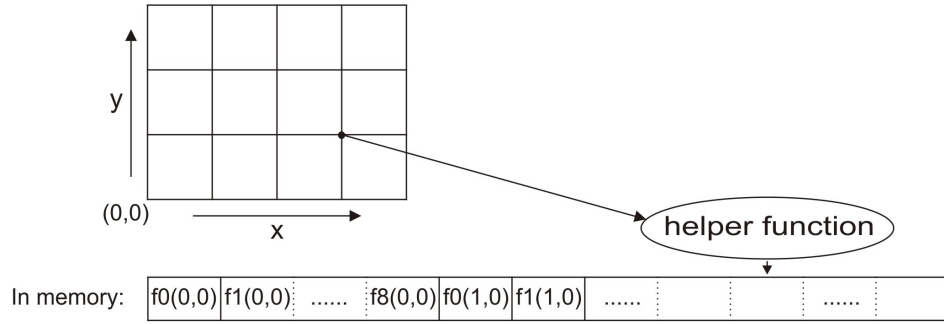


Figure 5.3: Example of memory allocation for the distribution functions $f_i(x, y)$. The helper function translates x , y and i from a matrix form to the position in the linear array.

| Size of lattice $N_x \times N_y$ | Memory for primary variables (kB) | Memory for secondary variables (kB) | Total memory (kB) |
|-------------------------------------|--------------------------------------|--|-----------------------------|
| 200×100 | 1460 | 640 | 2100 |
| 400×100 | 2920 | 1280 | 4200 |
| 500×60 | 2190 | 960 | 3150 |
| 1000×60 | 4380 | 1920 | 6300 |

Table 5.1: Memory requirements for the main variables for a D2Q9 lattice of dimensions $N_x \times N_y$

Derived (secondary) variables:

- density ρ
- components u_x and u_y of the velocity \vec{u}
- pressure thresholds p_{th}

5.1.3.2 Examples for memory usage

Besides the node type, whose data type is a ‘character’ (1 byte per node), all other variables are of the data type ‘double’ (8 bytes per node). The variable ρ for example occupies $(N_x \cdot N_y \cdot \text{sizeof}(\text{double}))$ bytes in memory, whereas the variable f_{in} (containing the f_i ’s for all nine directions i) is allocated with $(9 \cdot N_x \cdot N_y \cdot \text{sizeof}(\text{double}))$ bytes. Table 5.1 lists some examples of memory needed in total for the fundamental and main derived variables for different sizes of the lattice.

5.2 Numerical experiments

5.2.1 Simulations with periodic boundary conditions

The main objective of the numerical experiments presented in this chapter is to prove that the model provides correct physical behavior.

As first experiment, a straight channel with flat walls modeling the vessel is considered. Periodic boundary conditions are imposed in direction of the channel to model an infinite long tube. This condition will be replaced by inlet/outlet boundary conditions in the next section. At the wall, halfway bounce-back on the link boundary conditions are imposed which represent a no-slip condition (i.e., the fluid velocity at the wall is zero). Furthermore, the pressure is increased ‘manually’ at a certain time, just enough to induce an increase of the channel radius of one unit (expansion), and at a later time decreased again, just enough to induce a decrease of the radius of one unit (contraction). Thus, the behavior of the flow field for only one cycle of expansion and subsequent contraction (of the whole channel) is investigated. Here and in the following, ‘cycle’ denotes the sequence of an expansion followed by a contraction back to the initial state. In a later stage, the manual procedure of pressure increase/decrease will be replaced by an oscillating pressure gradient consequent on the periodic pumping of the heart.

As mentioned above, a straight channel of width H is considered. The values of macroscopic variables ρ (and thus p) and \vec{u} are symmetric with respect to the centerline. Thus, the pressures at nodes with the same y -coordinate are equal. Furthermore, all nodes with the same y -coordinate have the same pressure threshold. Under this assumption, the flat wall is displaced uniformly at all nodes with the same y -coordinate (i.e., one layer of nodes) within a single time step.

To induce an expansion in the presented model, the pressure is increased explicitly by adding an amount Δp to the pressure of all fluid nodes at a certain time t_{add} and then decreased again at time $t_{\text{sub}} > t_{\text{add}}$. Δp is chosen in a way that the wall is moved by only one layer at the lower and upper boundary. Due to the forced increase (decrease) of pressure at t_{add} (t_{sub}), mass increases (decreases) by a value proportional to Δp at t_{add} (t_{sub}).

In order to check whether the implemented method provides correct physical behavior,

the following steps are executed:

1. Wait for fully developed flow (until time t_0).
2. At time t_0 ($= t_{\text{add}}$), when the flow is fully developed, add mass by adding a small value Δf_i to the populations f_i at each node. This corresponds to an increase of pressure by $\Delta p = c_s^2 \Delta \rho$ in each node, with $\Delta \rho = \sum_{i=0}^8 \Delta f_i$ and $c_s = 1/\sqrt{3}$ being the speed of sound. Then wait for the flow to be fully developed (until time t_1).
3. At time t_1 , expansion occurs because the pressure thresholds at the wall are exceeded due to the increase of pressure at time t_0 . The channel is expanded by one layer at the upper and lower wall, respectively. The populations f_i are rescaled so as to ensure mass conservation. Then wait for fully developed flow (until time t_2).
4. At time t_2 ($= t_{\text{sub}}$), reduce mass by subtracting Δf_i from the populations f_i at each node. This corresponds a decrease of pressure. Wait again until flow is fully developed (until time t_3).
5. At time t_3 , contraction occurs because the pressure has fallen below the pressure threshold due to the decrease of pressure at time t_2 . The radius of the channel is reduced by one unit, so one layer of nodes is destroyed at the lower and upper wall, respectively. The populations f_i are rescaled so as to ensure mass conservation.

In this procedure, it is ensured that mass is conserved any time except when mass is added (step (2)) or subtracted (step (4)) by proper rescaling.

The results of this procedure are presented hereafter.

5.2.1.1 Simulation parameters

For the simulations, the following physical parameters have been used: viscosity $\nu = \frac{1}{3}$, maximum velocity $U_{\text{max}} = 0.01$, and initial density $\rho_0 = 1.0$. All parameters and variables are normalized and hence dimensionless. The computational domain has 200×100 nodes and the initially straight channel is of dimensions 200×40 .

5.2.1.2 Comparison between analytical and numerical solution

The analytical solution of a two-dimensional fully developed steady flow in a channel of width $H = 2R$, where R is the radius, driven by a constant pressure gradient G and with constant viscosity ν (Newtonian flow assumed) is given by the following formula (Poiseuille flow):

$$u_{\text{analytical}}(y) = \frac{G(R^2 - y^2)}{2\nu} \quad (5.1)$$

The pressure gradient G is given by

$$G = \frac{8\nu U_{\text{max}}}{H^2}. \quad (5.2)$$

The simulation output has been compared with the analytical solution using the same parameters. Fig. 5.4 displays the velocity profile of the exact solution and the result of the numerical simulation of a symmetric straight channel. It can be observed that the computed velocity profile (blue crosses) and the analytical solution by Poiseuille (green dashed line) coincide.

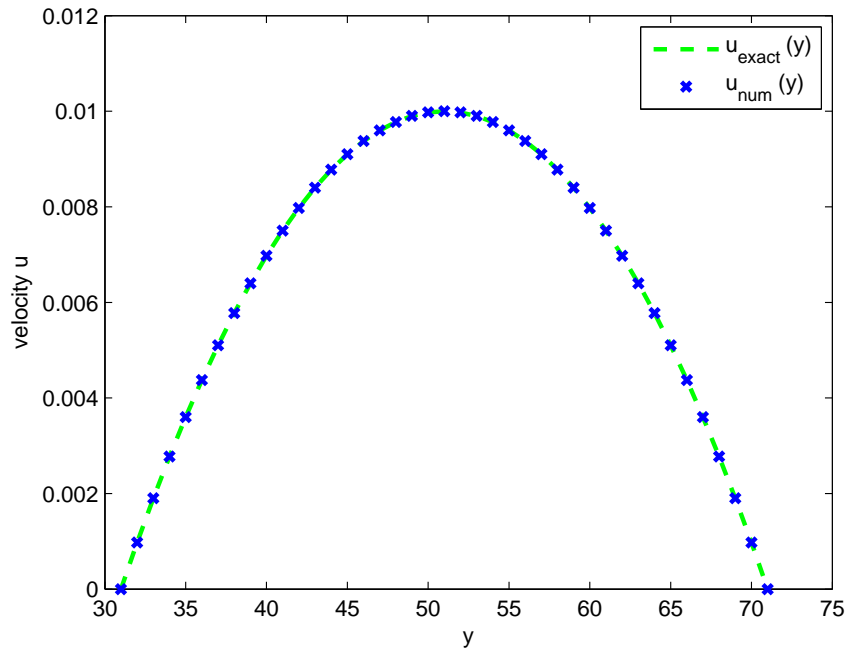


Figure 5.4: Velocity: Comparison between analytical solution of Poiseuille (green) and numerical result (blue) (periodic BC)

Fig. 5.5 represents the velocity field of the fully developed flow in the rigid straight

channel. The maximum velocity of 0.01 (compare with Fig. 5.4) is correctly reached in the center of the channel.

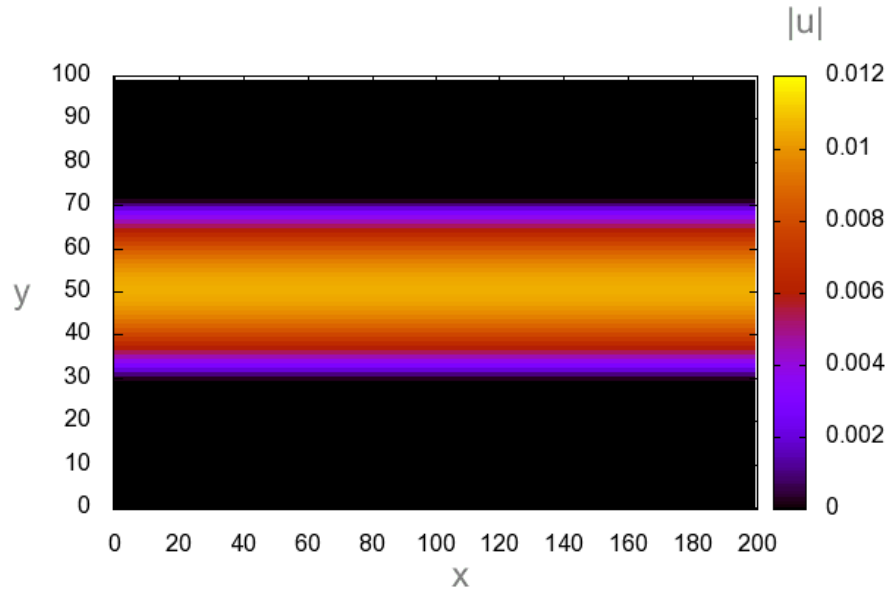


Figure 5.5: *Velocity field of fully developed flow in a rigid straight channel. The black area corresponds to solid nodes.*

5.2.1.3 Approach for testing the modeling of elasticity using local rescaling

A simulation in the straight channel using the local rescaling (LR) method has been carried out to show that it follows expected physical behavior. The procedure described below is only an artificial setup to enforce expansion and contraction through pressure increase/decrease for conducting this simulation experiment.

For this simulation, the problem of expansion and contraction has been separated in the parts explained in Section 5.2.1 and local rescaling has been used.

Fig. 5.6 shows the total mass (sum of the density ρ at each fluid node of the lattice) over time. It can be seen that mass is conserved at expansion (occurring at time $t = 3101$) and contraction (occurring at time $t = 4276$). After the wall has recovered its initial position again and the flow its initial state, i.e., after having performed the steps (1) to (5) cited above, the value of the total mass is the same as the initial value. However,

to reach the same value of the total mass as at the beginning, Δf_i in step (4) has to be multiplied by $\frac{H}{H+2}$, H being the width of the initial channel. This is due to the fact that the diameter (width) of the channel increases by 2 after expansion, i.e., there are two layers of fluid nodes more than before expansion. Thus, Δf_i , being subtracted at every node, has to be reduced by this proportionality factor to take into account the increase of nodes.

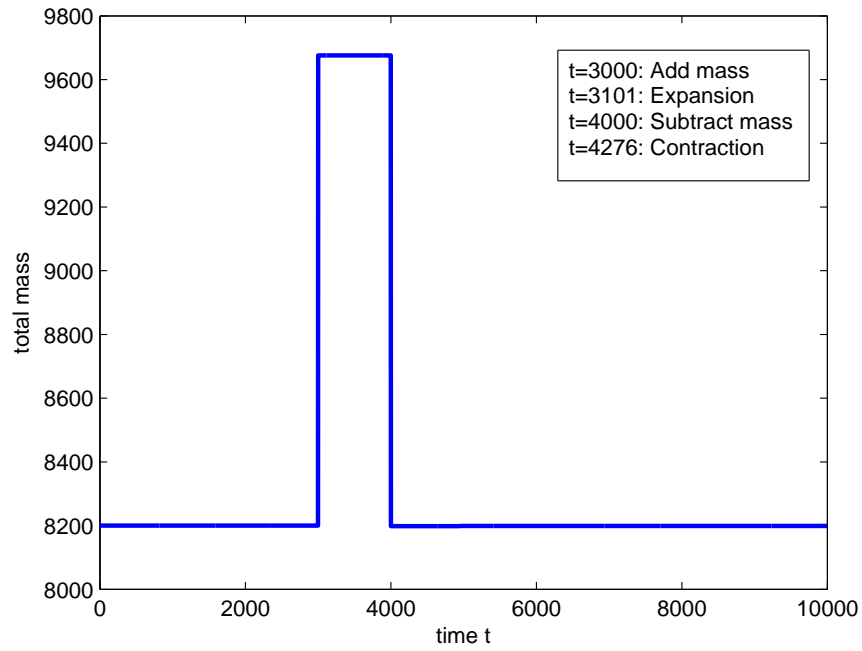


Figure 5.6: *Total mass as a function of time. In order to better distinguish between the single steps (1. to 5., see text), the algorithm waits for at least 100 time steps and for fully developed flow before performing the next step.*

Fig. 5.7 depicts the density at a fluid node next to the wall resulting from this simulated experimental setup. It can be observed that the density oscillates after expansion or contraction due to the propagation of the local perturbation throughout the channel (oscillation period) created by the local rescaling. The duration of the oscillations is influenced by the fluid parameters (viscosity). The value of ρ returns to the initial value after one cycle (expansion and subsequent contraction). Due to the local rescaling of the populations at the changed nodes and their neighbors, the value of ρ decreases at expansion and increases at contraction.

The resulting velocity component u_x at a fluid node next to the wall is displayed in Fig. 5.8. Small oscillations occur at expansion and contraction due to the local

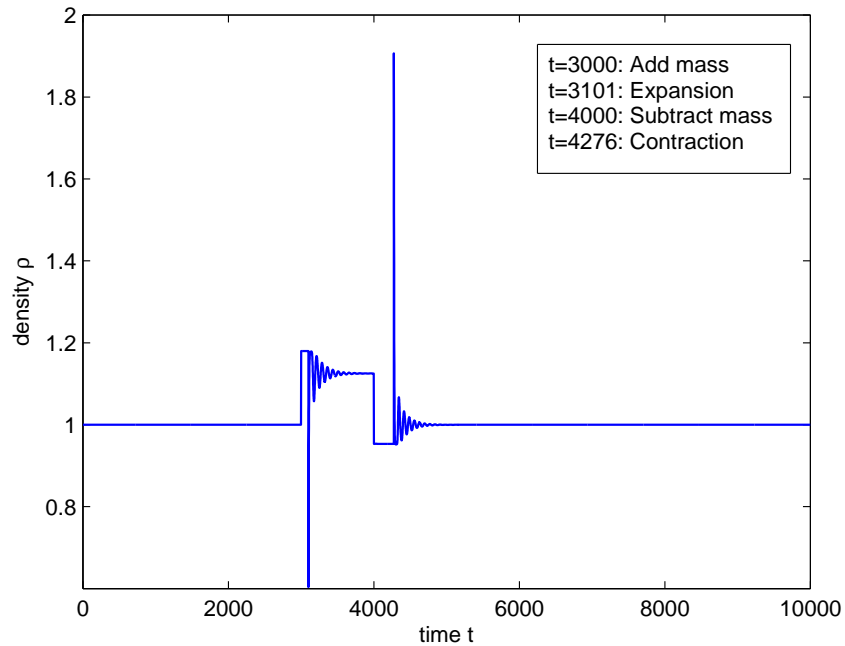


Figure 5.7: *Density at fluid node next to the upper wall as a function of time (local rescaling used)*

perturbation of the flow field. After one cycle of full expansion and contraction, the value of u_x returns to the initial value (when flow is fully developed).

The velocity component normal to the wall, u_y , is depicted in Fig. 5.9. Similarly to u_x , oscillations can be observed at expansion and contraction. However, they are damped much faster than those occurring for u_x . Except for those oscillations, the value of u_y is almost zero at the fluid node next to the wall. This underlines that the no-slip condition is fulfilled at the virtual wall situated halfway between last fluid and first solid node.

The simulation results presented in this subsection show expected physical behavior. Mass is conserved and initial values of the density and the velocity are recovered after one cycle of expansion and subsequent contraction. The oscillatory transient lasts a few hundred time steps, which is an expected duration for the chosen viscosity. As described, the method works strictly locally as does the lattice Boltzmann method itself. This allows straight-forward implementation of the method in LB simulations and makes it suitable for parallel computation.

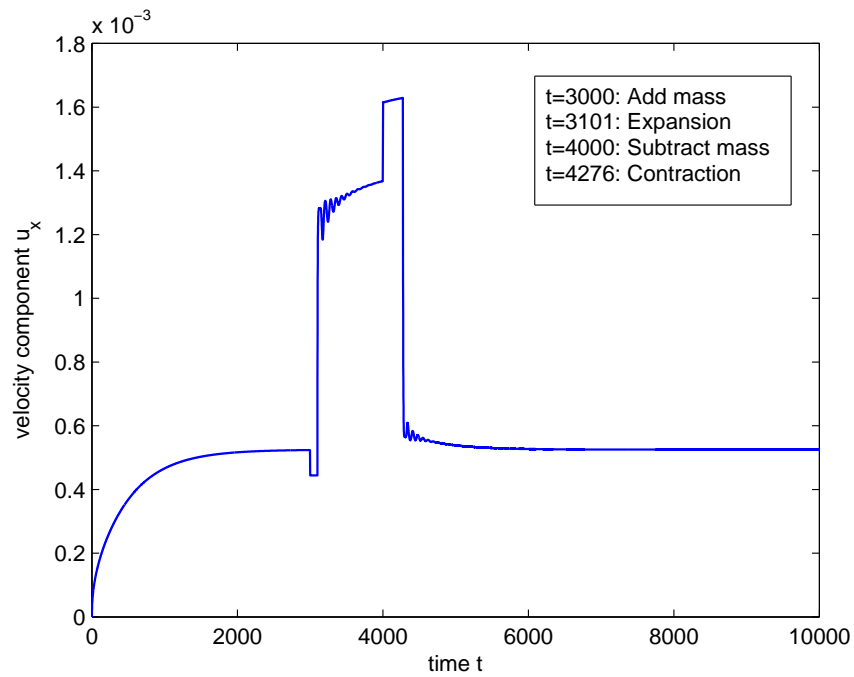


Figure 5.8: Velocity component u_x at fluid node next to the upper wall as a function of time (local rescaling used)

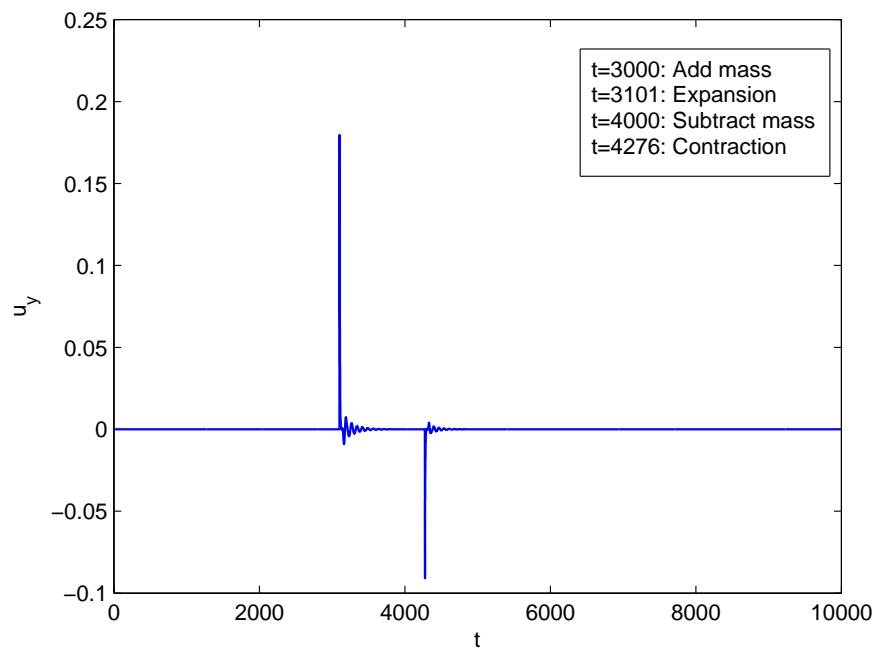


Figure 5.9: Velocity component u_y at fluid node next to the upper wall as a function of time (local rescaling used)

5.2.1.4 Approach for testing the modeling of elasticity using rescaling by columns

For this simulation, the same steps (1)-(5) cited in Section 5.2.1 have been performed and rescaling by columns (CR) has been used. The time history of the total mass shows the same behavior as the one for the LR method and is omitted. Contrary to the LR method, where contraction (as well as expansion) occurs at both the upper and lower wall at the same point in time in the simulation, the contraction of the channel when using rescaling by columns is split into two steps. First, contraction at the lower boundary occurs followed by a contraction at the upper boundary a few hundred time steps later. This is related to the order in which the lattice nodes are processed in the implementation (here, from lower to upper boundary). Since rescaling by columns does not affect only the nearest neighbors of a node becoming fluid (as in the LR method) but the populations of all nodes in the same column, a node type change at the lower wall affects the flow field at the upper wall in the same time step. As a consequence, the condition for expansion or contraction at the upper wall is not necessarily fulfilled anymore as soon as a node type change (and thus rescaling of the whole column) has occurred at the lower wall.

Fig. 5.10 displays the density at a fluid node next to the wall. It can be observed that the density oscillates much less after expansion (contraction) compared to the oscillations occurring with the LR method as local perturbations are limited. Furthermore, oscillations are completely absent at contraction. The value of ρ returns to the initial one after one cycle (expansion and subsequent contraction) as expected.

The time history of the velocity component u_x at a fluid node next to the wall, depicted in Fig. 5.11, exhibits a similar shape as the time history of u_x when using local rescaling, but without oscillations at expansion and contraction. After one cycle, the initial value of u_x is recovered.

The velocity component normal to the wall, u_y , is displayed in Fig. 5.12. Oscillations can be observed at expansion but not at contraction. Except for those oscillations, the value of u_y is almost zero for a fluid node next to the wall (no-slip condition).

Although the CR method provides expected physical behavior (mass conservation, recovery of the initial values after one cycle) and minimizes local perturbation, it exhibits the drawback that node type changes at one wall boundary affect the flow field within the whole channel without propagation latency. Since this specific effect

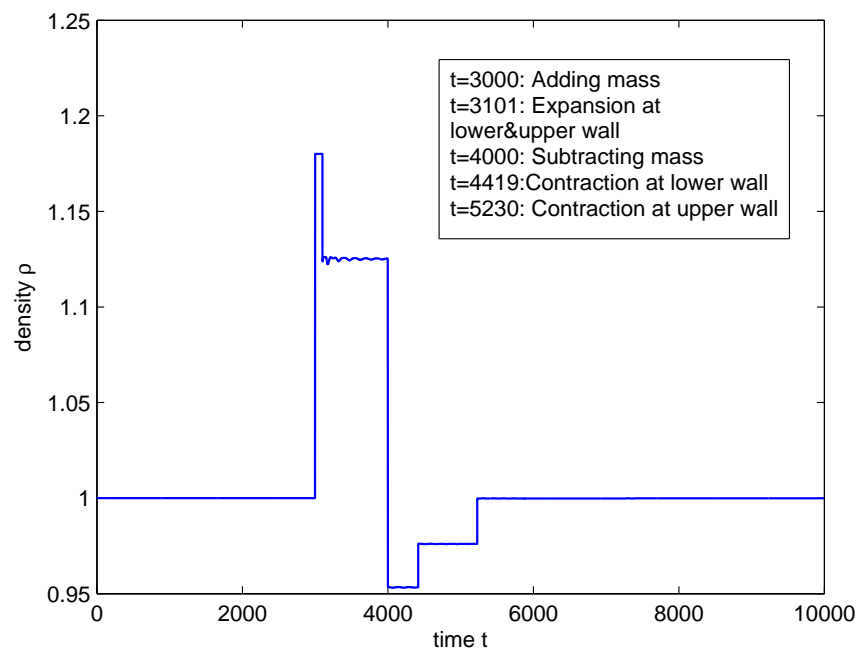


Figure 5.10: *Density at fluid node next to the upper wall as a function of time (rescaling by columns used). Since rescaling by column affects the flow field in the whole channel, expansion and contraction can occur at different points in time.*

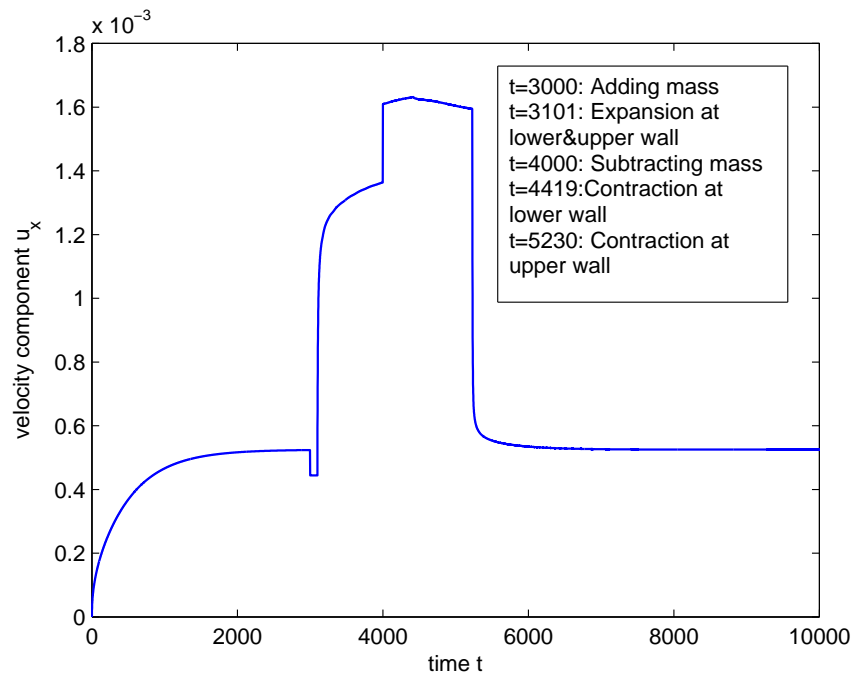


Figure 5.11: Velocity component u_x at fluid node next to the upper wall as a function of time (rescaling by columns used)

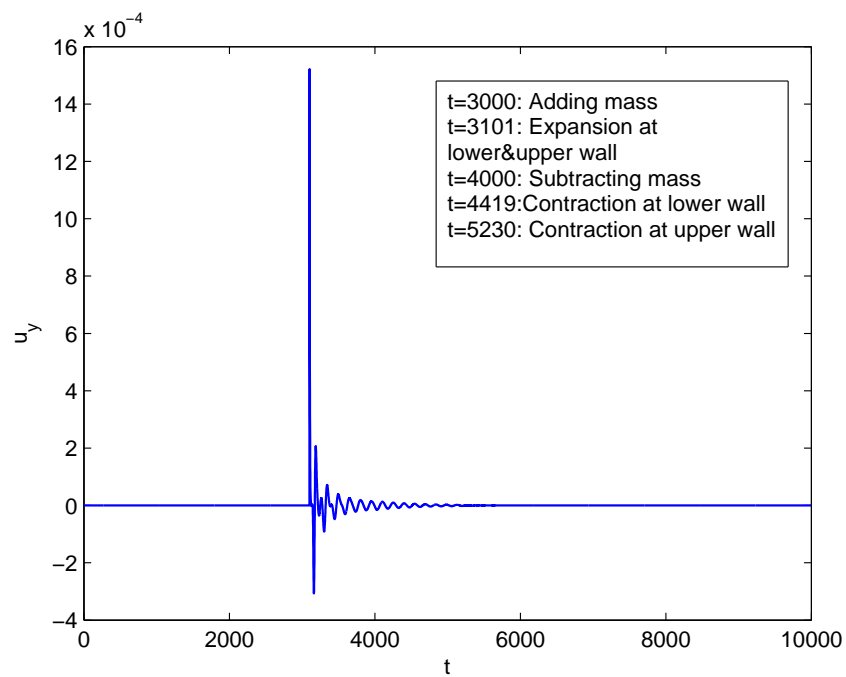


Figure 5.12: Velocity component u_y at fluid node next to the upper wall as a function of time (rescaling by columns used)

does not correspond to real fluid dynamics, the method can only be used in special cases where this side effect is negligible. Therefore, the rescaling by columns method minimizes perturbations in the simulation but lacks the generality of the local rescaling method.

5.2.1.5 Recovery time

The *recovery time* is the duration of time needed by the system to recover after a perturbation so that (unphysical) oscillations that are caused by the discrete nature of the method and the perturbations occurring after expansion and contractions are damped (within a given tolerance ϵ).

The simulation has been run with different viscosities ν ranging from $1/30$ to $1/3$ and the corresponding recovery times have been saved in a table. Figs. 5.13 and 5.14 show the recovery times after initialization (i.e., the time until the flow is fully developed), after expansion, and after contraction as a function of the diffusive time $t_d = H^2/\nu$, where H is the width of the channel. The lower the viscosity, the higher is the recovery time. The Figures 5.15 and 5.16 corresponding to a lower viscosity ($\nu = 1/30$) and showing the density ρ and the velocity component u_x as a function of time exhibit indeed a longer recovery time: it takes much longer for the perturbations to be damped out compared to the case $\nu = 1/3$ (compare with the corresponding Figures 5.7 and 5.8).

The recovery time depends on the condition for steady flow. The condition for steady flow is as follows and will be examined only in the center node of the channel (i.e., the node at $N_x/2$ on the centerline):

- In an array $U_x\text{Center}[t]$, the value of u_x at this center node is saved at every point in time.
- If the flow is unsteady (due to a change at the wall, i.e. expansion or contraction), wait at least some time (proportional to $\max(N_x, N_y)$) and store the maximum and minimum of u_x .
- If $(\max(u_x) - \min(u_x)) < \epsilon$, the flow is considered to be recovered. For ϵ , a value of 0.00001 has been chosen.

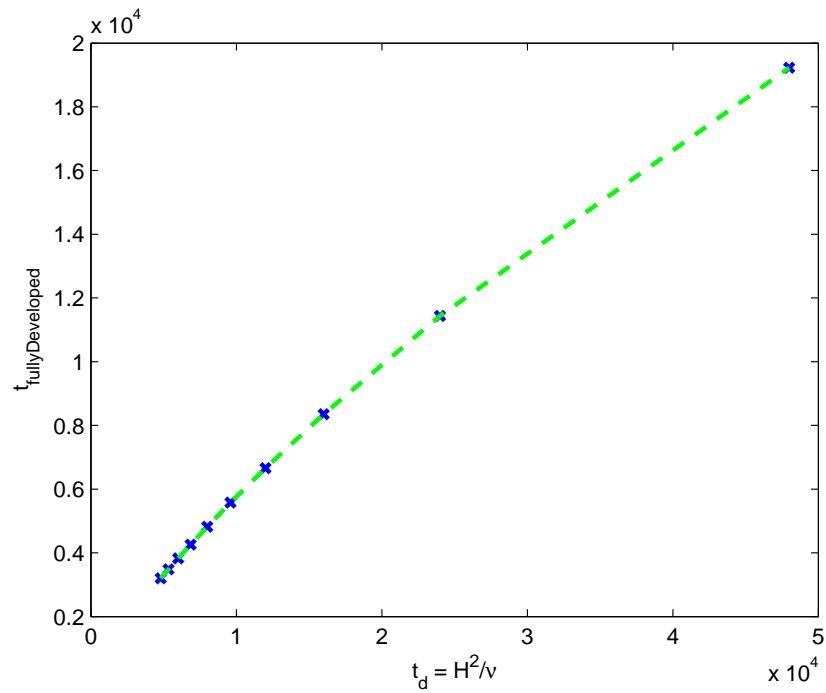


Figure 5.13: Time at which flow is fully developed as a function of the diffusive time t_d (ν varying)

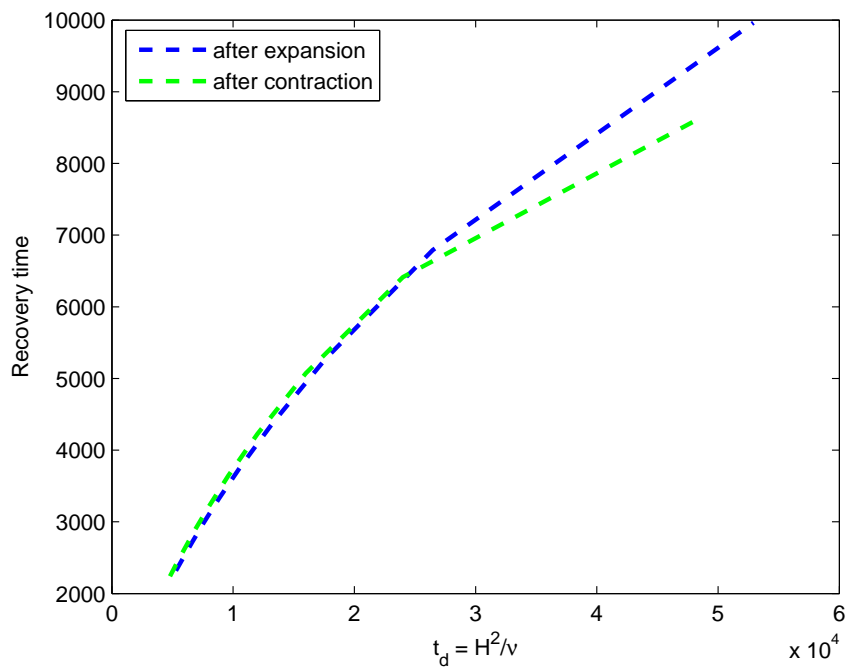


Figure 5.14: Recovery time after expansion (blue, $H = 42$) and contraction (green, $H = 40$) as a function of the diffusive time t_d (ν varying)

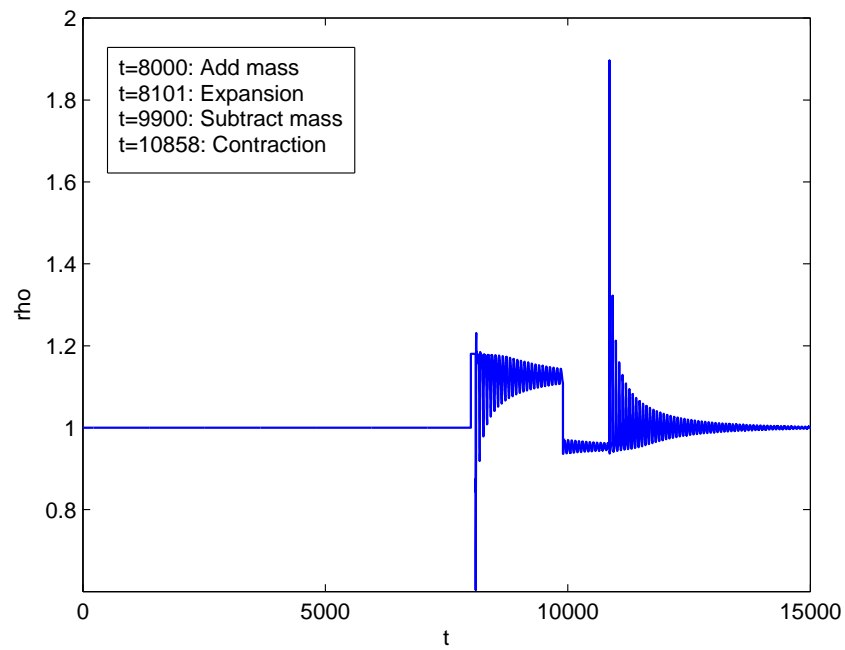


Figure 5.15: *Density at fluid node next to the wall as a function of time, lower viscosity ($\nu = 1/30$), compare with Fig. 5.7.*

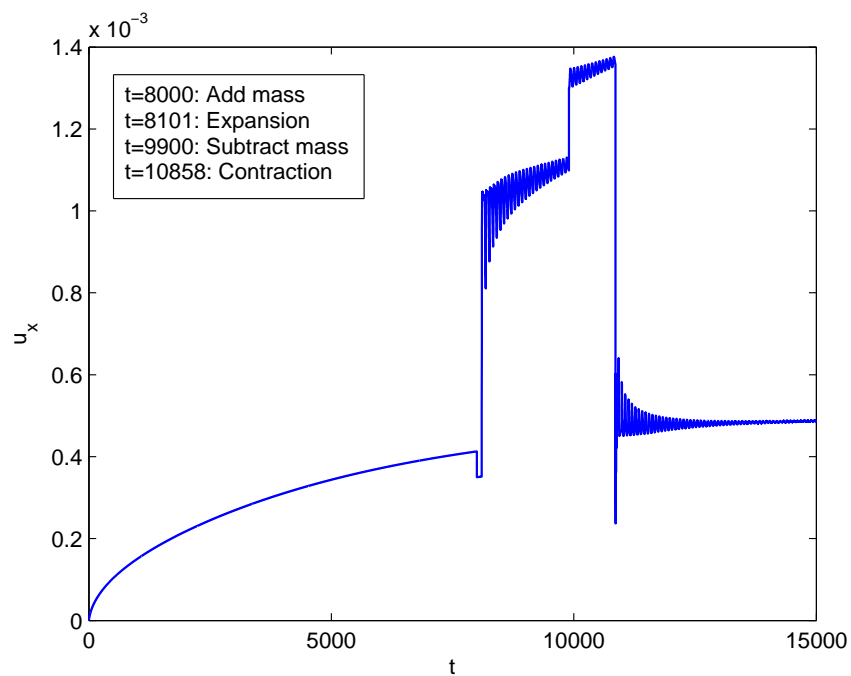


Figure 5.16: *Velocity component u_x at fluid node next to the wall as a function of time, lower viscosity ($\nu = 1/30$), compare with Fig. 5.8*

The steady flow condition is examined in one node of the fluid domain (center node). It is clear that oscillations (of ρ and u_x) occur mainly at the wall due to the redistribution and local rescaling of the populations. This perturbation of the flow field, which is also related to the discretization because values do not change continuously, takes a certain time (proportional to the width/length of the channel) to propagate through the channel (e.g., to the center node) and by consequence the flow field takes some time to recover. So, changes at the wall (expansion/contraction) will always lead to instabilities (the 'extent' of those instabilities depends on the chosen rescaling method). Thus, expansion and contraction can apply only when the flow is recovered. Otherwise the pressure that is compared with the pressure thresholds might have a physically incorrect value due to the perturbations that occur at the wall.

The computed recovery time is dependent on the tolerance ϵ when two values of u_x are compared. The smaller ϵ , the longer is the recovery time. Fig. 5.17 shows the recovery times as a function of the tolerance ϵ .

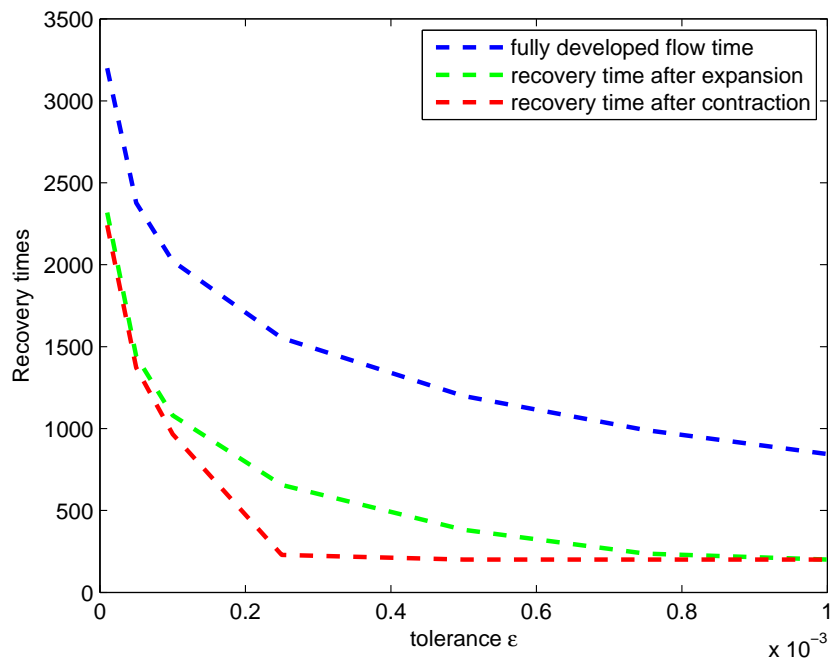


Figure 5.17: Recovery times as a function of the tolerance ϵ

5.2.2 Simulations with inlet/outlet pressure boundary conditions

Up to now, periodic boundary conditions have been used in the main direction of the flow (x -direction). With the aim of reproducing physiological cases, inlet/outlet boundary conditions will be used in the remainder of this chapter.

For next simulations, an initially straight channel is considered modeling the vessel which is again embedded in a computational domain of fixed dimensions $N_x \times N_y$. At inlet and outlet, pressure boundary conditions are imposed using the method of Zou/He [220] to determine the unknown LB populations pointing into the fluid domain. At the inlet, an oscillating pressure is prescribed. This is equivalent to imposing an oscillating density because density ρ and pressure p are linearly related through $p = c_s^2 \rho$, where c_s is the sound of speed. For simplicity, the pressure at the outlet is set constant and is chosen in a way that the pressure gradient between inlet and outlet is always positive. At the wall, the continuous bounce-back boundary condition, described in Chapter 4, are imposed, which represents a no-slip condition (i.e., the fluid velocity is zero at the wall). Expansion and contraction are allowed only after 1000 time steps when the flow is fully developed.

5.2.2.1 Simulation parameters

The following physical and numerical parameters have been used in the simulations: viscosity $\nu = 1/3$, initial density $\rho_0 = 1.0$, $\alpha = 0.007$, $p_0 = 1/3$, and $R_0 = 20$. All parameters and variables are normalized and hence dimensionless. A channel modeling the vessel of initial dimensions 200×40 nodes is embedded in the computational domain of fixed dimensions 200×100 nodes.

The densities at inlet (ρ_{in}) and outlet (ρ_{out}) are set respectively to

$$\rho_{in} = \rho_{mean} + A \sin\left(\frac{2\pi t}{T_{pulse}}\right) \quad (5.3)$$

$$\rho_{out} = 1.0 \quad (5.4)$$

Here, $\rho_{mean} = 1.025$ is the mean pressure, $A = 0.025$ the amplitude of the oscillations, t the time, and $T_{pulse} = 2500$ the period of the pulse. Thus, the density difference between inlet and outlet varies between zero and 0.05.

5.2.2.2 Results with halfway bounce-back on the link boundary condition

In first experiments, the continuous bounce-back boundary condition described in Section 4.1.3 has not been included. Instead, a halfway bounce-back on the link boundary condition has been used. This means that the wall is located halfway between fluid and solid nodes. Thus, the results presented hereafter correspond to simulations with the boundary conditions described in Section 3.3.2.

Before presenting the results with an oscillating pressure at the inlet in an elastic channel, a few results from simulations in a rigid straight channel are shown in order to prove that the system responds in a correct physical way. In a first step, a constant density gradient $\Delta\rho = \rho_{\text{in}} - \rho_{\text{out}}$ between inlet and outlet is assumed. The pressure gradient G is given by

$$G = \frac{\Delta p}{\Delta x} = \frac{c_s^2 \Delta\rho}{\Delta x}$$

and the corresponding centerline velocity by

$$U_{max} = \frac{G R^2}{2\nu}$$

with $R = \frac{H}{2}$ being the radius of the channel, compare with Eq. 5.2. The computed fully developed velocity profile has been compared with the analytical solution of Poiseuille. Fig. 5.18 shows a good agreement between the numerical result and the exact solution. Fig. 5.19a displays the parabolic fully developed velocity profiles along x in a straight rigid channel.

Figures 5.20a and 5.20b depict ρ and u_x as a function of time, respectively. The density at inlet and outlet of the rigid channel has been chosen as follows: $\rho_{\text{in}} = 1.05$ and $\rho_{\text{out}} = 1.0$, corresponding to a density difference $\Delta\rho$ of 0.05. As soon as the flow is fully developed ρ and u_x are equal to the values expected at the center node of the channel, i.e., 1.025 for ρ and 0.05 for u_x .

The same simulations have been conducted in a rigid channel with curved walls. The results are similar to the ones presented above. The velocity profiles at different positions x in the rigid channel with curved walls displayed in Fig. 5.19b have a parabolic shape.

The remaining results in this subsection are gained from simulations with an elastic channel. Halfway bounce-back condition at the wall and an oscillating density at the

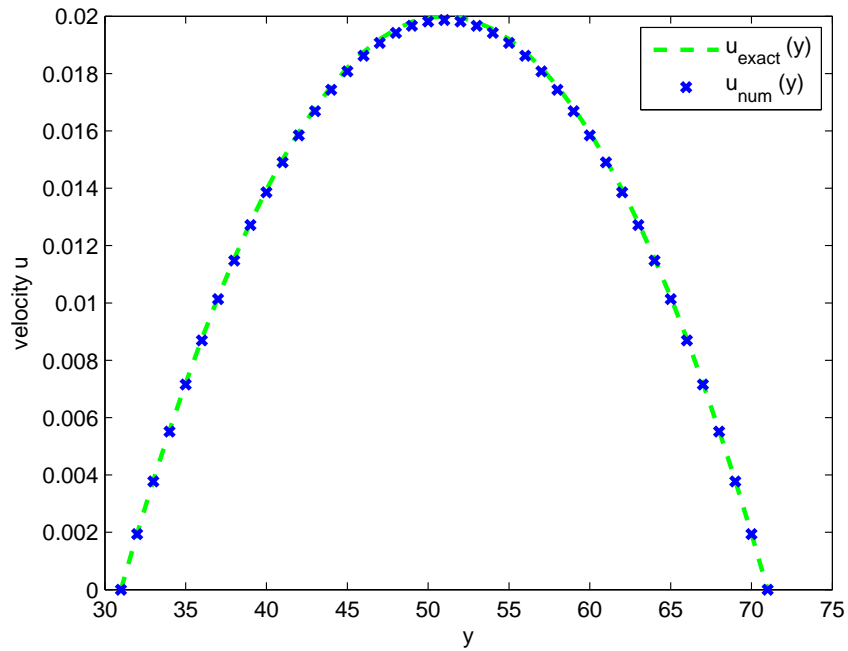


Figure 5.18: Comparison between computed velocity profile (blue) and analytical solution of Poiseuille (green) with density difference $\Delta\rho = 0.02$ between inlet and outlet (inlet/outlet BC)

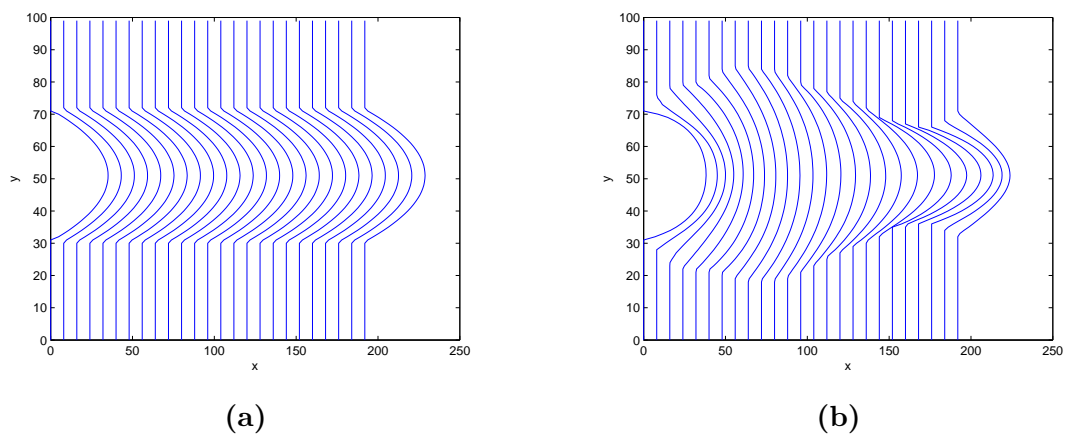


Figure 5.19: Velocity profiles of fully developed flow along x in a rigid straight channel (a) and a rigid channel with curved walls (b)

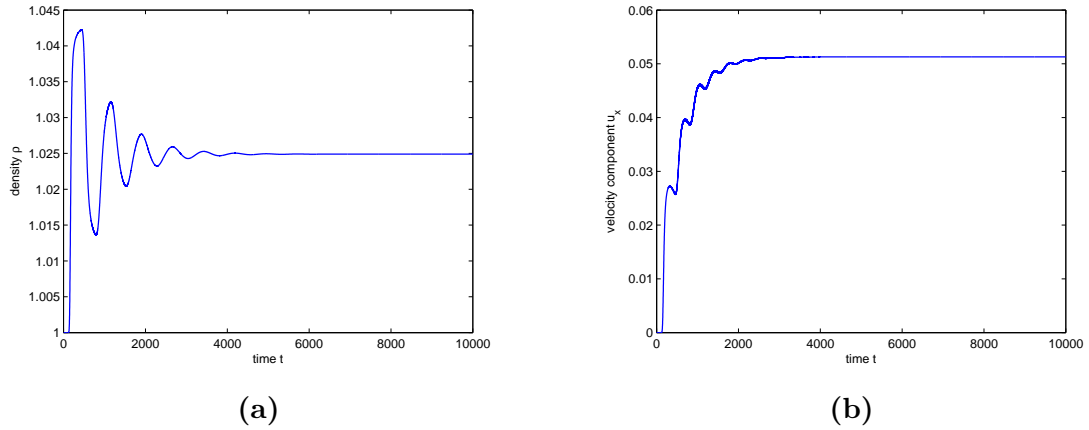


Figure 5.20: Time history of the density ρ (a) and the velocity component u_x (b) at the center node of the channel

inlet (see Eq. 5.3) are imposed. Since the distance q from the last fluid node to the wall is constant ($q = 1/2$) in the case of the BBL boundary condition, another condition for changing the type of a node has to be chosen. One possibility is to simply compare the current pressure to the pressure threshold and change the state of a node when the pressure exceeds or falls below the corresponding pressure threshold. As soon as the pressure at a fluid node exceeds the pressure threshold, the neighboring solid node becomes fluid and the wall changes by one lattice unit within one single time step. Analogously, as soon as the pressure of a fluid node falls below the pressure threshold, the considered node becomes solid and the wall is displaced by one lattice unit. Thus, the displacement of the wall is not continuous. The radius can only change by one full lattice unit.

Fig. 5.21 shows the density as a function of time at a fluid node near the wall. The time history of the velocity component u_x at a node near the wall is depicted in Fig. 5.22. It can be observed that density and velocity oscillate in a correct way as a response to the oscillating pressure at the inlet, but are superposed by smaller oscillations and also display peaks that seem unphysical. These oscillations and peaks are caused by the discrete nature of the method due to the not continuous displacement of the wall, which perturbs the system. The condition for changing the type of a node has been adapted again. In order to not use incorrect values of the pressure (that are just the consequence of the perturbation at the wall due to the node type change) for the comparison, the pressure over a certain number of time steps is averaged, and this average value is compared with the pressure threshold. This procedure avoids that the wall is displaced due to unphysical values of the pressure. However, the oscillations and peaks remain.

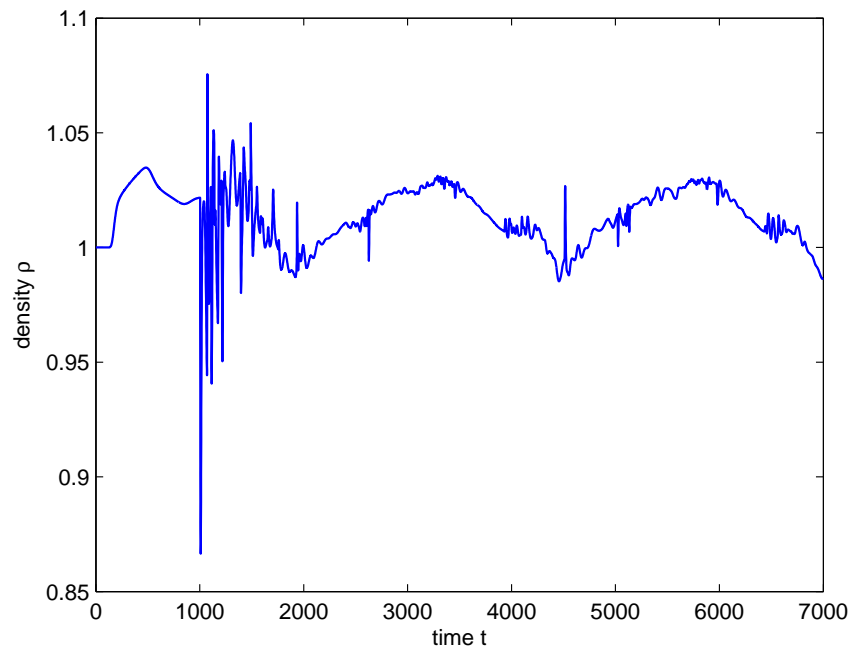


Figure 5.21: *Density ρ as a function of time at a node near the wall (bounce-back on the link, see Section 3.3.2)*

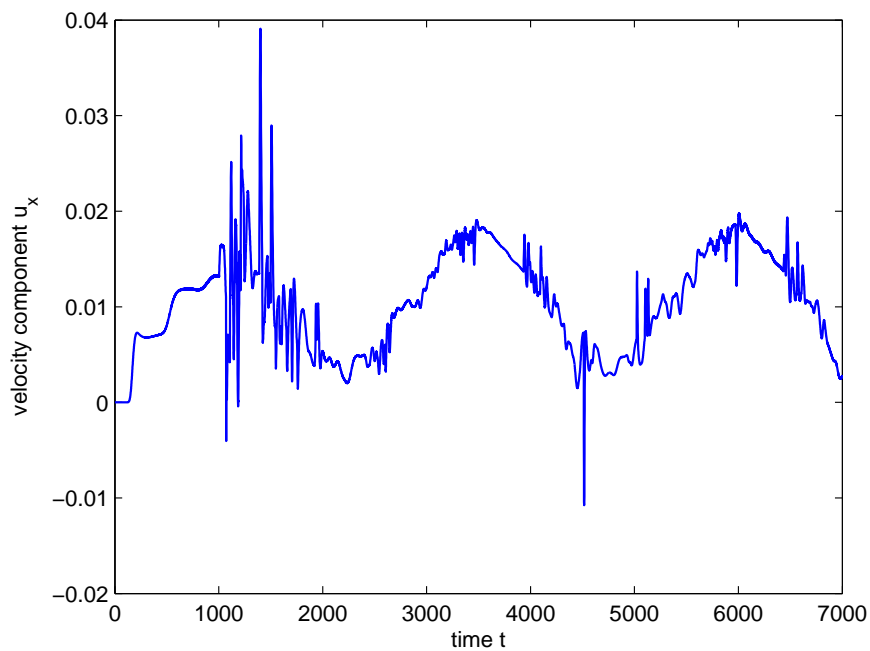


Figure 5.22: *Velocity component u_x as a function of time at a node near the wall (bounce-back on the link, see Section 3.3.2)*

Fig. 5.23 displays the moving average over 250 time steps (one tenth of the pulse period T_{pulse}) of u_x at different nodes of the channel. It can be observed that taking the moving average filters out the superposed oscillations and peaks appearing in the time history of the velocity. This confirms the assumption that the system reacts in a correct way and that the perturbations are only caused by the instantaneous displacement of the wall by one lattice unit.

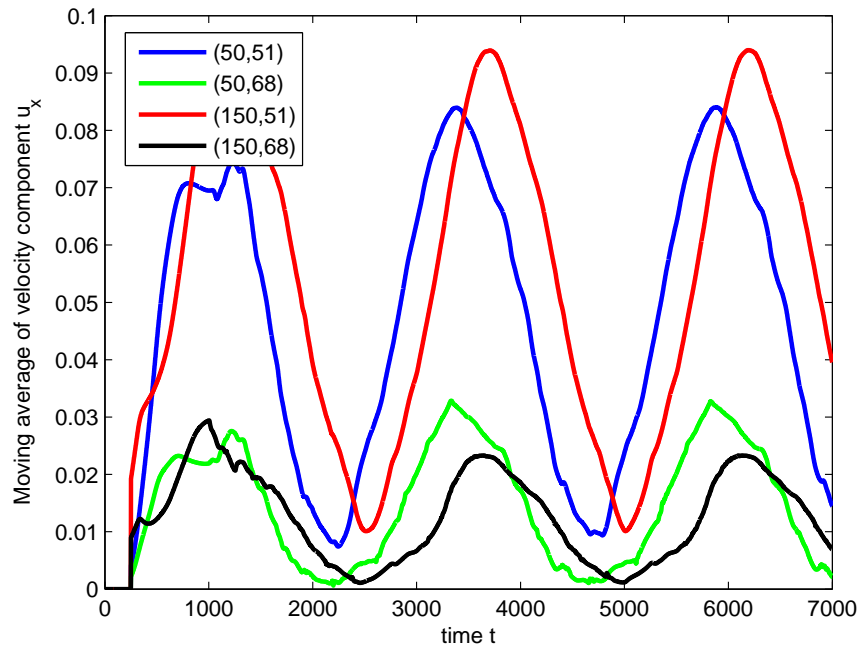


Figure 5.23: *Moving average over 250 time steps of the velocity component u_x at different lattice nodes (blue and red for a node with central y -coordinate, green and black for a node with y -coordinate near the upper wall)*

5.2.2.3 Results with continuous bounce-back boundary condition

In order to minimize the unphysical oscillations and spikes appearing in the time histories of the density and the velocity, simulations including the continuous bounce-back boundary conditions have been carried out, as described in Section 3.3.3, with the simulation parameters cited in Section 5.2.2.1.

Density, velocity, total mass

Figures 5.24 and 5.25 display ρ and u_x as a function of time at a fluid node near the wall, respectively. In each case, the peak values are the same for the second and

third peak. The first peak should not be taken into consideration because expansion and contraction are allowed only after the first 1000 time steps ($t > 1000$) when fully developed flow is guaranteed.

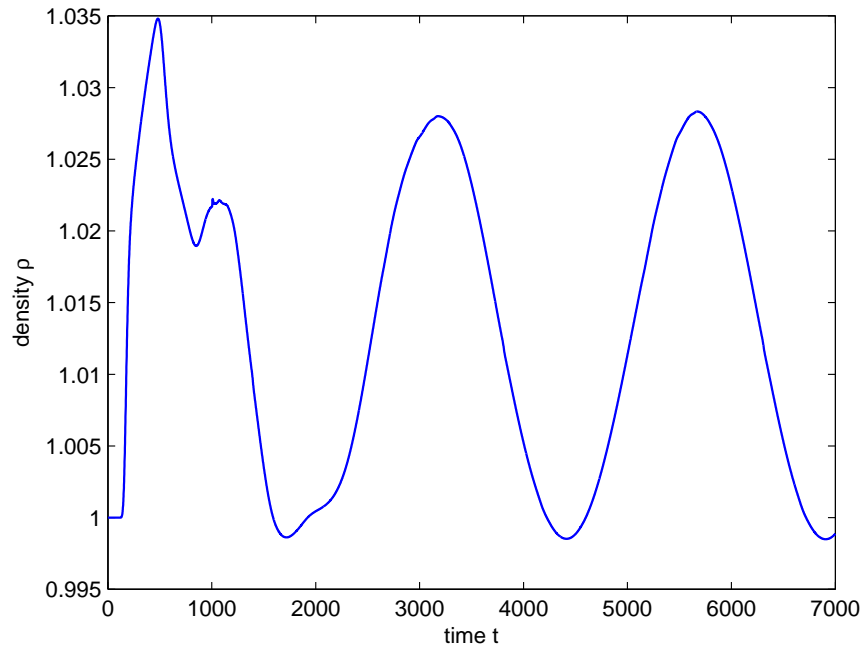


Figure 5.24: *Density ρ as a function of time at a node near the wall (continuous bounce-back)*

The time histories of ρ and u_x show smooth behavior without superposed oscillations or spikes, yet maintaining the same frequency and amplitude as in Figures 5.21 and 5.22 (the same parameters have been used for the two simulations). This is due to the continuous displacement of the wall and to the fact that the LB populations are corrected over several time steps before a node type change occurs and new fluid nodes are initialized based on the LB populations of the neighboring nodes.

The total mass as a function of time is displayed in Fig. 5.26. It exhibits an oscillating behavior as the density (pressure) at the inlet.

The surface plot of the velocity component u_y at time $t = 6000$ in Fig. 5.27 shows that u_y is of the order of 10^{-3} for the given parameters. Due to the wall deformability, u_y is not exactly zero but very small. The velocity field at time $t = 6000$ in a part of a channel depicted in Fig. 5.28 underlines this fact. It can be seen that the main direction of the flow is in x -direction.

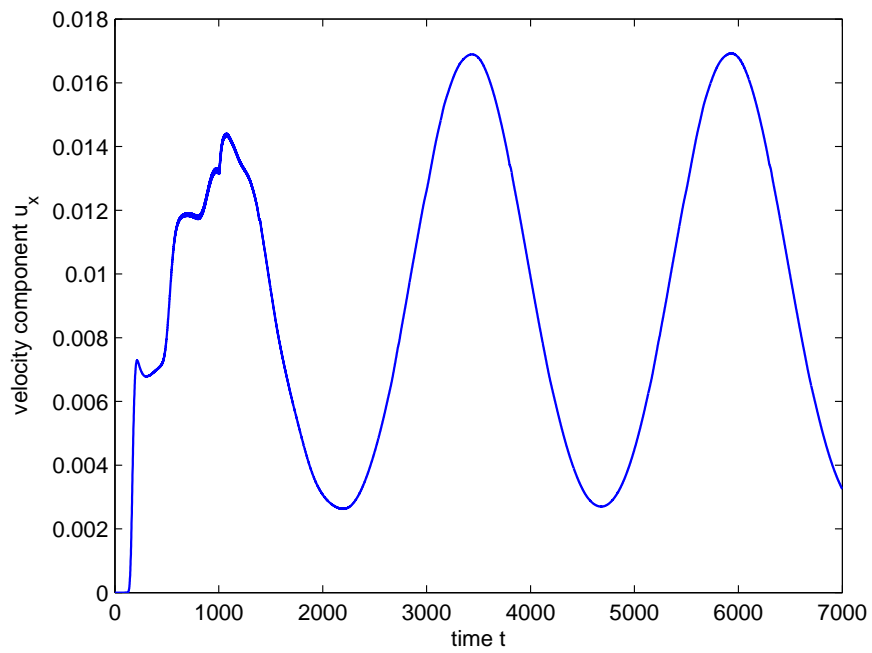


Figure 5.25: Velocity component u_x as a function of time at a node near the wall (continuous bounce-back)

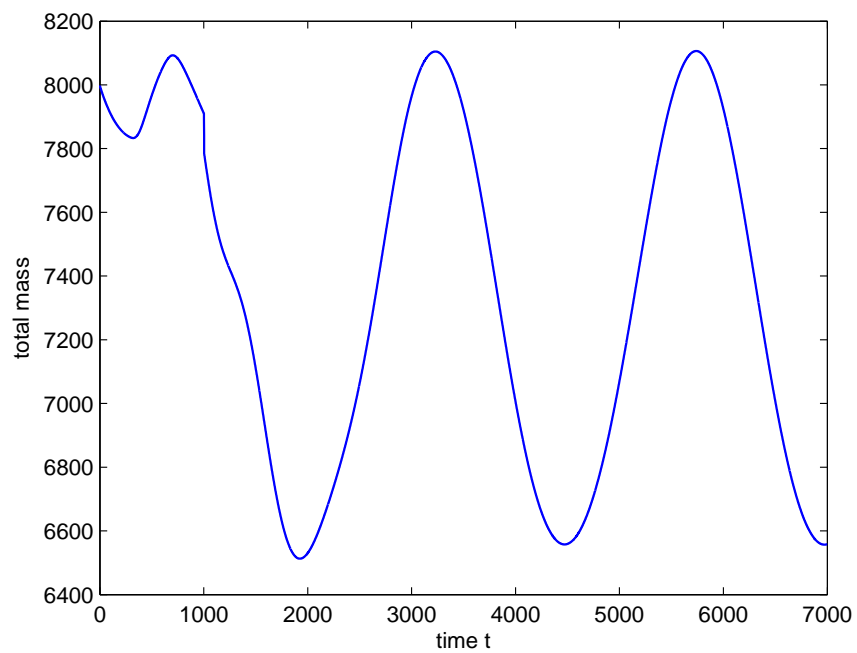


Figure 5.26: Total mass as a function of time

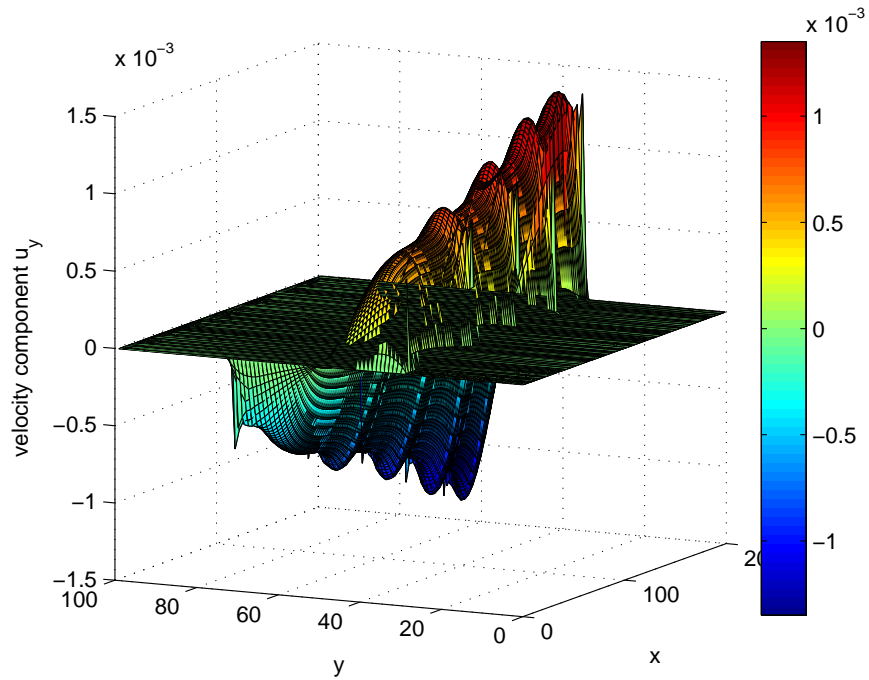
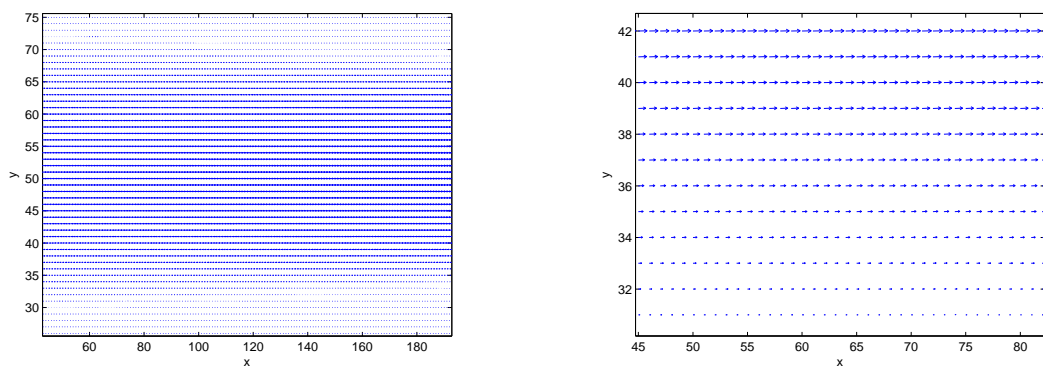


Figure 5.27: Surface plot of the velocity component u_y at time $t = 6000$



(a) small zoom

(b) big zoom near the lower boundary

Figure 5.28: Velocity field at time $t = 6000$

Fig. 5.29 displays the profiles for the velocity component u_x at several positions x for three points in time. The light blue lines indicate the position of the virtual wall where the no-slip condition is valid.

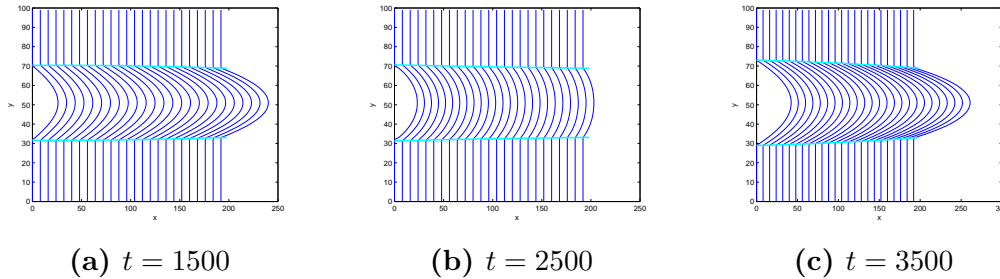


Figure 5.29: Profiles of the velocity component u_x along the channel at three instants in the case of oscillating inlet pressure. The scale of these figures do not allow a precise resolution, but the channel in case (b) is slightly more expanded than in case (a), and the channel in case (c) is more expanded than in case (a) and (b). The wall displacement of just one or two lattice units is not clearly visible in the figures.

Fig. 5.30 details the velocity field in a compliant channel computed at several instants. As time is progressing, the channel expands and contracts by a few lattice units.

Radius

The virtual radius $R(x)$ at a position x has been introduced in Chapter 4, see Eq. 4.1.

Fig. 5.31 displays the virtual radius at every position x for different points in time. At the outlet ($x = 199$), the channel is constrained due to the boundary condition which imposes a constant pressure, see Eqs 4.2 and 4.4. Since the pressure at the outlet does not change (see Eq. 5.4), the parameter q does not change either and, as a consequence, the radius at the outlet is constant. In order to neglect the effect of the constriction of the outlet on the flow field, the channel has to be long enough. A physiologically more correct boundary condition that does not bound the outlet section will be presented in Section 5.2.4.

The parameter q

Fig. 5.32 shows the time evolution of the parameter q at a fixed node at the lower wall. The discontinuities are due to the change of node type when q is reset to a value between zero and one (see Section 4.3).

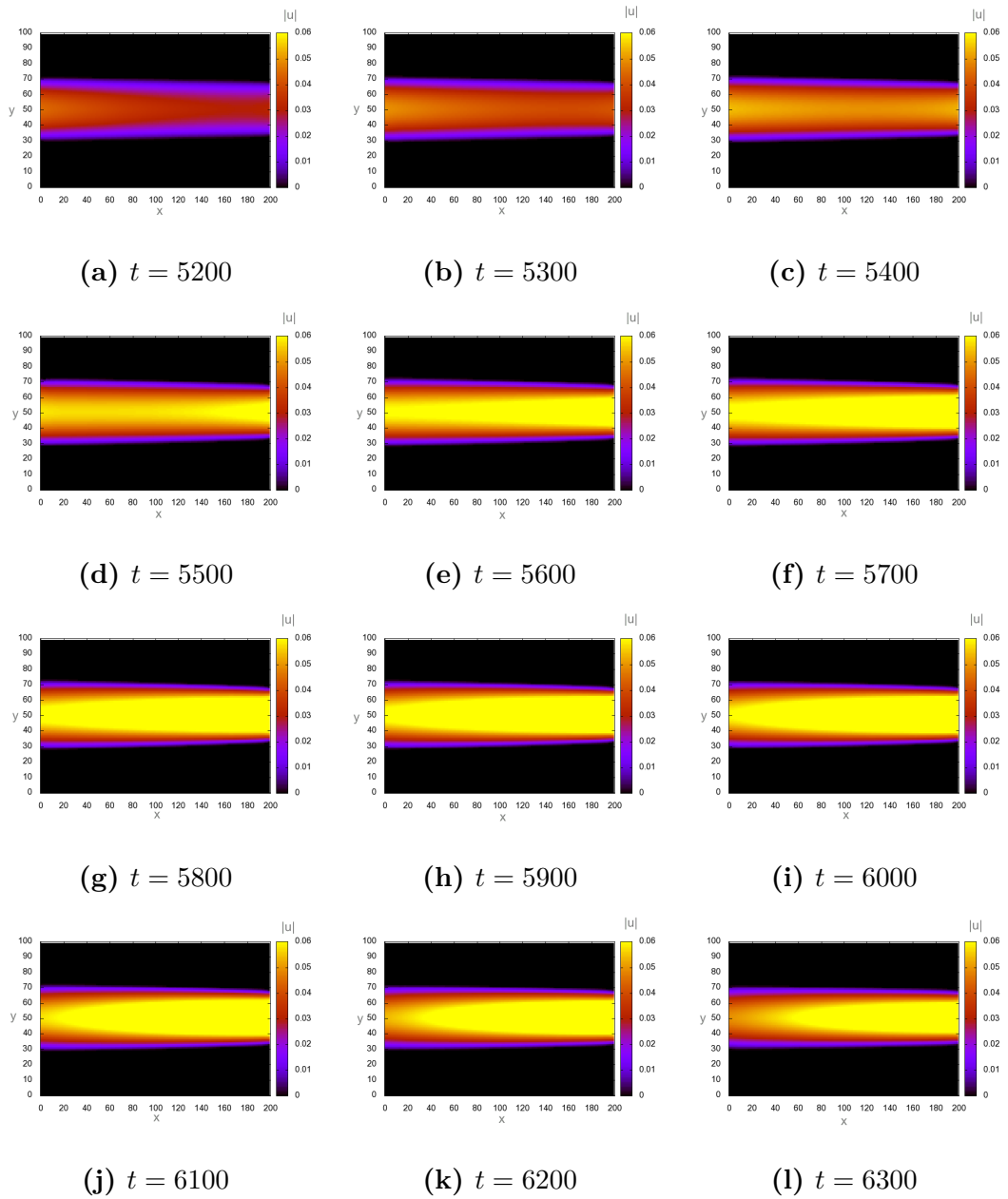


Figure 5.30: Velocity field in a compliant channel for different points in time. The channel expands and contracts (by a few lattice units) as time is progressing.

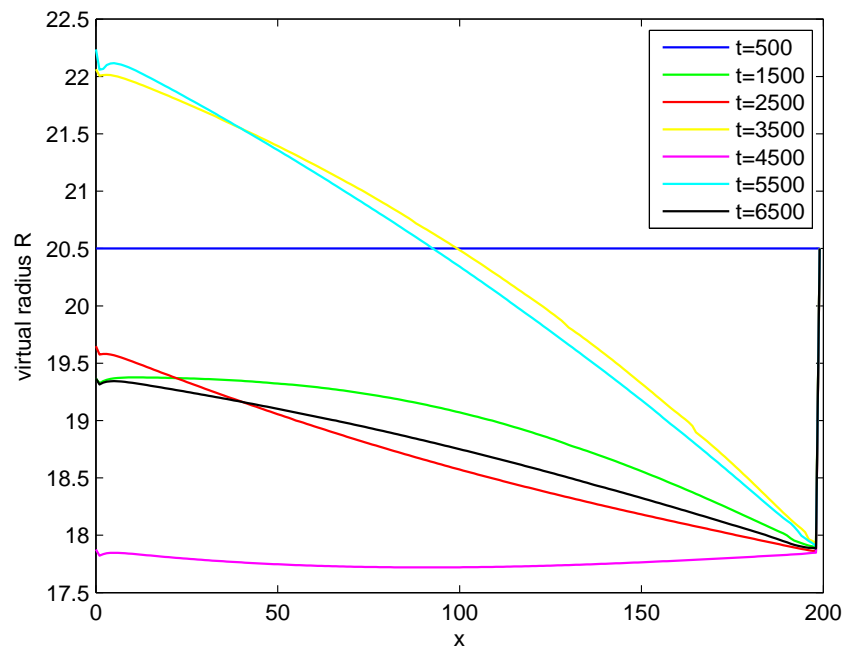


Figure 5.31: *Virtual radius R at every position x for different points in time*

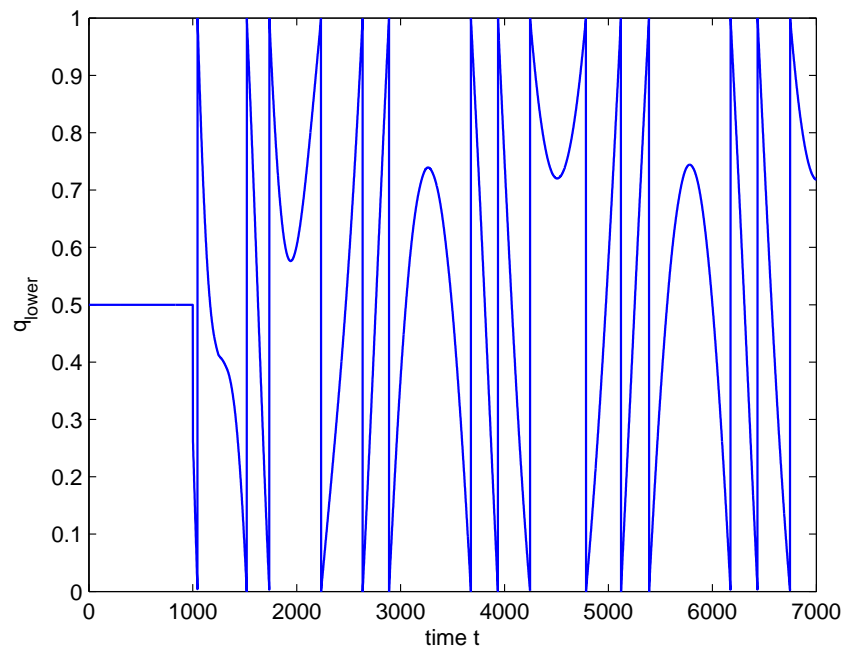


Figure 5.32: *Parameter q of continuous bounce-back condition for a fixed node at the lower wall*

In order to verify that the continuous bounce-back condition does not cause systematic errors, the frequency of the values taken by the parameter q has been computed. The histogram for q at the lower boundary over one pulse period (2500 time steps) is depicted in Fig. 5.33: for all x in Fig. 5.33a and for all x except inlet and outlet in Fig. 5.33b. The histogram in Fig. 5.33a exhibits one prominent peak (a frequency of 10000). This peak is due to the boundary condition at the outlet which bounds the outlet section because of the prescribed constant pressure (and as a consequence constant q). Besides this peak, the histograms in Fig. 5.33 do not have prominent peaks; the smaller peaks around zero and one are due to the fact that q is reset to zero or one after creation or destruction of a fluid node when the excess Δq is greater than one, see 4.3. The shape of the histograms depends on the chosen oscillating pressure, i.e., on the pulse period and the amplitude.

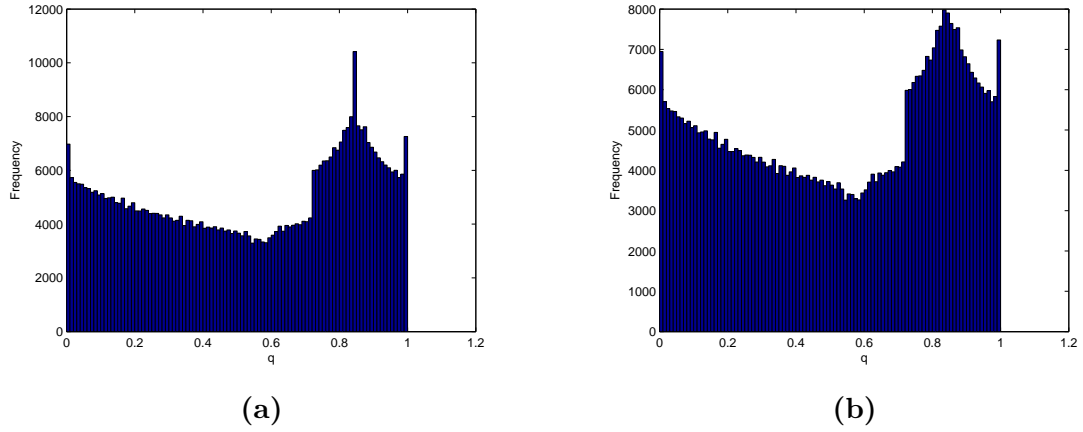


Figure 5.33: *Histograms for the parameter q of the continuous bounce-back condition at the lower boundary over one pulse period: (a) all x including inlet and outlet; (b) all x except inlet and outlet. The prominent peak in case (a) is due to the boundary condition at the outlet which bounds the outlet section because of the prescribed constant pressure (and as a consequence constant q). The smaller peaks around zero and one are due to the fact that q is reset to zero or one after creation or destruction of a fluid node when the excess Δq is greater than one, see Section 4.3*

5.2.3 Sensitivity analysis with inlet/outlet pressure boundary conditions

A sensitivity analysis by changing the compliance parameter α , the amplitude T , or the pulse period T_{pulse} has been conducted in a computational domain of dimensions

$N_x \times N_y = 400 \times 100$ or $N_x \times N_y = 200 \times 100$.

5.2.3.1 Influence of the compliance parameter α

In order to study the behavior of the wall having different elastic properties, simulations with different values of α have been run. The amplitude and the pulse period of the oscillating density have been kept constant: $A = 0.05$ and $T_{\text{pulse}} = 2500$. Fig. 5.34 depicts the maximum radius as a function of the compliance parameter α . As expected, a lower value of α leads to a larger wall deformation. Fig. 5.35 displaying the virtual radius (see Eq. 4.1) at every x from simulations with different values of α shows this effect as well.

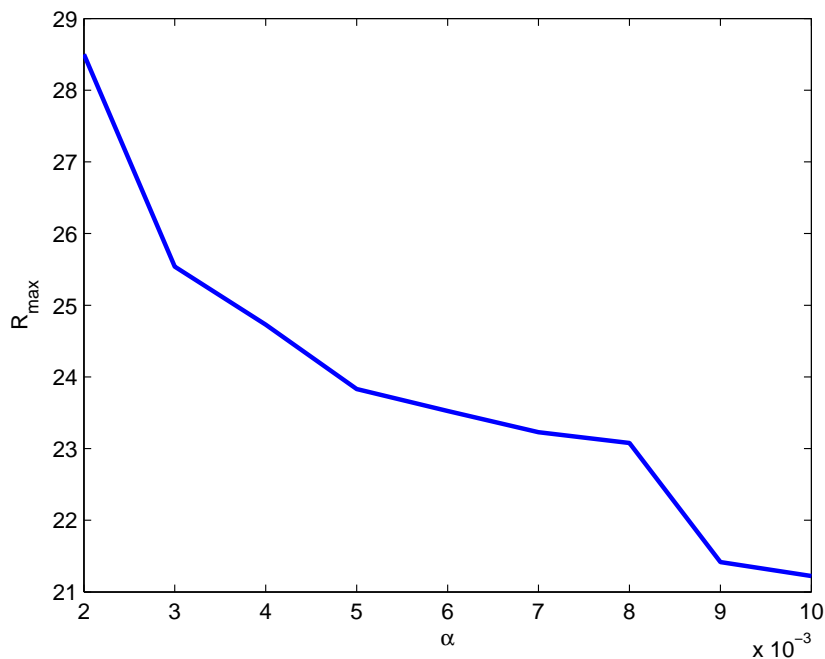


Figure 5.34: Maximum radius as a function of the compliance parameter α

Concerning the simulations of arterial blood flow, it should be pointed out that the diameter of a large vessel does not change by more than 10% [165]. This should be taken into account when choosing α . Note that the wall deformation is very sensitive with α , compare Figures 5.35a ($\alpha = 0.003$) and 5.35b ($\alpha = 0.007$).

Fig. 5.36 depicts the histograms of the parameter q gained from simulations with two different values of α . The histograms have a smooth shape (except for the peak caused

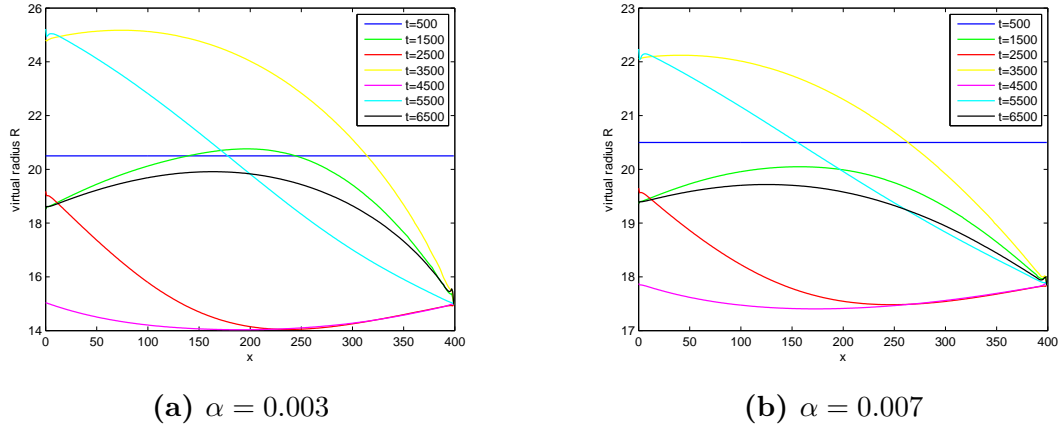


Figure 5.35: *Virtual radius R at every position x for different points in time, gained from simulations with different α . Expansion and contraction are allowed only after 1000 time steps when the flow is fully developed. Hence, at $t = 500$, the channel keeps its initial state (straight).*

by the outlet boundary condition) which confirms again that there are no systematic errors in the continuous bounce-back method.

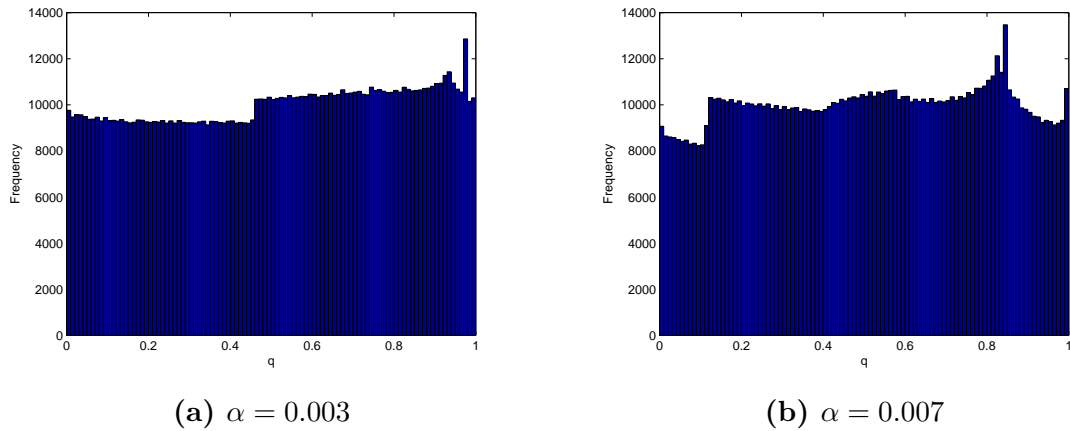


Figure 5.36: *Histograms for the parameter q of the continuous bounce-back condition at the lower boundary over one pulse period, gained from simulations with different α . In each case, the prominent peak is due to the boundary condition at the outlet which bounds the outlet section because of the prescribed constant pressure, see Eq. 5.4 (and as a consequence constant q).*

The compliance parameter α should have an effect on the wave propagation speed. The stiffer the channel (i.e., the higher α), the higher is the wave speed, see Eq. 2.36 or Eq. 2.50. The wave speed can be identified graphically from the contour plots of the channel radius by determining the slope of the isolines in the contour plot.

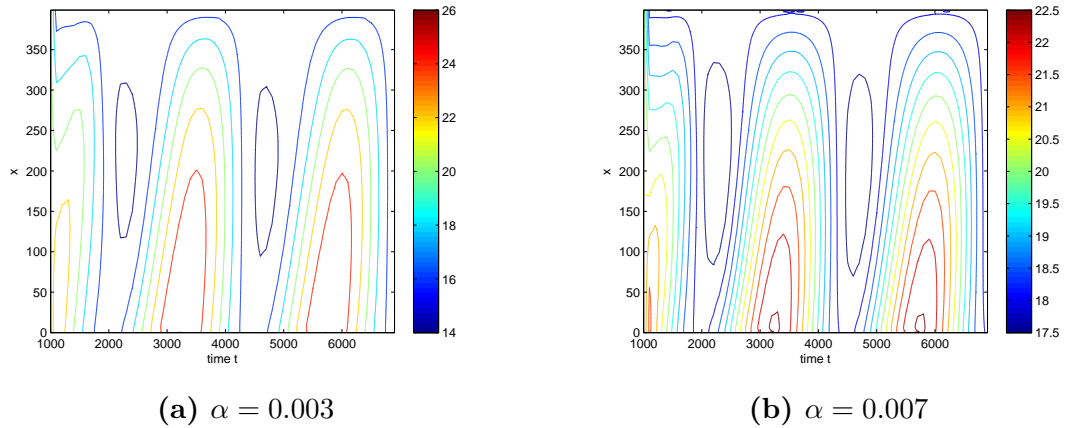


Figure 5.37: Contour plot of the virtual radius R , gained from simulations with different α . Different colors correspond to different values of R . Note that the scaling is not the same in case (a) and (b).

Fig. 5.37 displays the contour plot of the radius R in the t - x -plane gained from simulations with two different values of α . It can be observed that the slope of the curve does not change much when comparing the two plots corresponding to $\alpha = 0.003$ and $\alpha = 0.007$. A possible reason for this is that the modeling of the wall elasticity does not include a real fluid-structure interaction because no feedback from the wall to the fluid is given, see Chapter 4. In fact, in both cases, the wave speed is of the order of magnitude of c_s^2 , the square of the speed of sound in the lattice Boltzmann algorithm. If one is interested in studying the wave propagation, an appropriate model should be further developed. One idea is to use a spring model that links contiguous wall nodes near the wall. Further work in such a direction is planned.

The circumstance that there is no visible difference in the wave speed when changing α could also be related to the outlet boundary condition because of the prescribed constant pressure. An attempt to circumvent this problem using the Windkessel concept will be presented in Section 5.2.4.

Furthermore, it can be seen in Fig. 5.37 that the oscillation of the wall is damped downstream: the radius of the channel changes more in the section close to the inlet than in the section close to the outlet. This effect can be due to the outlet boundary condition which keeps the radius at the outlet fixed, the length of the channel, and the chosen viscosity.

5.2.3.2 Influence of the amplitude A

Simulations have been conducted changing the amplitude A and keeping constant the compliance parameter ($\alpha = 0.007$) and the pulse period ($T_{\text{pulse}} = 2500$). Fig. 5.38 displays the virtual radius at every x from simulations with different amplitude A . As expected, a higher value of the amplitude leads to a larger deformation of the channel.

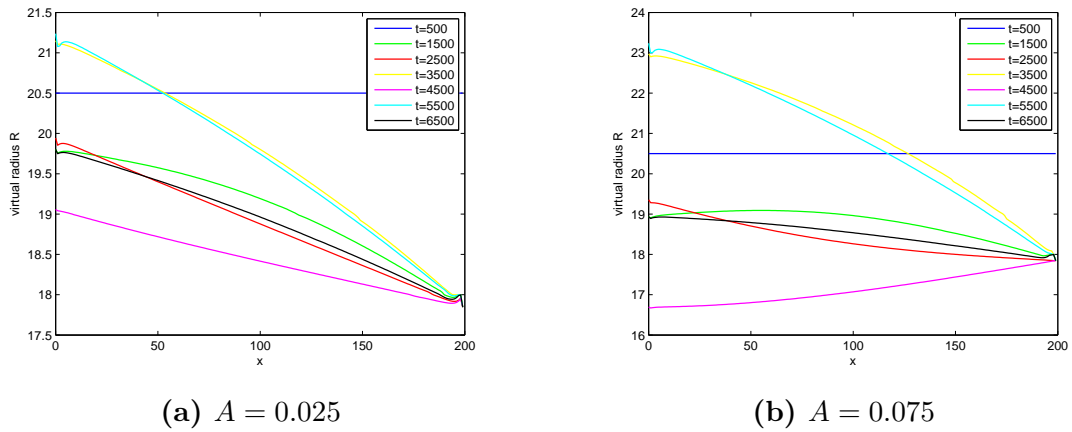


Figure 5.38: *Virtual radius R at every position x for different points in time, gained from simulations with different amplitude A*

The corresponding histograms of the parameter q are depicted in Fig. 5.39. It can be observed that the amplitude has an effect on the shape of the histogram. Depending on the amplitude, the values are accumulated in a certain interval. However, the shape remains smooth. The prominent peaks are again due to outlet boundary condition and can be neglected.

5.2.3.3 Influence of the pulse period T_{pulse}

Simulations have been carried out changing the pulse period T_{pulse} and keeping constant $\alpha = 0.007$ and the amplitude $A = 0.05$. The virtual radius at every position x gained from simulations with different pulse period is displayed in Fig. 5.40. Since the points in time at which the radius is saved are a multiple of the pulse period, the curves in Fig. 5.40a almost overlap.

Fig. 5.41 depicts the histograms of the parameter q gained from simulations with two different values of T_{pulse} . It can be observed that the pulse period has an effect on the shape of histogram (nevertheless smooth) and the accumulations of certain values,

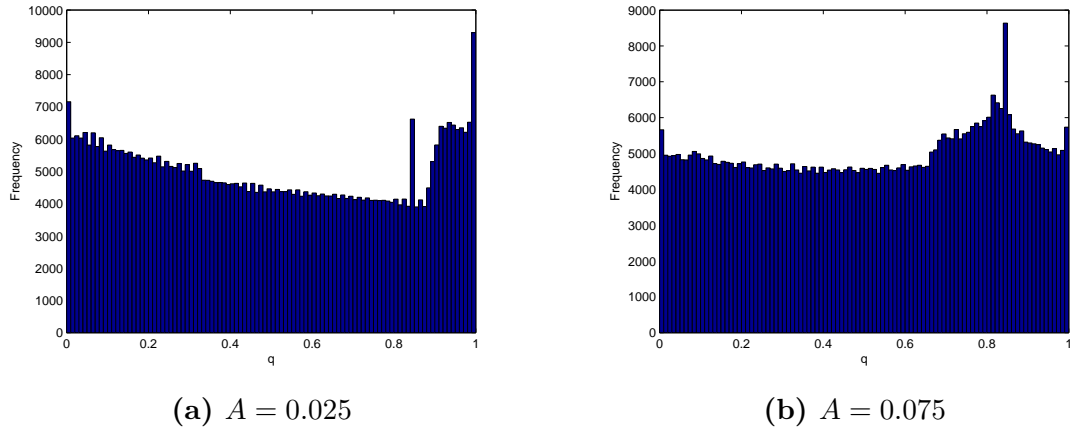


Figure 5.39: Histograms for the parameter q of the continuous bounce-back condition at the lower boundary over one pulse period, gained from simulations with different amplitude A . In each case, the prominent peak (around 0.85) is due to the boundary condition at the outlet which bounds the outlet section because of the prescribed constant pressure (and as a consequence constant q). The peaks around zero and one are due to the fact that q is reset to zero or one after creation or destruction of a fluid node when the excess Δq is greater than one, see Section 4.3

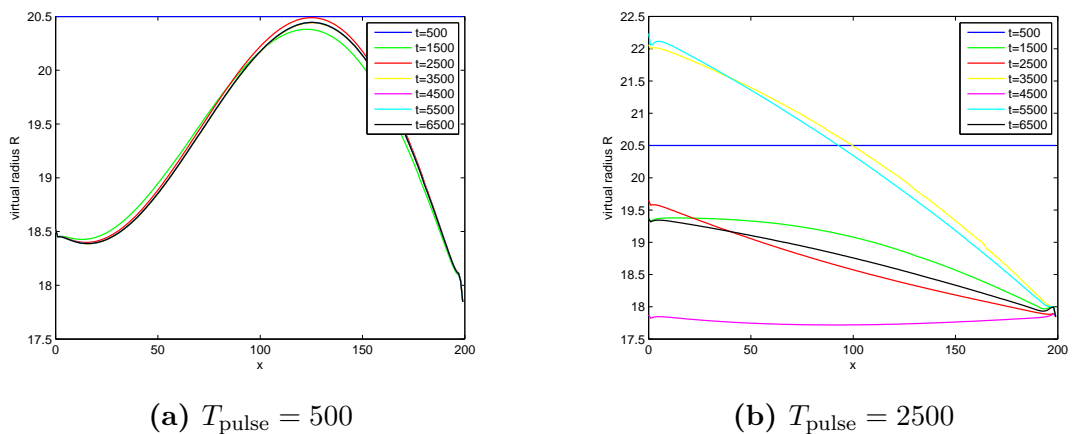


Figure 5.40: Virtual radius R at every position x for different points in time, gained from simulations with different pulse period T_{pulse}

as mentioned before. In fact, it is, among other, the interplay of pulse period and amplitude that has an effect on the shape of the histogram.

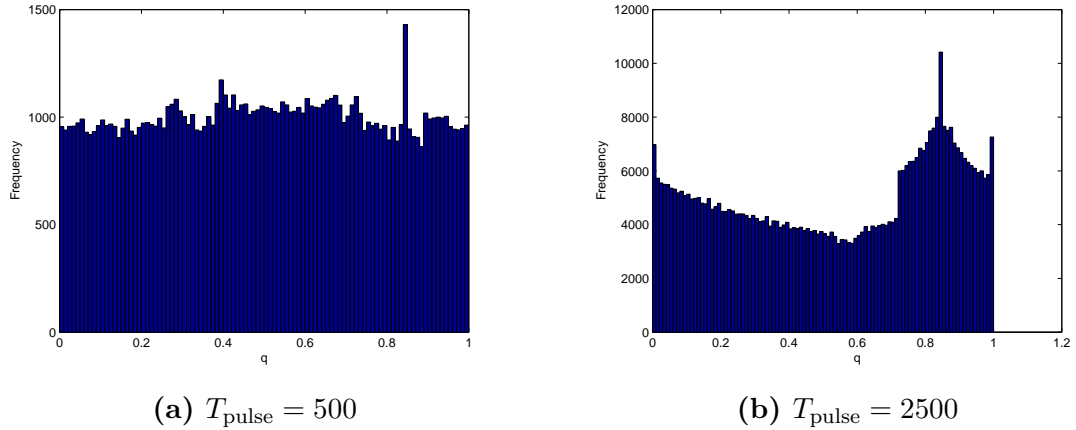


Figure 5.41: *Histograms for the parameter q of the continuous bounce-back condition at the lower boundary over one pulse period, gained from simulations with different T_{pulse} . In each case, the prominent peak (around 0.85) is due to the boundary condition at the outlet which bounds the outlet section because of the prescribed constant pressure (and as a consequence constant q).*

5.2.4 Coupling between Windkessel model and lattice Boltzmann method

To circumvent the problem caused by the outflow boundary condition prescribing a constant pressure, see Section 5.2.3, another boundary condition is suggested. The lattice Boltzmann model is coupled with a Windkessel model at the outlet boundary. By this, the radius of the outlet section can change because the pressure is not constant anymore and physiological cases can be reproduced. To the knowledge of the author, the coupling of lattice Boltzmann models with a Windkessel model has not been investigated up to now.

In the following, an overview of the Windkessel (WK) concept is first given. The LBM/WK coupling is then described and preliminary results from numerical experiments are presented.

5.2.4.1 The Windkessel model

The Windkessel model is an electric analog model commonly used in the overall representation of the cardiovascular system. It considers the arterial system as a chamber able to store blood and is based on the property that larger arteries first save some amount of the blood coming from the heart in order to release it afterwards in a continuous way. By this principle, the pulsatile flow which originates due to the periodic pumping of the heart is transformed to a continuous flow downstream the vessels. The name of the described concept comes from the German word ‘Windkessel’ which is an air chamber in fire engines. By analogy with the early fire-engine pumps, the air chamber represents the large arteries while the single outlet tube represents the small vessels [166]. S. Hales was the first who qualitatively described a lumped model of the arterial system, in 1733 [70].

At the end of the 19th century, the German physiologist O. Frank tried to compute the stroke volume (blood volume pumped from the heart in one heart beat) from the measured pressure in the aorta by using the two-element Windkessel model [57]. His calculations led to a nonlinear differential equation relating pressure and flow. When the pressure at the distal side of the system (venous pressure) is assumed to be zero, the differential equation takes the form

$$Q_{\text{in}} = C \frac{dp}{dt} + \frac{p}{R}. \quad (5.5)$$

Here, Q_{in} is the outflow from the left ventricle and p is the arterial pressure. In this model, the whole arterial tree is modeled as an electric chamber where R represents the total peripheral resistance and C can be interpreted as the total arterial compliance, i.e., C describes the ability of the whole arterial tree to store blood [166], see Fig. 5.42. It is defined as the ratio of change in blood volume V to corresponding change of blood pressure p and is assumed to be constant.

$$C = \frac{dV}{dp} \quad (5.6)$$

In general, Eq. 5.5 does not admit an explicit solution in p because Q_{in} is time-dependent. However, during diastole $Q_{\text{in}} = 0$ because the aortic valves are closed. In this case, the homogeneous solution p_h of Eq. 5.5 is given by

$$p_h(t) = B e^{-\frac{t}{RC}} \quad (5.7)$$

where B is an arbitrary constant. Eq. 5.7 represents an exponential decay with time constant RC .

The importance of the Windkessel concept has been detected as Fourier transformations have been applied to the nonlinear equation derived by O. Frank. By this, a description of the Windkessel in the frequency domain was obtained, which allowed an equivalent representation as electric circuit [166]. If current represents the rate of flow and voltage represents the pressure, the Windkessel has the same functional form as a capacitor (representing the total arterial compliance) in parallel with a resistor (representing the total peripheral resistance) [166]. This is called a two-element Windkessel because it includes two electric components, a capacitor and a resistor. The analog electric circuit is depicted in Fig. 5.42. It has the same differential equation as the Windkessel model described by Eq. 5.5. Other Windkessel models exist (three- and four-element Windkessel), see for example [4]. Similarly, other lumped-parameter models for the study of the systemic arterial tree have been designed and investigated in varying and increasing degrees of detail. A mathematical formulation of these models can be found in [152] and in the references therein.

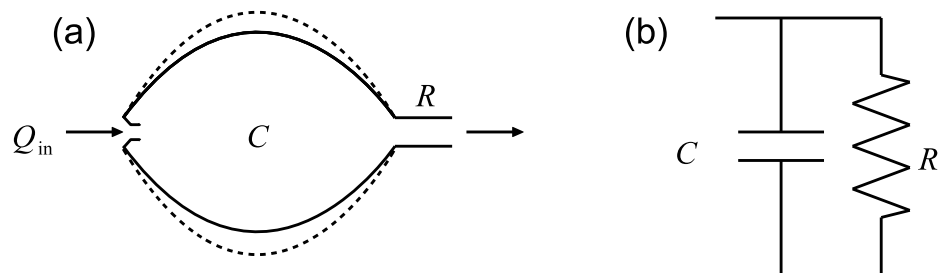


Figure 5.42: *The Windkessel model (a) and the equivalent representation as electric circuit (b). Q_{in} is the flow into the Windkessel, C denotes the compliance/capacitance and R represents the resistance.*

By adding an inductance in series with the resistance in the electric analog in Fig. 5.42, fluid inertia can be included in the model, see [44]. Table 5.2 lists the variables of the hydrodynamic system and the corresponding variables/components of the electric analog.

5.2.4.2 Coupling LBM/WK

In distributed models of blood flow through the cardiovascular system, the peripheral circulation is often considered as a distal boundary condition for the arterial system.

| Flow system | Electric analog |
|---------------|-----------------|
| Volume flow | Current |
| Pressure | Voltage |
| Compliance | Capacitor |
| Resistance | Resistor |
| Fluid inertia | Inductance |

Table 5.2: *Correspondance of hydrodynamic and electric variables*

As a representation for a terminating impedance at the end of the arterial system, the Windkessel model can be used for the description of the arterial termination and, properly validated, can avoid spurious reflections at the outlet.

An attempt has been made to couple the Windkessel model with the lattice Boltzmann model used for the computations of the fluid dynamics. The basic idea of the coupling is sketched hereafter. It should be understood as a short outlook to the future work [38] that is planned based on the conclusions and results achieved so far in this thesis.

Instead of imposing constant pressure boundary conditions at the outflow section, a two-element Windkessel model is used to determine the pressure at the outlet. Since Eq. 5.5 does not admit an explicit solution in the general case, an approximation is needed for determining the pressure p_{out} at the outlet. This approximation is found by an Euler forward integration of Eq. 5.5 yielding

$$p_{\text{out}}^{t+h} = \int_t^{t+h} \frac{dp}{dt} \approx p_{\text{out}}^t + \frac{h}{C} \left(Q^t - \frac{p_{\text{out}}^t}{R} \right) \quad (5.8)$$

where h is the step size (time step) of the Euler method. p_{out}^t is the outlet pressure at time t , p_{out}^{t+h} the outlet pressure at time $t+h$, and Q^t denotes the flow at the outlet at time t . Since $\Delta t = 1$ in the LB simulations, $h = \Delta t = 1$. Eq. 5.8 then becomes

$$p_{\text{out}}^{t+1} \approx p_{\text{out}}^t + \frac{1}{C} \left(Q^t - \frac{p_{\text{out}}^t}{R} \right) \quad (5.9)$$

Eq. 5.9 is then used to update p_{out} at every time step. The procedure is as follows. After prescribing p_{out}^t at time $t = 0$,

1. compute Q^t in the LB simulations
2. use Q^t as input for the Windkessel model

3. compute p_{out}^{t+1} using Eq. 5.9
4. use p_{out}^{t+1} as input for the LB simulations
5. perform the LB simulations
6. proceed in time by restarting with point 1., with $t \rightarrow t + 1$

Since p_{out} is updated at every time instant by virtue of Eq. 5.9, the pressure at the outlet is not constant anymore but changes in time. As a consequence, the radius of the outflow section changes as well, which gives a more realistic outlet boundary condition, related to the arterial termination.

5.2.4.3 Preliminary results from first test simulations

A number of test simulations have been carried out to calibrate the parameters C and R . A channel with initial dimensions 500×40 embedded in a computational domain of dimensions 500×60 is considered. The numerical parameters have been chosen as $\nu = 1/6$ and $\alpha = 0.003$.

The response of the system to the following single pressure pulse prescribed at the inlet is studied.

$$\rho_{\text{in}}^{\text{pulse}} = \bar{\rho} + A e^{-50 \left(\frac{t - t_{\text{pulse}}}{2\beta} \right)^2} \quad (5.10)$$

where $A = 0.07$ and $\beta = 10$ are the amplitude and the width of the pulse, respectively. $\bar{\rho} = 1.0$ denotes the density when no pulse is present and $t_{\text{pulse}} = 10000$ is the time when the pulse has its maximum.

Several combinations of C and R have been tried and good results (expected response to the single pressure pulse, no unphysical oscillations) have been achieved with $C = 10^4$ and $R = 0.5$. The quality of the results are highly dependent on the parameters C and R . The range for C and R still needs to be studied and a compatibility relation with the parameters of the distributed model exists.

Figures 5.43 and 5.44 depict the density ρ_{out} (corresponding to p_{out}) and the flow Q_{out} at the outlet, as a function of time, respectively, gained from simulations with the parameters above. The first 6000 time steps have been omitted in the figures because the pulse occurs only at $t = 10000$. The effect of the pulse is clearly visible. No

unphysical oscillations appear in the time histories. The Windkessel responds in a smooth way to the single pulse.

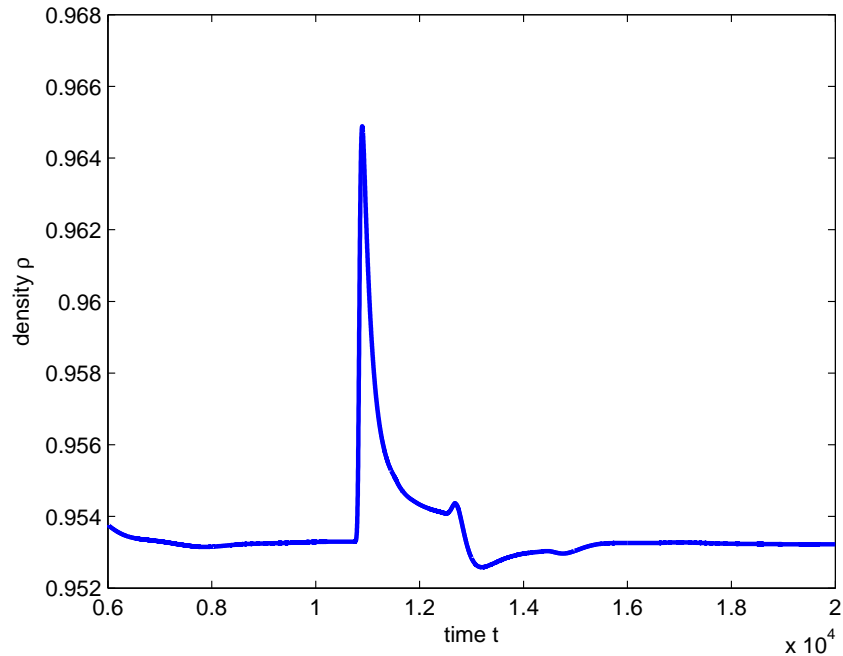


Figure 5.43: *Density ρ_{out} at the outlet as a function of time as a response to the single pulse given by Eq. 5.10. Coupled LBM/WK used with $C = 10^4$ and $R = 0.5$.*

The width of the channel at the outflow section is displayed in Fig. 5.45. Again the first 6000 time steps have been omitted. It can be observed that the width (and hence radius) changes when the pulse arrives at the outlet. Thus, the outlet section is not bounded anymore and can change in diameter over time.

Fig. 5.46 shows the velocity field for several points in time. It can be seen that the pulse travels across the channel and consequently the channel expands. However, the amplitude of the pulse is damped and the pulse disperses as it travels across the channel.

Such preliminary results encourage studying in more depth the coupling LBM/WK. Additional simulations are planned in the future [38] with an oscillating pressure at the inlet instead of the single pressure pulse used for the simulations up to now to enable physiological cases to be reproduced.

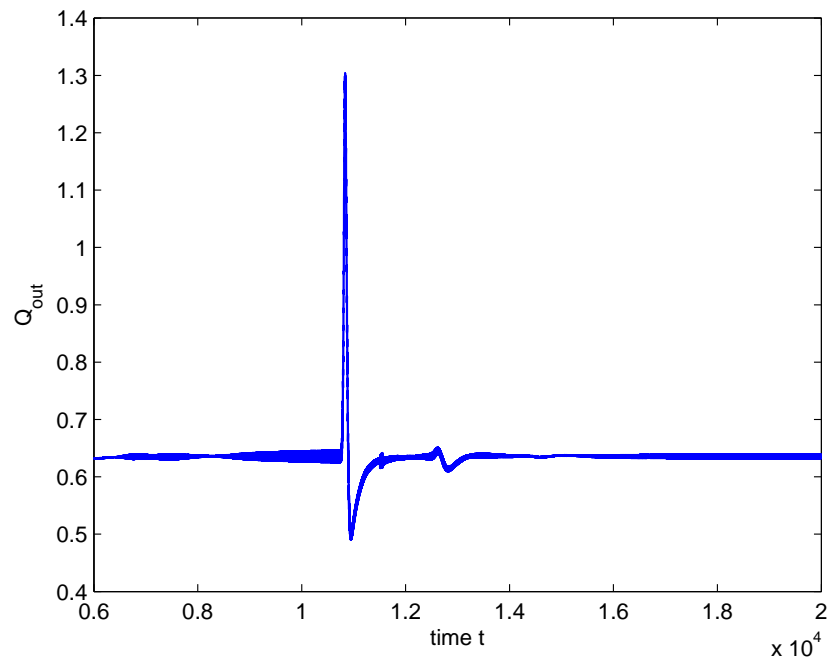


Figure 5.44: Flow Q_{out} at the outlet as a function of time as a response to the single pulse given by Eq. 5.10. Coupled LBM/WK used with $C = 10^4$ and $R = 0.5$.

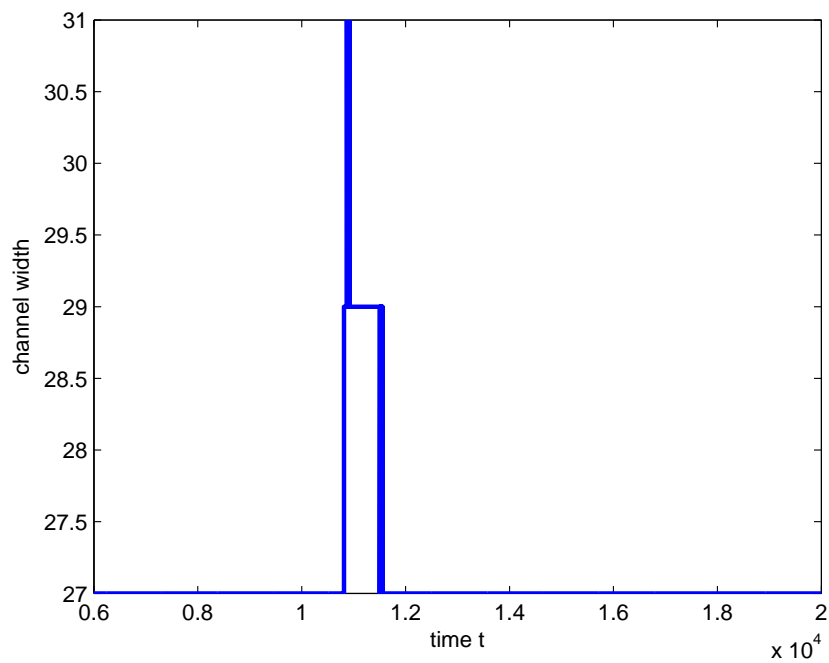


Figure 5.45: Width of the channel at the outlet as a function of time as a response to the single pulse given by Eq. 5.10. Coupled LBM/WK used with $C = 10^4$ and $R = 0.5$.

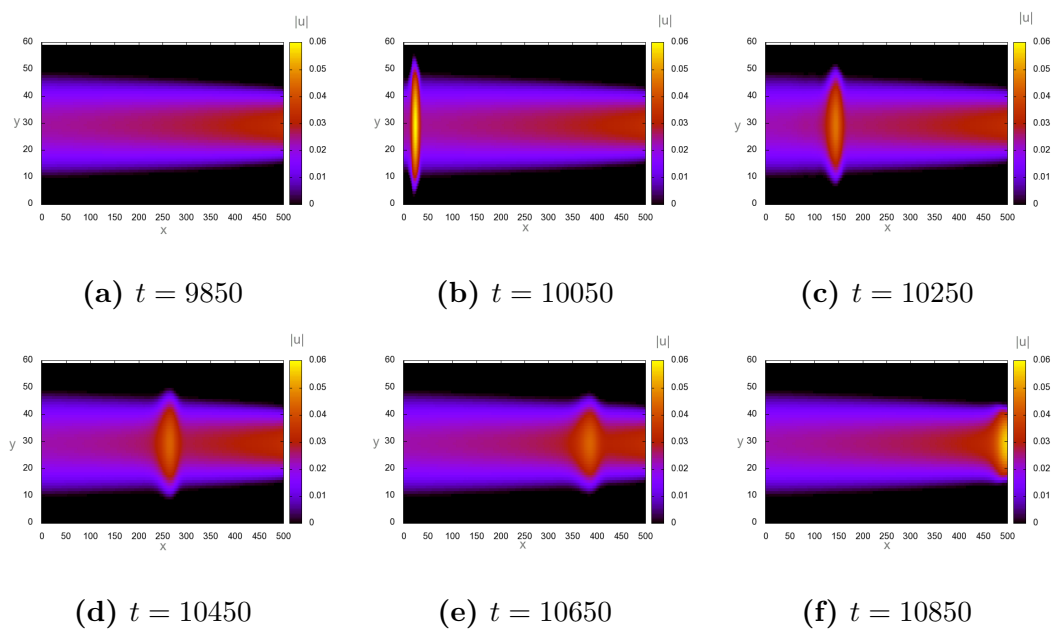


Figure 5.46: Velocity field in a compliant channel for different points in time (coupled LBM/WK with single pulse at inlet). The channel expands as the pulse travels across the channel.

Chapter 6

Towards physiological experiments: blood flow simulation through stents

The results of the numerical experiments presented in the previous chapter are promising and encourage using the developed method for modeling elastic walls for applications in hemodynamics. In particular, in this chapter the focus is on stents. A stent is a cylindrical wire mesh (made of metal or alloy) that is inserted into a narrowed artery to prevent its occlusion by sustaining the damaged vessel wall, see Fig. 6.1.

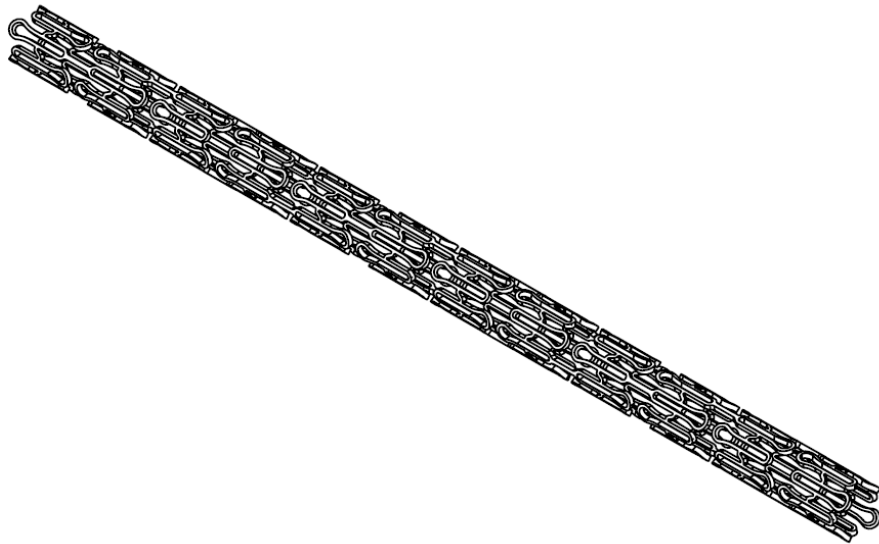


Figure 6.1: *Tenax™-Stent – BIOTRONIK SE & Co. KG Woermannkehe 1, 12359 Berlin, Germany*

This chapter starts with an overview of stents pointing out their main aspects and properties. In the second section, the modeling of the stent is detailed. It is based

on the methods and algorithms described in the previous chapters. Some preliminary results from numerical experiments are presented at the end of this chapter.

6.1 Arterial stents: an overview

The first clinical studies about stents implanted in arteries were published in the 1980's [47, 142, 169, 172, 206]. Since then, associated with the increase of cardiovascular diseases, research in that domain has gained importance. By now, the placement of stents in occluded or narrowed blood vessels is considered to be a clinical standard method. Nevertheless, only little is known about the exact behavior of blood flow in stented arteries. The geometry and the different elasticity of the stent, which is stiffer than the rest of the vessel, influence the blood flow pattern. Turbulences can occur. It is assumed that those turbulences can induce intimal hyperplasia and lead to a renewed narrowing of the artery, so-called *in-stent restenosis*. This pathological process prevalently occurs after stent implantation [107].

The problem of restenosis underlines the importance of fluid mechanics around stents by modeling and simulations. A variety of studies deal with different aspects related to the mechanical, biochemical, or geometrical properties of arterial stents, such as:

- clinical studies of particular stents [15, 17, 105, 115, 178, 186, 197, 210]
- possible risks of stent implantation [113]
- in-stent restenosis [14, 25, 49, 64, 65, 71, 88, 107, 184]
- stent design [37, 48, 97, 140, 141, 177]
- blood flow simulation in stented aneurysms [2, 78, 79, 208]
- biodegradable stents [33, 41, 75, 186, 193]
- drug-eluting stents [41, 63, 153, 154, 155, 171]
- requirements for the stent properties [139, 140, 190]
- historical overview on stent development [219]

A short summary of some of the aspects cited above will be given in the following subsections.

Possible risks of stent implantation

Even if nowadays stent implantation can be regarded as a clinical standard method, it is not without risks. First, it can injure the vessel which can cause a rupture in the wall or perforation. Then, the stent can be incorrectly deployed or move to a wrong location. Further complications are thrombosis due to oversized stent diameter and the formation of aneurysms.

Finally, if the neointimal tissue grows too much, a chronic narrowing of the vessel (restenosis) is possible. Restenosis is still one of the major problems occurring after stent implantation. Some causes of restenosis will be given hereafter.

In-stent restenosis

In-stent restenosis can be defined as the reoccurrence of stenosis in a dilated vessel occupying more than 50 percent of the vessel lumen [109]. Many clinical studies investigate the restenosis rates, see [179, 218] as well as [17, 107] and references therein.

As possible causes for restenosis the literature [109] cites neointimal hyperplasia (growth of neointimal tissue), inflammatory reactions, and diabetes mellitus. Besides that, restenosis can also be caused by the implantation procedure, e.g., by applying a high pressure at the dilatation process, by using several stents, or by injuring the vessel wall. Concerning the stent itself, further influencing factors are oversized stent diameter, length of the stent, stent design, geometric configuration, and stent compression.

Stent design

The stent design plays a crucial role for the positive outcome of the stent implantation. Stoeckel et al. [177] give a detailed overview of stent designs. More than 100 different designs exist, differing by the following aspects:

- material (nickel-titanium alloy, stainless steel, tantalum, cobalt alloys, etc.)
- form of the raw material (wire, tubing, ribbon, sheet)
- fabrication method (laser machining, photochemical etching, knitting, etc.)

- geometry (coil, helical spiral, individual rings)
- additional properties (drug-eluting coating, radiopaque coating, radiopaque markers)

Biodegradable stents

Most of the developed stents are permanent implants remaining lifelong in the vessel, far beyond the time needed to prevent wall recoil [41]. Because of the unclear function of the implant beyond the required period and the potential long-term complications associated with a permanent metal stent [33], the cardiology community is interested in the development of biodegradable stents.

The first biodegradable stent has been developed by Stack et al. in 1988 and implanted in animals [175]. For this prototype stent, a polymer of poly-L-lactide acid (PLLA) was used. In 2000, Tamai et al. [186] published the first report on initial and 6-month results after the placement of biodegradable PLLA stents in humans. A drawback of this stent was that it could not be entirely expanded by dilation. Heat supply, which potentially causes damage of the vessel wall, was necessary for the full expansion. In 2004, DiMario et al. [41] presented the first drug-eluting bioabsorbable magnesium stent. This implant had the drawback that it was completely radiolucent, which made the confirmation of correct placement and full expansion impossible.

The development of an appropriate biodegradable stent is still a difficult task. The main difficulty - and at the same time the most important feature - is the decomposition of the material in appropriate time.

Requirements for stent properties

Stent manufacturer have to consider several aspects when developing vascular implants. The requirements for the stent properties are as follows [109]:

- biocompatibility
- visibility (for verifying the correct placement and the full expansion)
- ability of elastic and plastic deformability at implantation and dilatation
- sufficient mechanical strength to sustain the vessel after dilatation

- sufficient fatigue strength to avoid fatigue crack and fatigue break of the stent structure
- easy to implant
- enabling of a long-term patency of the vessel
- smooth surface structure (reduces pressure gradients and prevents turbulences)
- corrosion resistance in the case of non-biodegradable stents

6.2 Modeling blood flow through a stented artery

Because only limited computational power was available for this study, only a restricted computational domain could be used in the simulations. This allowed modeling the stent only as stiffer part of the vessel segment without considering its detailed geometry. For including the exact geometry into the model, more computational power and memory is needed.

The developed model for the elastic wall presented in Chapter 4 can easily be applied to model the stents. The details about the modeling are specified hereafter.

Since the stented portion is stiffer than the rest of the vessel, it has a higher compliance parameter than the unstented part. Therefore, the idea to model the stent by varying the compliance parameter comes naturally. Instead of taking a constant α in the pressure-radius relationship (Eq. 4.2), α is increased in the stiffer part representing the stent. Thus, α varies with x , i.e., $\alpha = \alpha(x)$. Let α_s denote the elasticity parameter of the stent and α_0 the elasticity parameter of the unstented vessel. In order to avoid a discontinuity in $\alpha(x)$ at the edges of the stent due to the considerable difference between the compliant vessel and the more rigid stented part, α is chosen as a rapidly changing function as in [156].

$$\alpha(x) = \alpha_0 \left(1 + \delta e^{-\left(\frac{x-x^*}{\sigma}\right)^8} \right) \quad (6.1)$$

Here, σ is half of the stent length, x^* is the point around which the stent is centered,

and $\delta = \frac{\alpha_s - \alpha_0}{\alpha_0}$. For $\alpha_s = \alpha_0$, the compliance parameter of the unstented vessel is recovered in Eq. 6.1. By varying the value of σ and δ it is possible to roughly model a number of mechanical properties of stents and the local stiffening or softening of the artery [156].

With $\alpha = \alpha(x)$ defined by Eq. 6.1, the pressure-radius relationship (Eq. 4.2) used for determining the pressure thresholds p_{th} is generalized as

$$p_{th} = p_0 + \alpha(x)(R - R_0). \quad (6.2)$$

By this, nodes corresponding to the stented part have higher pressure thresholds than nodes representing the unstented vessel wall. As described in Chapter 4, the pressure thresholds are coupled to the parameter q of the continuous bounce-back boundary condition. In analogy to Eq. 4.4, the relation is

$$q(x, y_b) = \frac{p(x, y_b) - p_{th}(x, y_b)}{\alpha(x, y_b)}. \quad (6.3)$$

The following section presents preliminary results from simulations including the modeling described above.

6.3 Preliminary numerical experiments

The numerical experiments presented in this section only intend to show the feasibility of the developed algorithm. For more informative results, more computing power is needed. To underline this fact, it is reminded that the diameter of a blood vessel typically changes by maximum 10% [165]. Considering a channel with initial radius of 20 lattice units, the wall should not change by more than two lattice units, which does not allow to generate figures of the vessel with smooth shape.

For the numerical experiments, a channel of dimensions 500×40 is considered, embedded in a computational domain of dimensions 500×60 . A stent of length 100 lattice units is imagined to be located in the middle of the vessel, so $\sigma = 50$ and $x^* = 250$. The compliance parameter α_0 of the unstented part has been chosen 0.007. An oscillating

pressure is prescribed at the inlet, whereas constant pressure boundary conditions are imposed at the outlet (the coupling LBM/WK not being developed and tested in detail so far).

Simulations with different α_s have been carried out and the ratio between the stented and the unstented maximum deformation at the center of the stented segment has been calculated. Fig. 6.2 depicts this ratio as a function of α_s/α_0 . As expected, the ratio decreases with α_s/α_0 and tends asymptotically to the value of the rigid wall.

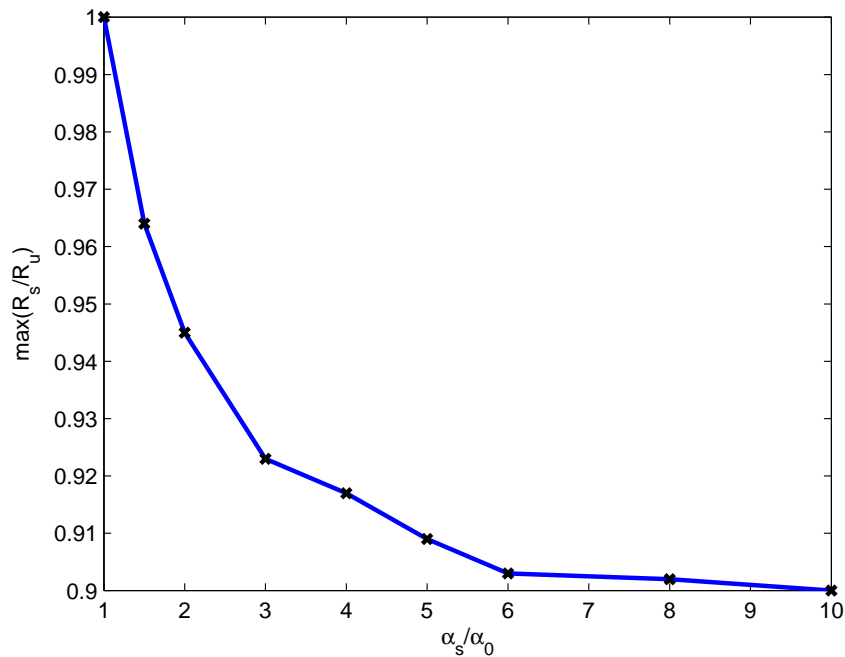


Figure 6.2: Ratio between the stented and the unstented maximum deformation at the center of the stented segment ($\alpha_0 = 0.007$). R_s and R_u denote the radius of stented and unstented vessel, respectively.

As a consequence of the perturbed flow field, the time evolutions of the wall shear stress at the beginning and the end of the stented segment exhibit strong oscillations, see Figures 6.3 and 6.4. It should be reminded of the correlation between the wall shear stress and the development of atherosclerosis, see Section 2.3. There is significant evidence that highly oscillating WSS causes intimal wall thickening [170]. Interpreting the presented results, this would mean that the proximal and distal ends of the stent are prone to blood stagnancy, tissue growth, increased coagulation and, as a consequence, to restenosis.

The presented results show that the developed method can be successfully applied for

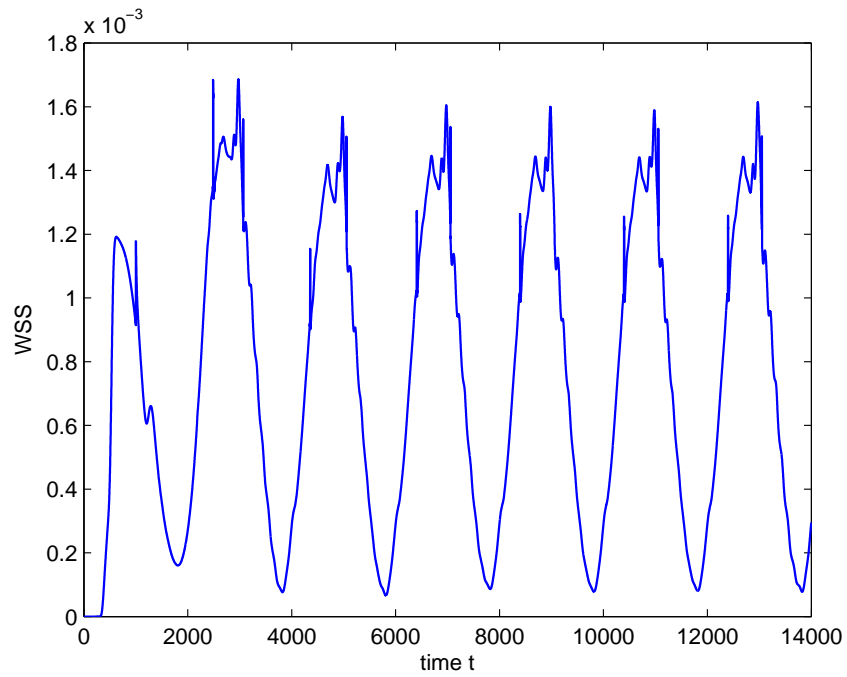


Figure 6.3: Wall shear stress at the upper wall at the beginning of the stented segment as a function of time ($\alpha_0 = 0.07$, $\sigma = 50$)

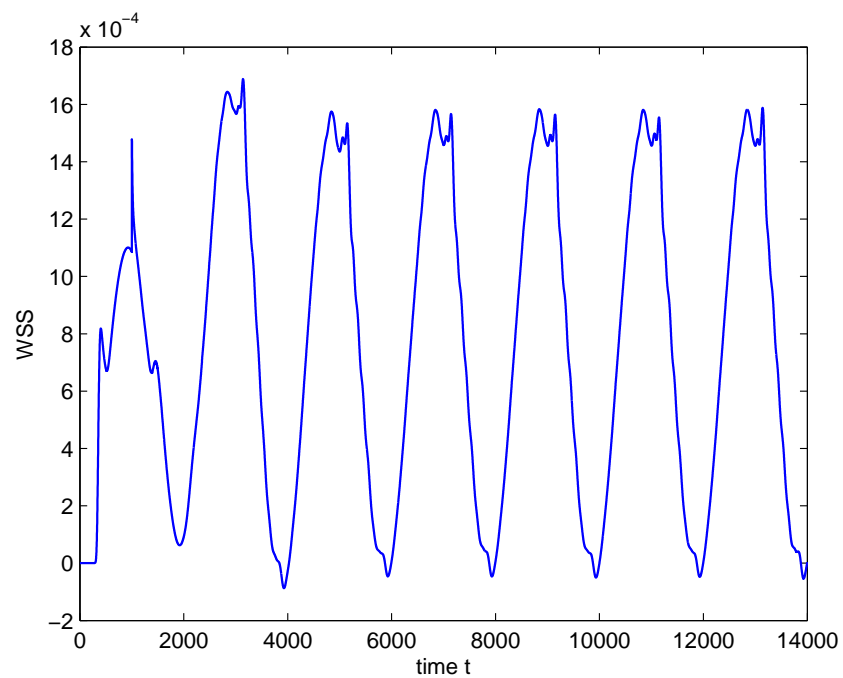


Figure 6.4: Wall shear stress at the upper wall at the end of the stented segment as a function of time ($\alpha_0 = 0.07$, $\sigma = 50$)

a deeper investigation the blood flow through stents. However, to gain more significant results, further improvement of the method is required. Especially, when interested in the propagation of pulse waves, the presented model needs to be enriched and the algorithm suitably adjusted.

Summary and conclusions

Mathematical models for the cardiovascular system are widely used to simulate blood flow in arteries and to predict dynamic patterns in physiological and pathological conditions. Nowadays, computational modeling and simulation have emerged as important tools for a deeper understanding of the physical concurrent factors that influence the flow field.

With this objective, an accurate and computationally efficient method for modeling incompressible flows in distensible tubes has been developed using the lattice Boltzmann method. It constitutes an improvement of the method proposed by D. Leitner [99]. Compared to the approach presented in [99] by which the wall can only be displaced in a discrete way over the underlying lattice, the current method is especially devised for allowing a continuous wall motion.

Using the lattice Boltzmann method for the simulations has many advantages compared to conventional solvers for computational fluid dynamics problems. The explicit scheme allows for an easy implementation and the local nature of the LB algorithm makes it suitable for parallel computing. The developed approach for modeling elastic walls acts locally as the LB method itself, which makes the coupled algorithm computationally efficient, even for simulations in complex geometries.

The developed algorithm has been implemented in the programming language C and extensive numerical experiments have been carried out to show the feasibility and the effectiveness of the method. The velocity field in a cylindrical tube was in good agreement with the analytical solution and the results showed the expected physical behavior. The results presented in this work are not complete but intend to show the feasibility of the methodology for applications in which the compliance of the wall plays a relevant role.

The implemented simulation environment can be applied to hemodynamics to study the pressure and flow fields in elastic vessels and has been extended to model the blood

flow through stents. A linear pressure-radius relationship has been assumed for this work, but the presented method is able to treat more complex tube laws as long as they are explicit. However, before the model can be used to study physiological flows in a predictive way, several parameters contained in the model need to be identified. Measurement data are necessary for validation of the model and for quantitatively describe the blood flow in compliant vessels.

Some results pointed out the weakness of the method as it is developed so far. It was not possible to study the propagation of pulse waves which certainly is important in many applications, especially in hemodynamics where the pulse wave velocity gives evidence of the stiffness of the vessel and can be used as an indicator for unhealthy states. A possible reason for this is that the method for coupling the elastic vessel and the enclosed fluid is not a real fluid-structure interaction problem because the retroaction from the wall back to the fluid is missing. For this, further extension of the method is needed (for example by using a longitudinal elasticity model that links the LB nodes near the wall). Another reason could be the outlet condition bounding the terminal section. In order to circumvent this problem, the LB algorithm has been coupled with a Windkessel model accounting for the terminal system. The preliminary results of some test simulations are promising and encourage to further develop the LBM/WK coupling.

Despite the limitation of the presented method, it constitutes a valuable computational tool because it is simple while at the same time able to predict flow and pressure fields in distensible tubes and to provide first qualitative and quantitative results. By showing the relationship between the several variables and parameters, the model can be used to identify simple indices and clinical indicators of biomedical significance. It would be interesting to further elaborate and extend the approach in such a way that wave propagation can be studied and to validate the enhanced model with real physiological data. Furthermore, the availability of more computing power enabling to run simulations with a bigger computational domain would allow to investigate the effects of different stent geometries or other vascular prostheses on the blood flow.

List of Figures

| | | |
|-----|--|----|
| 2.1 | Straight tube with circular cross section | 8 |
| 2.2 | The parabolic velocity profile (u_z) of a fully developed steady Poiseuille flow. The average velocity \bar{u}_z is one half of the maximum velocity. At the wall, the velocity is zero (no-slip condition). | 10 |
| 2.3 | Time-dependent Womersley flow with $\Omega \approx 0.056$ ($\omega = \frac{2\pi}{5000}$, $\nu = 0.4$, $R = 1$, in arbitrary units) | 13 |
| 2.4 | Distensible axisymmetric tube of length L with circular cross section | 14 |
| 2.5 | Components of the stress tensor on an infinitesimal cubic element in the Cartesian coordinate system | 16 |
| 2.6 | Transversal section of a tube of thickness h | 18 |
| 3.1 | Top-down versus bottom-up approach | 23 |
| 3.2 | Propagation step: each population is propagated to the neighboring node corresponding to the direction of its velocity. | 26 |
| 3.3 | $D2Q9$ lattice | 28 |
| 3.4 | $D3Q15$ lattice | 29 |
| 3.5 | $D3Q19$ lattice | 30 |
| 3.6 | Periodic boundary conditions | 35 |
| 3.7 | No-slip boundary condition: bounce-back on the node (left) and halfway bounce-back on the link (right). The red filled circles represent fluid nodes; the gray crosses describe solid nodes. Full arrows indicate outgoing populations; dashed arrows denote reflected incoming populations | 36 |
| 3.8 | Continuous bounce-back boundary condition for a virtual wall located at distance q from the last fluid node x_j . Gray crosses indicate solid nodes, red filled circles denote fluid nodes. The lattice spacing Δx is set to one. Dashed blue arrows represent directions i of unknown populations f_i which are determined using the linear interpolation in Eqs. 3.29 or 3.30. | 38 |
| 3.9 | Inlet/outlet boundary conditions. Dashed arrows indicate unknown populations; full arrows denote known particles. | 40 |

| | | |
|------|---|----|
| 3.10 | Inlet/outlet boundary conditions for a corner node. Dashed arrows indicate unknown populations; full arrows denote known populations. . . | 42 |
| 4.1 | Sketch of lattice illustrating the concept of wall displacement based on node type changes. Gray crosses indicate solid nodes; red filled circles denote fluid nodes. The dark red disk designates a node that has changed its type. The virtual wall (dashed line) separates the solid and the fluid domain. | 46 |
| 4.2 | Sketch of the initialization of new fluid nodes (dark red disks). (a) Example of a new fluid node having solid neighbors in direction 1 and 3. f_1 and f_3 at the new fluid node are set to their equilibrium values. (b) Example of a new fluid node having fluid neighbors in direction 6 and 8. f_6 and f_8 at the new fluid node are gained from propagation. (c) Example of a new fluid node having a fluid neighbor in direction 8 and a solid neighbor in the opposite direction (6). At the new fluid node, f_6 is gained from propagation and f_8 using the bounce-back rule for the non-equilibrium part. | 47 |
| 4.3 | Sketch of lattice showing which nodes (domain inside the blue frame) are affected by the local rescaling method | 49 |
| 4.4 | Sketch of lattice showing which nodes (domain inside the blue frame) are affected by the rescaling by columns method | 50 |
| 4.5 | Continuous bounce-back boundary condition for a virtual wall located at distance q from the last fluid node. To every fluid node next the the wall a different q is assigned. Gray crosses indicate solid nodes; red filled circles denote fluid nodes. The lattice spacing Δx is set to one. | 50 |
| 5.1 | Sketch of lattice with embedded vessel | 56 |
| 5.2 | Flow chart of the implemented lattice Boltzmann algorithm | 57 |
| 5.3 | Example of memory allocation for the distribution functions $f_i(x, y)$. The helper function translates x , y and i from a matrix form to the position in the linear array. | 58 |
| 5.4 | Velocity: Comparison between analytical solution of Poiseuille (green) and numerical result (blue) (periodic BC) | 61 |
| 5.5 | Velocity field of fully developed flow in a rigid straight channel. The black area corresponds to solid nodes. | 62 |
| 5.6 | Total mass as a function of time. In order to better distinguish between the single steps (1. to 5., see text), the algorithm waits for at least 100 time steps and for fully developed flow before performing the next step. | 63 |

| | | |
|------|---|----|
| 5.7 | Density at fluid node next to the upper wall as a function of time (local rescaling used) | 64 |
| 5.8 | Velocity component u_x at fluid node next to the upper wall as a function of time (local rescaling used) | 65 |
| 5.9 | Velocity component u_y at fluid node next to the upper wall as a function of time (local rescaling used) | 65 |
| 5.10 | Density at fluid node next to the upper wall as a function of time (rescaling by columns used). Since rescaling by column affects the flow field in the whole channel, expansion and contraction can occur at different points in time. | 67 |
| 5.11 | Velocity component u_x at fluid node next to the upper wall as a function of time (rescaling by columns used) | 68 |
| 5.12 | Velocity component u_y at fluid node next to the upper wall as a function of time (rescaling by columns used) | 68 |
| 5.13 | Time at which flow is fully developed as a function of the diffusive time t_d (ν varying) | 70 |
| 5.14 | Recovery time after expansion (blue, $H = 42$) and contraction (green, $H = 40$) as a function of the diffusive time t_d (ν varying) | 70 |
| 5.15 | Density at fluid node next to the wall as a function of time, lower viscosity ($\nu = 1/30$), compare with Fig. 5.7. | 71 |
| 5.16 | Velocity component u_x at fluid node next to the wall as a function of time, lower viscosity ($\nu = 1/30$), compare with Fig. 5.8 | 71 |
| 5.17 | Recovery times as a function of the tolerance ϵ | 72 |
| 5.18 | Comparison between computed velocity profile (blue) and analytical solution of Poiseuille (green) with density difference $\Delta\rho = 0.02$ between inlet and outlet (inlet/outlet BC) | 75 |
| 5.19 | Velocity profiles of fully developed flow along x in a rigid straight channel (a) and a rigid channel with curved walls (b) | 75 |
| 5.20 | Time history of the density ρ (a) and the velocity component u_x (b) at the center node of the channel | 76 |
| 5.21 | Density ρ as a function of time at a node near the wall (bounce-back on the link, see Section 3.3.2) | 77 |
| 5.22 | Velocity component u_x as a function of time at a node near the wall (bounce-back on the link, see Section 3.3.2) | 77 |
| 5.23 | Moving average over 250 time steps of the velocity component u_x at different lattice nodes (blue and red for a node with central y -coordinate, green and black for a node with y -coordinate near the upper wall) | 78 |

| | | |
|------|---|----|
| 5.24 | Density ρ as a function of time at a node near the wall (continuous bounce-back) | 79 |
| 5.25 | Velocity component u_x as a function of time at a node near the wall (continuous bounce-back) | 80 |
| 5.26 | Total mass as a function of time | 80 |
| 5.27 | Surface plot of the velocity component u_y at time $t = 6000$ | 81 |
| 5.28 | Velocity field at time $t = 6000$ | 81 |
| 5.29 | Profiles of the velocity component u_x along the channel at three instants in the case of oscillating inlet pressure. The scale of these figures do not allow a precise resolution, but the channel in case (b) is slightly more expanded than in case (a), and the channel in case (c) is more expanded than in case (a) and (b). The wall displacement of just one or two lattice units is not clearly visible in the figures. | 82 |
| 5.30 | Velocity field in a compliant channel for different points in time. The channel expands and contracts (by a few lattice units) as time is progressing. | 83 |
| 5.31 | Virtual radius R at every position x for different points in time | 84 |
| 5.32 | Parameter q of continuous bounce-back condition for a fixed node at the lower wall | 84 |
| 5.33 | Histograms for the parameter q of the continuous bounce-back condition at the lower boundary over one pulse period: (a) all x including inlet and outlet; (b) all x except inlet and outlet. The prominent peak in case (a) is due to the boundary condition at the outlet which bounds the outlet section because of the prescribed constant pressure (and as a consequence constant q). The smaller peaks around zero and one are due to the fact that q is reset to zero or one after creation or destruction of a fluid node when the excess Δq is greater than one, see Section 4.3 | 85 |
| 5.34 | Maximum radius as a function of the compliance parameter α | 86 |
| 5.35 | Virtual radius R at every position x for different points in time, gained from simulations with different α . Expansion and contraction are allowed only after 1000 time steps when the flow is fully developed. Hence, at $t = 500$, the channel keeps its initial state (straight). | 87 |

| | | |
|------|---|----|
| 5.36 | Histograms for the parameter q of the continuous bounce-back condition at the lower boundary over one pulse period, gained from simulations with different α . In each case, the prominent peak is due to the boundary condition at the outlet which bounds the outlet section because of the prescribed constant pressure, see Eq. 5.4 (and as a consequence constant q). | 87 |
| 5.37 | Contour plot of the virtual radius R , gained from simulations with different α . Different colors correspond to different values of R . Note that the scaling is not the same in case (a) and (b). | 88 |
| 5.38 | Virtual radius R at every position x for different points in time, gained from simulations with different amplitude A | 89 |
| 5.39 | Histograms for the parameter q of the continuous bounce-back condition at the lower boundary over one pulse period, gained from simulations with different amplitude A . In each case, the prominent peak (around 0.85) is due to the boundary condition at the outlet which bounds the outlet section because of the prescribed constant pressure (and as a consequence constant q). The peaks around zero and one are due to the fact that q is reset to zero or one after creation or destruction of a fluid node when the excess Δq is greater than one, see Section 4.3 | 90 |
| 5.40 | Virtual radius R at every position x for different points in time, gained from simulations with different pulse period T_{pulse} | 90 |
| 5.41 | Histograms for the parameter q of the continuous bounce-back condition at the lower boundary over one pulse period, gained from simulations with different T_{pulse} . In each case, the prominent peak (around 0.85) is due to the boundary condition at the outlet which bounds the outlet section because of the prescribed constant pressure (and as a consequence constant q). | 91 |
| 5.42 | The Windkessel model (a) and the equivalent representation as electric circuit (b). Q_{in} is the flow into the Windkessel, C denotes the compliance/capacitance and R represents the resistance. | 93 |
| 5.43 | Density ρ_{out} at the outlet as a function of time as a response to the single pulse given by Eq. 5.10. Coupled LBM/WK used with $C = 10^4$ and $R = 0.5$ | 96 |
| 5.44 | Flow Q_{out} at the outlet as a function of time as a response to the single pulse given by Eq. 5.10. Coupled LBM/WK used with $C = 10^4$ and $R = 0.5$ | 97 |

| | | |
|------|---|-----|
| 5.45 | Width of the channel at the outlet as a function of time as a response to the single pulse given by Eq. 5.10. Coupled LBM/WK used with $C = 10^4$ and $R = 0.5$ | 97 |
| 5.46 | Velocity field in a compliant channel for different points in time (coupled LBM/WK with single pulse at inlet). The channel expands as the pulse travels across the channel. | 98 |
| 6.1 | Tenax TM -Stent – BIOTRONIK SE & Co. KG Woermannkehre 1, 12359 Berlin, Germany | 99 |
| 6.2 | Ratio between the stented and the unstented maximum deformation at the center of the stented segment ($\alpha_0 = 0.007$). R_s and R_u denote the radius of stented and unstented vessel, respectively. | 105 |
| 6.3 | Wall shear stress at the upper wall at the beginning of the stented segment as a function of time ($\alpha_0 = 0.07$, $\sigma = 50$) | 106 |
| 6.4 | Wall shear stress at the upper wall at the end of the stented segment as a function of time ($\alpha_0 = 0.07$, $\sigma = 50$) | 106 |

List of Tables

| | | |
|-----|--|----|
| 3.1 | Weighting factors of the $D2Q9$ LBGK lattice | 28 |
| 3.2 | Weighting factors of the $D3Q15$ LBGK lattice | 29 |
| 3.3 | Weighting factors of the $D3Q19$ LBGK lattice | 29 |
| 5.1 | Memory requirements for the main variables for a $D2Q9$ lattice of dimensions $N_x \times N_y$ | 58 |
| 5.2 | Correspondance of hydrodynamic and electric variables | 94 |

Bibliography

- [1] D.J. Acheson. *Elementary Fluid Dynamics*. Oxford University Press, USA, 1990.
- [2] M. Aenis, A.P. Stancampiano, A.K. Wakhloo, and B.B. Lieber. Modeling of flow in a straight stented and nonstented side wall aneurysm model. *Journal of Biomechanical Engineering*, 119:206, 1997.
- [3] C.K. Aidun, Y. Lu, and E.J. Ding. Direct analysis of particulate suspensions with inertia using the discrete Boltzmann equation. *Journal of Fluid Mechanics*, 373:287–311, 1998.
- [4] A.J. Alastruey. *Numerical modelling of pulse wave propagation in the cardiovascular system: development, validation and clinical applications*. PhD thesis, University of London, 2006.
- [5] A.D. Angelopoulos, V.N. Paunov, V.N. Burganos, and A.C. Payatakes. Lattice Boltzmann simulation of nonideal vapor-liquid flow in porous media. *Physical Review E*, 57(3):3237–3245, 1998.
- [6] R. Argentini, A.F. Bakker, and C.P. Lowe. Efficiently using memory in lattice Boltzmann simulations. *Future Generation Computer Systems*, 20(6):973–980, 2004.
- [7] A.M. Artoli. *Mesosopic computational haemodynamics*. PhD thesis, University of Amsterdam, 2003.
- [8] A.M. Artoli, A.G. Hoekstra, and P.M.A. Slood. Simulation of a systolic cycle in a realistic artery with the Lattice Boltzmann BGK method. *International Journal of Modern Physics B*, 17:95–98, 2003.
- [9] A.M. Artoli, A.G. Hoekstra, and P.M.A. Slood. Mesoscopic simulations of systolic

- flow in the human abdominal aorta. *Journal of Biomechanics*, 39(5):873–884, 2006.
- [10] A.M. Artoli, A.G. Hoekstra, and P.M.A. Slood. Optimizing lattice Boltzmann simulations for unsteady flows. *Computers and Fluids*, 35(2):227–240, 2006.
- [11] A.M. Artoli, D. Kandhai, H.C.J. Hoefsloot, A.G. Hoekstra, and P.M.A. Slood. Lattice Boltzmann, a robust and accurate solver for interactive computational hemodynamics. In *Computational science-ICCS 2003: International conference, Melbourne, Australia and St. Petersburg, Russia, June 2-4, 2003: proceedings: pt. I*, volume 2657, pages 1034–1043. Springer, 2003.
- [12] A.M. Artoli, D. Kandhai, H.C.J. Hoefsloot, A.G. Hoekstra, and P.M.A. Slood. Lattice BGK simulations of flow in a symmetric bifurcation. *Future Generation Computer Systems*, 20(6):909–916, 2004.
- [13] A.M.M. Artoli, B.D. Kandhai, H.G. Hoefsloot, A.G. Hoekstra, and P.M.A. Slood. Shear Stress in Lattice Boltzmann Simulations. In *Europhysics Conference on Computational Physics in series Publication Series of the John von Neumann Institute for Computing*, page A127, 2001.
- [14] C. Bauters, E. Hubert, A. Prat, K. Bougrimi, E. Van Belle, E.P. McFadden, P. Amouyel, J.M. Lablanche, and M. Bertrand. Predictors of restenosis after coronary stent implantation. *Journal of the American College of Cardiology*, 31(6):1291–1298, 1998.
- [15] G.A. Beathard. Gianturco self-expanding stent in the treatment of stenosis in dialysis access grafts. *Kidney international*, 43:872–872, 1993.
- [16] R. Benzi, S. Succi, and M. Vergassola. The lattice Boltzmann equation: theory and applications. *Physics Reports*, 222(3):145–197, 1992.
- [17] P. Bergeron, J.J. Pinot, V. Poyen, H. Benichou, P. Khanoyan, P. Rudondy, Y. Wang, S. Chiarandini, R. El Hussein, R. Rieu, et al. Long-term results with the Palmaz stent in the superficial femoral artery. *Journal of Endovascular Surgery*, 2(2):161–167, 1995.
- [18] P.L. Bhatnagar, E.P. Gross, and M. Krook. A model for collision processes

- in gases. I. Small amplitude processes in charged and neutral one-component systems. *Physical Review*, 94(3):511–525, 1954.
- [19] L. Boltzmann. Weitere Studien über das Wärmegleichgewicht unter Gasmolekülen. *Sitzungsberichte der Akademie der Wissenschaften*, 66:275–370, 1872.
- [20] M. Bouzidi, M. Firdaouss, and P. Lallemand. Momentum transfer of a Boltzmann-lattice fluid with boundaries. *Physics of Fluids*, 13:3452, 2001.
- [21] J. Boyd, J. Buick, J.A. Cosgrove, and P. Stansell. Application of the lattice Boltzmann model to simulated stenosis growth in a two-dimensional carotid artery. *Physics in Medicine and Biology*, 50(20):4783, 2005.
- [22] K. Bryan. A numerical method for the study of the circulation of the world ocean. *Journal of Computational Physics*, 4(3):347–376, 1969.
- [23] G.A. Buxton, R. Verberg, D. Jasnow, and A.C. Balazs. Newtonian fluid meets an elastic solid: Coupling lattice Boltzmann and lattice-spring models. *Physical Review E*, 71(5):056707–1, 2005.
- [24] A. Caiazzo. *Asymptotic Analysis of lattice Boltzmann method for Fluid-Structure interaction problems*. PhD thesis, Technische Universität Kaiserslautern, 2007.
- [25] A. Caiazzo, D. Evans, J.L. Falcone, J. Hegewald, E. Lorenz, B. Stahl, D. Wang, J. Bernsdorf, et al. A complex automata approach for in-stent restenosis: two-dimensional multiscale modelling and simulations. *Journal of Computational Science*, 2:9–17, 2011.
- [26] S. Chapman and T.G. Cowling. *The Mathematical Theory of Nonuniform Gases*. Cambridge University Press, 1970.
- [27] C. Chen, H. Chen, D. Freed, R. Shock, I. Staroselsky, R. Zhang, A. Ümit Coşkun, P.H. Stone, and C.L. Feldman. Simulation of blood flow using extended Boltzmann kinetic approach. *Physica A: Statistical Mechanics and its Applications*, 362(1):174–181, 2006.
- [28] S. Chen, H. Chen, D. Martínez, and W. Matthaeus. Lattice Boltzmann model for simulation of magnetohydrodynamics. *Physical Review Letters*, 67(27):3776–3779, 1991.

-
- [29] S. Chen and G.D. Doolen. Lattice Boltzmann method for fluid flows. *Annual Reviews in Fluid Mechanics*, 30(1):329–364, 1998.
- [30] S. Chen, D. Martínez, and R. Mei. On boundary conditions in lattice Boltzmann methods. *Physics of Fluids*, 8:2527, 1996.
- [31] B. Chopard and S. Marconi. Lattice Boltzmann solid particles in a lattice Boltzmann fluid. *Journal of Statistical Physics*, 107(1):23–37, 2002.
- [32] D.S. Clague and P.J. Cornelius. The hydrodynamic force and torque on a bounded sphere in Poiseuille flow. *International Journal for Numerical Methods in Fluids*, 35(1):55–70, 2001.
- [33] A. Colombo and E. Karvouni. Biodegradable stents: ‘Fulfilling the mission and stepping away’. *Circulation*, 102(4):371–373, 2000.
- [34] R. Cornubert, D. d’Humières, and D. Levermore. A Knudsen layer theory for lattice gases. *Physica D: Nonlinear Phenomena*, 47(1-2):241–259, 1991.
- [35] J.A. Cosgrove, J.M. Buick, S.J. Tonge, C.G. Munro, C.A. Greated, and D.M. Campbell. Application of the lattice Boltzmann method to transition in oscillatory channel flow. *Journal of Physics A: Mathematical and General*, 36(10):2609–2620, 2003.
- [36] S.P. Dawson, S. Chen, and GD Doolen. Lattice Boltzmann computations for reaction-diffusion equations. *The Journal of chemical physics*, 98:1514–1523, 1993.
- [37] S. De Bock, F. Iannaccone, G. De Santis, M. De Beule, P. Mortier, B. Verheghe, and P. Segers. Our capricious vessels: The influence of stent design and vessel geometry on the mechanics of intracranial aneurysm stent deployment. *Journal of biomechanics*, 45(8):1353–1359, 2012.
- [38] X. Descovich, G. Pontrelli, S. Melchionna, S. Succi, and M. Bammer. A lattice Boltzmann model for blood flow in vessels with elastic walls. In preparation, 2012.
- [39] X. Descovich, G. Pontrelli, S. Melchionna, S. Succi, and M. Bammer. Modelling elastic walls in lattice Boltzmann simulations for applications in haemodynamics.

- In *Proceedings of The International Workshop on Applied Modeling & Simulation, Rome, September 24-27, 2012*, 2012.
- [40] X. Descovich, G. Potrelli, S. Succi, S. Melchionna, and M. Bammer. Modeling Elastic Walls in Lattice Boltzmann Simulations of Arterial Blood Flow. In *Proceedings of MATHMOD 2012 conference, Vienna, February 14-17, 2012*, 2012.
- [41] C. Di Mario, H. Griffiths, O. Goktekin, N. Peeters, J. Verbist, M. Bosiers, K. De-loose, B. Heublein, R. Rohde, V. Kasese, et al. Drug-eluting bioabsorbable magnesium stent. *Journal of Interventional Cardiology*, 17(6):391–395, 2004.
- [42] E.J. Ding and C.K. Aidun. The dynamics and scaling law for particles suspended in shear flow with inertia. *Journal of Fluid Mechanics*, 423:317–344, 2000.
- [43] E.J. Ding and C.K. Aidun. Extension of the lattice-Boltzmann method for direct simulation of suspended particles near contact. *Journal of Statistical Physics*, 112(3):685–708, 2003.
- [44] U. Dinnar. *Cardiovascular Fluid Dynamics*, volume 264. CRC Press Boca Raton, FL, 1981.
- [45] G.M. Doctors. *Towards patient-specific modelling of cerebral blood flow using lattice-Boltzmann methods*. PhD thesis, University College London, 2011.
- [46] G.M. Doctors, M.D. Mazzeo, and P.V. Coveney. A computationally efficient method for simulating fluid flow in elastic pipes in three dimensions. *Computer Physics Communications*, 181(9):1584–1592, 2010.
- [47] C.T. Dotter, R.W. Buschmann, M.K. McKinney, and J. Rosch. Transluminal expandable nitinol coil stent grafting: preliminary report. *Radiology*, 147(1):259–260, 1983.
- [48] T.W. Duerig, D.E. Tolomeo, and M. Wholey. An overview of superelastic stent design. *Minimally Invasive Therapy and Allied Technologies*, 9(3/4):235–246, 2000.
- [49] G.R. Dussailant, G.S. Mintz, A.D. Pichard, K.M. Kent, L.F. Satler, J.J. Popma, S.C. Wong, and M.B. Leon. Small stent size and intimal hyperplasia contribute

- to restenosis: a volumetric intravascular ultrasound analysis. *Journal of the American College of Cardiology*, 26(3):720–724, 1995.
- [50] Eurostat. *Health statistics – Atlas on mortality in the European Union*. Office for Official Publications of the European Communities, Luxembourg, 2009.
- [51] H. Fang, Z. Lin, and Z. Wang. Lattice Boltzmann simulation of viscous fluid systems with elastic boundaries. *Physical Review E*, 57(1):25–28, 1998.
- [52] H. Fang, Z. Wang, Z. Lin, and M. Liu. Lattice Boltzmann method for simulating the viscous flow in large distensible blood vessels. *Physical Review E*, 65(5):51925, 2002.
- [53] Z.G. Feng and E.E. Michaelides. Interparticle forces and lift on a particle attached to a solid boundary in suspension flow. *Physics of Fluids*, 14:49, 2002.
- [54] O. Filippova and D. Hänel. Grid refinement for lattice-BGK models. *Journal of Computational Physics*, 147(1):219–228, 1998.
- [55] O. Filippova and D. Hänel. A novel lattice BGK approach for low Mach number combustion. *Journal of Computational Physics*, 158(2):139–160, 2000.
- [56] O. Filippova and D. Hänel. Acceleration of lattice-BGK schemes with grid refinement. *Journal of Computational Physics*, 165(2):407–427, 2000.
- [57] O. Frank. Die Grundform des arteriellen Pulses. *Zeitung für Biologie*, 37:483–526, 1899.
- [58] M.H. Friedman, C.B. Bargeron, D.D. Duncan, G.M. Hutchins, F.F. Mark, et al. Effects of arterial compliance and non-newtonian rheology on correlations between intimal thickness and wall shear. *Journal of Biomechanical Engineering*, 114(3):317–320, 1992.
- [59] M.H. Friedman, G.M. Hutchins, C. Brent Bargeron, O.J. Deters, and F.F. Mark. Correlation between intimal thickness and fluid shear in human arteries. *Atherosclerosis*, 39(3):425–436, 1981.
- [60] Y.C. Fung. *Biomechanics: Mechanical Properties of Living Tissues*. Springer-Verlag New York, 1993.

-
- [61] Y.C. Fung. *Biodynamics: Circulation*. Springer Verlag, 1997.
- [62] M.A. Gallivan, D.R. Noble, J.G. Georgiadis, and R.O. Buckius. An evaluation of the bounce-back boundary condition for lattice Boltzmann simulations. *International Journal for Numerical Methods in Fluids*, 25(3):249–263, 1997.
- [63] M. Grassi, G. Pontrelli, L. Teresi, G. Grassi, L. Comel, A. Ferluga, and L. Galasso. Novel design of drug delivery in stented arteries: A numerical comparative study. *Mathematical Biosciences and Engineering (MBE)*, 6(3):493–508, 2009.
- [64] T. Grumann, P. Diehl, C. Bode, and M. Moser. Is stent thrombosis the new Achilles heel of interventional cardiology? State of the Art clinical trials, causes and approaches for prevention. *Hämostaseologie*, 27(5):344, 2007.
- [65] J. Gunn and D. Cumberland. Does stent design influence restenosis? *European Heart Journal*, 20(14):1009–1013, 1999.
- [66] W. Guo, C. Jin, and J. Li. High performance lattice Boltzmann algorithms for fluid flows. In *Proceedings of the 2008 International Symposium on Information Science and Engineering - Volume 01*, volume 1, 2008.
- [67] Z. Guo, C. Zheng, and B. Shi. An extrapolation method for boundary conditions in lattice Boltzmann method. *Physics of Fluids*, 14:2007, 2002.
- [68] Z. Guo, C. Zheng, and B. Shi. Non-equilibrium extrapolation method for velocity and pressure boundary conditions in the lattice Boltzmann method. *Chinese Physics*, 11:366–374, 2002.
- [69] Z.L. Guo and T.S. Zhao. Lattice Boltzmann model for incompressible flows through porous media. *The American Physical Society*, 66(3):1–9, 2002.
- [70] S. Hales. *Statical Essays: Containing Haemastaticks; or, An account of some Hydraulick and Hydrostatical Experiments made on the Blood and Blood Vessels of Animals*. W. Innys and R. Manby, London, 1733.
- [71] H. Hara, M. Nakamura, J.C. Palmaz, and R.S. Schwartz. Role of stent design and coatings on restenosis and thrombosis. *Advanced Drug Delivery Reviews*, 58(3):377–386, 2006.

- [72] X. He and D.N. Ku. Pulsatile flow in the human left coronary artery bifurcation: average conditions. *Journal of Biomechanical Engineering*, 118:74, 1996.
- [73] X. He and L.S. Luo. A priori derivation of the lattice Boltzmann equation. *Physical Review E*, 55(6):6333–6336, 1997.
- [74] X. He and L.S. Luo. Theory of the lattice Boltzmann method: From the Boltzmann equation to the lattice Boltzmann equation. *Physical Review E*, 56(6):6811–6817, 1997.
- [75] H. Hetterich. *Untersuchung biodegradierbarer Magnesiumstents mittels Angiographie, intravaskulärem Ultraschall und optischer Kohärenztomographie in Koronararterien*. PhD thesis, Ludwig-Maximilian-Universität München, 2010.
- [76] F.J. Higuera and J. Jimenez. Boltzmann approach to lattice gas simulations. *Europhysics Letters*, 9(7):663–668, 1989.
- [77] F.J. Higuera, S. Succi, and R. Benzi. Lattice gas dynamics with enhanced collisions. *Europhysics Letters*, 9:345–349, 1989.
- [78] M. Hirabayashi, M. Ohta, D.A. Rüfenacht, and B. Chopard. Characterization of flow reduction properties in an aneurysm due to a stent. *Physical Review E*, 68(2):21918, 2003.
- [79] M. Hirabayashi, M. Ohta, D.A. Rüfenacht, and B. Chopard. A lattice Boltzmann study of blood flow in stented aneurism. *Future Generation Computer Systems*, 20(6):925–934, 2004.
- [80] A.G. Hoekstra, J. van't Hoff, A.M. Artoli, and P.M.A. Sloot. Unsteady flow in a 2D elastic tube with the LBGK method. *Future Generation Computer Systems*, 20(6):917–924, 2004.
- [81] J. Horbach and D. Frenkel. Lattice-Boltzmann method for the simulation of transport phenomena in charged colloids. *Physical Review E*, 64(6):61507, 2001.
- [82] T. Inamuro, M. Yoshino, and F. Ogino. A non-slip boundary condition for lattice Boltzmann simulations. *Physics of Fluids*, 7:2928, 1995.

- [83] M. Junk, A. Klar, and L.S. Luo. Asymptotic analysis of the lattice Boltzmann equation. *Journal of Computational Physics*, 210(2):676–704, 2005.
- [84] Q. Kang, D. Zhang, and S. Chen. Displacement of a two-dimensional immiscible droplet in a channel. *Physics of Fluids*, 14:3203–3214, 2002.
- [85] R. Klinke and S. Silbernagl. *Lehrbuch der Physiologie*. Georg Thieme Verlag Stuttgart, 1994.
- [86] J. Koelman. A simple lattice Boltzmann scheme for Navier-Stokes fluid flow. *Europhysics Letters*, 15(6):603–607, 1991.
- [87] C. Körner, T. Pohl, U. Rude, N. Thurey, and T. Zeiser. Parallel lattice Boltzmann methods for CFD applications. *Lecture Notes in Computational Science and Engineering*, 51:439, 2005.
- [88] R. Kornowski, M.K. Hong, F.O. Tio, O. Bramwell, H. Wu, and M.B. Leon. In-stent restenosis: contributions of inflammatory responses and arterial injury to neointimal hyperplasia. *Journal of the American College of Cardiology*, 31(1):224–230, 1998.
- [89] M. Krafczyk, J. Tölke, E. Rank, and M. Schulz. Two-dimensional simulation of fluid-structure interaction using lattice-Boltzmann methods. *Computers and Structures*, 79(22-25):2031–2037, 2001.
- [90] J. Kropf. *Multiscale Blood Flow Modelling and Simulation*. PhD thesis, Vienna University of Technology, 2007.
- [91] D.N. Ku. Blood flow in arteries. *Annual Review of Fluid Mechanics*, 29(1):399–434, 1997.
- [92] D.N. Ku, D.P. Giddens, C.K. Zarins, and S. Glagov. Pulsatile flow and atherosclerosis in the human carotid bifurcation. Positive correlation between plaque location and flow oscillating shear stress. *Arteriosclerosis, Thrombosis, and Vascular Biology*, 5(3):293–302, 1985.
- [93] A.J.C. Ladd. Numerical simulations of particulate suspensions via a discretized Boltzmann equation. Part I. Theoretical foundation. *Journal of Fluid Mechanics*, 271:285–309, 1993.

-
- [94] A.J.C. Ladd. Numerical simulations of particulate suspensions via a discretized Boltzmann equation. Part II. Numerical results. *Journal of Fluid Mechanics*, 271:311–339, 2006.
- [95] P. Lallemand and L.S. Luo. Theory of the lattice Boltzmann method: Dispersion, dissipation, isotropy, Galilean invariance, and stability. *Physical Review E*, 61(6):6546–6562, 2000.
- [96] P. Lallemand and L.S. Luo. Lattice Boltzmann method for moving boundaries. *Journal of Computational Physics*, 184(2):406–421, 2003.
- [97] C. Lally, F. Dolan, and P.J. Prendergast. Cardiovascular stent design and vessel stresses: a finite element analysis. *Journal of Biomechanics*, 38(8):1574–1581, 2005.
- [98] J. Latt, B. Chopard, O. Malaspinas, M. Deville, and A. Michler. Straight velocity boundaries in the lattice Boltzmann method. *Physical Review E*, 77(5):56703, 2008.
- [99] D. Leitner. *Simulation of Arterial Blood Flow with the Lattice Boltzmann Method*. PhD thesis, Vienna University of Technology, 2007.
- [100] D. Leitner, S. Wassertheurer, and F. Breitenecker. A lattice Boltzmann model for pulsative flow in elastic vessels. *ARGESIM Report*, 30, 2006.
- [101] D. Leitner, S. Wassertheurer, M. Hessinger, A. Holzinger, and F. Breitenecker. Modeling elastic vessels with the LBGK method in three dimensions. *Lecture Notes in Computer Science*, 4799:213, 2007.
- [102] H. Li, X. Lu, H. Fang, and Y. Qian. Force evaluations in lattice Boltzmann simulations with moving boundaries in two dimensions. *Physical Review E*, 70(2):026701, 2004.
- [103] J. Lighthill. *Mathematical Biofluidynamics*. Society for Industrial and Applied Mathematics (Philadelphia), 1975.
- [104] J. Lighthill. *Waves in fluids*. Cambridge University Press, 1975.
- [105] A.L. Long, M.R. Sapoval, B.M. Beyssen, M.C. Auguste, Y. Le Bras, A.C. Ray-

- naud, G. Chatellier, and J.C. Gaux. Stretcher stent implantation in iliac arteries: patency and predictive factors for long-term success. *Radiology*, 194(3):739–744, 1995.
- [106] G.E. Loots. *Fluid-Structure Interaction in Hemodynamics*. PhD thesis, Rijksuniversiteit Groningen, 2003.
- [107] H.C. Lowe, S.N. Oesterle, and L.M. Khachigian. Coronary in-stent restenosis: current status and future strategies. *Journal of the American College of Cardiology*, 39(2):183–193, 2002.
- [108] B. Machenhauer. The spectral method. *Numerical methods used in atmospheric models*, 2(17):121–275, 1979.
- [109] A. Machraoui, P. Grewe, and A. Fischer. *Koronarstenting*. Steinkopff, 2001.
- [110] R.S. Maier, R.S. Bernard, and D.W. Grunau. Boundary conditions for the lattice Boltzmann method. *Physics of Fluids*, 8:1788, 1996.
- [111] C. Manwart, U. Aaltosalmi, A. Koponen, R. Hilfer, and J. Timonen. Lattice-Boltzmann and finite-difference simulations for the permeability for three-dimensional porous media. *Physical Reviews E*, 66:1–11, 2002.
- [112] B. Manz, L.F. Gladden, and P.B. Warren. Flow and dispersion in porous media: Lattice-Boltzmann and NMR studies. *AIChE Journal*, 45(9):1845–1854, 1999.
- [113] M.P. Marks, M.D. Dake, G.K. Steinberg, A.M. Norbash, and B. Lane. Stent placement for arterial and venous cerebrovascular disease: preliminary experience. *Radiology*, 191(2):441, 1994.
- [114] N.S. Martys and H. Chen. Simulation of multicomponent fluids in complex three-dimensional geometries by the lattice Boltzmann method. *Physical Review E*, 53(1):743–750, 1996.
- [115] A.H. Matsumoto, G.P. Teitelbaum, K.H. Barth, M.J. Carvlin, M.A. Savin, and E.P. Strecker. Tantalum vascular stents: in vivo evaluation with MR imaging. *Radiology*, 170(3):753–755, 1989.
- [116] J. Mazumdar. *Biofluid mechanics*. World Scientific, 1992.

-
- [117] M.D. Mazzeo and P.V. Coveney. HemeLB: A high performance parallel lattice-Boltzmann code for large scale fluid flow in complex geometries. *Computer Physics Communications*, 178(12):894–914, 2008.
- [118] D.A. McDonald. The relation of pulsatile pressure to flow in arteries. *The Journal of Physiology*, 127(3):533, 1955.
- [119] G.R. McNamara and G. Zanetti. Use of the Boltzmann equation to simulate lattice-gas automata. *Physical Review Letters*, 61(20):2332–2335, 1988.
- [120] R. Mei, L.S. Luo, and W. Shyy. An accurate curved boundary treatment in the lattice Boltzmann method. *Journal of Computational Physics*, 155:307–330, 2000.
- [121] R. Mei, W. Shyy, D. Yu, and L.S. Luo. Lattice Boltzmann method for 3-D flows with curved boundary. *Journal of Computational Physics*, 161(2):680–699, 2000.
- [122] R. Mei, D. Yu, W. Shyy, and L.S. Luo. Force evaluation in the lattice Boltzmann method involving curved geometry. *Physical Review E*, 65(4):041203, 2002.
- [123] S. Melchionna, M. Bernaschi, S. Succi, E. Kaxiras, F.J. Rybicki, D. Mitsouras, A.U. Coskun, and C.L. Feldman. Hydrokinetic approach to large-scale cardiovascular blood flow. *Computer Physics Communications*, 181(3):462–472, 2010.
- [124] W. Miller and S. Succi. A lattice Boltzmann model for anisotropic crystal growth from melt. *Journal of Statistical Physics*, 107(1):173–186, 2002.
- [125] W. Miller, S. Succi, and D. Mansutti. Lattice Boltzmann model for anisotropic liquid-solid phase transition. *Physical Review Letters*, 86(16):3578–3581, 2001.
- [126] W.R. Milnor. *Hemodynamics*. Williams & Wilkins, 1982.
- [127] K.W. Morton and D.F. Mayers. *Numerical Solution of Partial Differential Equations*. Cambridge University Press, 1994.
- [128] M. Nazemi and C. Kleinstreuer. Analysis of particle trajectories in aortic artery bifurcations with stenosis. *Journal of Biomechanical Engineering*, 111:311, 1989.
- [129] R.M. Nerem. Vascular fluid mechanics, the arterial wall, and atherosclerosis. *Journal of Biomechanical Engineering*, 114:274, 1992.

- [130] R.M. Nerem. Hemodynamics and the vascular endothelium. *Journal of Biomechanical Engineering*, 115:510, 1993.
- [131] N.Q. Nguyen and A.J.C. Ladd. Lubrication corrections for lattice-Boltzmann simulations of particle suspensions. *Physical Review E*, 66(4):46708, 2002.
- [132] W.W. Nichols and M. O'Rourke. *McDonald's Blood Flow in Arteries: Theoretical, Experimental and Clinical Principles*. Arnold, 1998.
- [133] X. Nie, Y.H. Qian, G.D. Doolen, and S. Chen. Lattice Boltzmann simulation of the two-dimensional Rayleigh-Taylor instability. *Physical Review E*, 58(5):6861–6864, 1998.
- [134] D.R. Noble, S. Chen, J.G. Georgiadis, and R.O. Buckius. A consistent hydrodynamic boundary condition for the lattice Boltzmann method. *Physics of Fluids*, 7:203, 1995.
- [135] D.R. Noble, J.G. Georgiadis, and R.O. Buckius. Comparison of accuracy and performance for lattice Boltzmann and finite difference simulations of steady viscous flow. *International Journal*, 23(1):1–18, 1996.
- [136] R.R. Nourgaliev, T.N. Dinh, T.G. Theofanous, and D. Joseph. The lattice Boltzmann equation method: theoretical interpretation, numerics and implications. *International Journal of Multiphase Flow*, 29(1):117–169, 2003.
- [137] H. Oertel and S. Ruck. *Bioströmungsmechanik: Grundlagen, Methoden und Phänomene*. Vieweg+Teubner Verlag, 2012.
- [138] R. Ouared and B. Chopard. Lattice Boltzmann simulations of blood flow: non-Newtonian rheology and clotting processes. *Journal of Statistical Physics*, 121(1):209–221, 2005.
- [139] J.C. Palmaz. Balloon-expandable intravascular stent. *American Journal of Roentgenology*, 150(6):1263–1269, 1988.
- [140] J.C. Palmaz. Intravascular stents: tissue-stent interactions and design considerations. *American Journal of Roentgenology*, 160(3):613–618, 1993.
- [141] J.C. Palmaz, S. Bailey, D. Marton, and E. Sprague. Influence of stent design

- and material composition on procedure outcome. *Journal of Vascular Surgery*, 36(5):1031–1039, 2002.
- [142] J.C. Palmaz, R.R. Sibbitt, S.R. Reuter, F.O. Tio, and W.J. Rice. Expandable intraluminal graft: a preliminary study. Work in progress. *Radiology*, 156(1):73–77, 1985.
- [143] C. Pan, J.F. Prins, and C.T. Miller. A high-performance lattice Boltzmann implementation to model flow in porous media. *Computer Physics Communications*, 158(2):89–105, 2004.
- [144] E.M. Pedersen, IB Kristensen, AP Yoganathan, et al. Wall shear stress and early atherosclerotic lesions in the abdominal aorta in young adults. *European Journal of Vascular and Endovascular Surgery*, 13(5):443–451, 1997.
- [145] T.J. Pedley. *The Fluid Mechanics of Large Blood Vessels*. Cambridge University Press, Cambridge, 1980.
- [146] K. Perktold and G. Rappitsch. Computer simulation of local blood flow and vessel mechanics in a compliant carotid artery bifurcation model. *Journal of Biomechanics*, 28(7):845–856, 1995.
- [147] C.S. Peskin. Numerical analysis of blood flow in the heart. *Journal of Computational Physics*, 25(3):220–252, 1977.
- [148] L.A. Pipes. *Applied Mathematics for Engineers and Physicists*. McGraw-Hill, 1958.
- [149] T. Pohl, M. Kowarschik, J. Wilke, K. Iglberger, and U. Rude. Optimization and profiling of the cache performance of parallel lattice Boltzmann codes. *Parallel Processing Letters*, 13(4):549–560, 2003.
- [150] G. Pontrelli. Pulsatile blood flow in a pipe. *Computers & Fluids*, 27(3):367–380, 1998.
- [151] G. Pontrelli. Nonlinear problems in arterial flows. *Nonlinear Analysis: Theory, Methods & Applications*, 47(7):4905–4915, 2001.
- [152] G. Pontrelli. A multiscale approach for modelling wave propagation in an arte-

- rial segment. *Computer Methods in Biomechanics and Biomedical Engineering*, 7(2):79–89, 2004.
- [153] G. Pontrelli and F. de Monte. Mass diffusion through two-layer porous media: an application to the drug-eluting stent. *International Journal of Heat and Mass Transfer*, 50(17):3658–3669, 2007.
- [154] G. Pontrelli and F. de Monte. Modeling of mass dynamics in arterial drug-eluting stents. *Journal of Porous Media*, 12(1):19–28, 2009.
- [155] G. Pontrelli and F. De Monte. A multi-layer porous wall model for coronary drug-eluting stents. *International Journal of Heat and Mass Transfer*, 53(19):3629–3637, 2010.
- [156] G. Pontrelli and E. Rossoni. Numerical modelling of the pressure wave propagation in the arterial flow. *International Journal for Numerical Methods in Fluids*, 43(6-7):651–671, 2003.
- [157] G. Pontrelli, S. Ubertini, and S. Succi. The unstructured lattice Boltzmann method for non-Newtonian flows. *Journal of Statistical Mechanics: Theory and Experiment*, 6:P06005, 2009.
- [158] D. Qi. Lattice-Boltzmann simulations of fluidization of rectangular particles. *International Journal of Multiphase Flow*, 26(3):421–433, 2000.
- [159] D. Qi. Simulations of fluidization of cylindrical multiparticles in a three-dimensional space. *International Journal of Multiphase Flow*, 27(1):107–118, 2001.
- [160] D. Qi and L.S. Luo. Transitions in rotations of a nonspherical particle in a three-dimensional moderate Reynolds number Couette flow. *Physics of Fluids*, 14:4440–4443, 2002.
- [161] D. Qi and L.S. Luo. Rotational and orientational behaviour of three-dimensional spheroidal particles in Couette flows. *Journal of Fluid Mechanics*, 477:201–213, 2003.
- [162] Y.H. Qian, D. d’Humières, and P. Lallemand. Lattice BGK models for Navier-Stokes equation. *Europhysics Letters*, 17(6):479–484, 1992.

-
- [163] Y.H. Qian and S.A. Orszag. Lattice BGK models for the Navier-Stokes equation: nonlinear deviation in compressible regimes. *Europhysics Letters*, 21(3):255–259, 1993.
- [164] Y.H. Qian and S.A. Orszag. Scalings in diffusion-driven reaction $A + B \rightarrow C$: Numerical simulations by lattice BGK models. *Journal of Statistical Physics*, 81(1):237–253, 1995.
- [165] A. Quarteroni and L. Formaggia. Mathematical modelling and numerical simulation of the cardiovascular system. *Handbook of Numerical Analysis*, 12:3–127, 2004.
- [166] C.M. Quick. Integrated arterial hemodynamics. Unpublished postdoctoral studies.
- [167] M.P. Rast. Simultaneous solution of the Navier-Stokes and elastic membrane equations by a finite element method. *International Journal for Numerical Methods in Fluids*, 19(12):1115–1135, 1994.
- [168] D. Rubenstein, W. Yin, and M.D. Frame. *Biofluid Mechanics: An Introduction to Fluid Mechanics, Macrocirculation, and Microcirculation*. Academic Press, 2011.
- [169] R.A. Schatz, J.C. Palmaz, F.O. Tio, F. Garcia, O. Garcia, and S.R. Reuter. Balloon-expandable intracoronary stents in the adult dog. *Circulation*, 76(2):450–457, 1987.
- [170] A.M. Shaaban and A.J. Duerinckx. Wall shear stress and early atherosclerosis: A review. *American Journal of Roentgenology*, 174(6):1657–1665, 2000.
- [171] U. Sigwart. Drug-eluting stents are safe and effective: right or wrong? *Journal of the American College of Cardiology*, 47(7):1361–1362, 2006.
- [172] U. Sigwart, J. Puel, V. Mirkovitch, F. Joffre, and L. Kappenberger. Intravascular stents to prevent occlusion and restenosis after transluminal angioplasty. *New England Journal of Medicine*, 316(12):701–706, 1987.
- [173] P.A. Skordos. Initial and boundary conditions for the lattice Boltzmann method. *Physical Review E*, 48(6):4823–4842, 1993.

- [174] M.A.A. Spaid and F.R. Phelan. Modeling void formation dynamics in fibrous porous media with the lattice Boltzmann method. *Composites Part A*, 29(7):749–755, 1998.
- [175] R.S. Stack, R.M. Califf, H.R. Phillips, D.B. Pryor, P.J. Quigley, R.P. Bauman, J.E. Tchong, and J.C. Greenfield Jr. Interventional cardiac catheterization at Duke Medical Center. *The American Journal of Cardiology*, 62:3F–24F, 1988.
- [176] J.D. Sterling and S. Chen. Stability analysis of lattice Boltzmann methods. *Journal of Computational Physics*, 123:196, 1993.
- [177] D. Stoeckel, C. Bonsignore, and S. Duda. A survey of stent designs. *Minimally Invasive Therapy and Allied Technologies*, 11(4):137–147, 2002.
- [178] E.P. Strecker, I.B. Boos, and B. Hagen. Flexible tantalum stents for the treatment of iliac artery lesions: long-term patency, complications, and risk factors. *Radiology*, 199(3):641–647, 1996.
- [179] E.P.K. Strecker, B. Hagen, D. Liermann, B. Schneider, H.R.D. Wolf, and J. Wambsganss. Iliac and femoropopliteal vascular occlusive disease treated with flexible tantalum stents. *Cardiovascular and interventional radiology*, 16(3):158–164, 1993.
- [180] S. Succi. *The Lattice Boltzmann Equation*. Oxford University Press, Oxford, 2001.
- [181] S. Succi, R. Benzi, and F. Higuera. The lattice boltzmann equation: a new tool for computational fluid-dynamics. *Physica D: Nonlinear Phenomena*, 47(1):219–230, 1991.
- [182] V.K. Sud and G.S. Sekhon. Simulation of steady cardiovascular flow in the presence of stenosis using a finite element method. *Physics in Medicine and Biology*, 35(7):947–959, 1990.
- [183] J. Suo, D.E. Ferrara, D. Sorescu, R.E. Guldberg, W.R. Taylor, and D.P. Giddens. Hemodynamic shear stresses in mouse aortas: implications for atherogenesis. *Arteriosclerosis, Thrombosis, and Vascular Biology*, 27(2):346, 2007.
- [184] H. Tahir, A.G. Hoekstra, E. Lorenz, P.V. Lawford, D.R. Hose, J. Gunn, and

- D.J.W. Evans. Multi-scale simulations of the dynamics of in-stent restenosis: impact of stent deployment and design. *Interface Focus*, 1(3):365–373, 2011.
- [185] M. Tamagawa and S. Matsuo. Predictions of thrombus formation using lattice Boltzmann method. *JSME International Journal Series C*, 47(4):1027–1034, 2004.
- [186] H. Tamai, K. Igaki, E. Kyo, K. Kosuga, A. Kawashima, S. Matsui, H. Komori, T. Tsuji, S. Motohara, and H. Uehata. Initial and 6-month results of biodegradable poly-l-lactic acid coronary stents in humans. *Circulation*, 102(4):399–404, 2000.
- [187] C.A. Taylor, T.J.R. Hughes, and C.K. Zarins. Finite element modeling of blood flow in arteries. *Computer Methods in Applied Mechanics and Engineering*, 158(1-2):155–196, 1998.
- [188] C.A. Taylor, T.J.R. Hughes, and C.K. Zarins. Finite element modeling of three-dimensional pulsatile flow in the abdominal aorta: relevance to atherosclerosis. *Annals of Biomedical Engineering*, 26(6):975–987, 1998.
- [189] P.R.F. Teixeira and A.M. Awruch. Numerical simulation of fluid–structure interaction using the finite element method. *Computers & fluids*, 34(2):249–273, 2005.
- [190] B. Thierry and M. Tabrizian. Biocompatibility and biostability of metallic endovascular implants: state of the art and perspectives. *Journal of Endovascular Therapy*, 10(4):807–824, 2003.
- [191] J. Tölke, M. Krafczyk, M. Schulz, and E. Rank. Lattice Boltzmann simulations of binary fluid flow through porous media. *Philosophical Transactions: Mathematical, Physical and Engineering Sciences*, 360:535–545, 2002.
- [192] A. Veneziani. *Mathematical and Numerical Modelling of Blood Flow Problems*. PhD thesis, Politecnico di Milano, 1998.
- [193] S.S. Venkatraman, L.P. Tan, J.F.D. Joso, Y.C.F. Boey, and X. Wang. Biodegradable stents with elastic memory. *Biomaterials*, 27(8):1573–1578, 2006.
- [194] R. Verberg and A.J.C. Ladd. Simulation of low-Reynolds-number flow via a

- time-independent lattice-Boltzmann method. *Physical Review E*, 60(3):3366–3373, 1999.
- [195] R. Verberg and A.J.C. Ladd. Lattice-Boltzmann model with sub-grid-scale boundary conditions. *Physical Review Letters*, 84(10):2148–2151, 2000.
- [196] R. Verberg and A.J.C. Ladd. Accuracy and stability of a lattice-Boltzmann model with subgrid scale boundary conditions. *Physical Review E*, 65(1):16701, 2001.
- [197] A.K. Wakhloo, F.O. Tio, B.B. Lieber, F. Schellhammer, M. Graf, and L.N. Hopkins. Self-expanding nitinol stents in canine vertebral arteries: hemodynamics and tissue response. *American Journal of Neuroradiology*, 16(5):1043–1051, 1995.
- [198] W.A. Wall. *Fluid-Struktur-Interaktion mit stabilisierten Finiten Elementen*. PhD thesis, Universität Stuttgart, 1999.
- [199] J. Wang, X. Zhang, A.G. Bengough, and J.W. Crawford. Domain-decomposition method for parallel lattice Boltzmann simulation of incompressible flow in porous media. *Physical Review E*, 72(1):016706, 2005.
- [200] G. Wellein, T. Zeiser, G. Hager, and S. Donath. On the single processor performance of simple lattice Boltzmann kernels. *Computers and Fluids*, 35(8-9):910–919, 2006.
- [201] J. Wilke, T. Pohl, M. Kowarschik, and U. Rude. Cache performance optimizations for parallel lattice Boltzmann codes. *Lecture Notes in Computer Science*, 2790:441–450, 2003.
- [202] D.A. Wolf-Gladrow. *Lattice-Gas Cellular Automata and Lattice Boltzmann Models: An Introduction*. Springer, 2000.
- [203] J.R. Womersley. Method for the calculation of velocity, rate of flow and viscous drag in arteries when the pressure gradient is known. *The Journal of Physiology*, 127(3):553, 1955.
- [204] J.R. Womersley. XXIV. Oscillatory motion of a viscous liquid in a thin-walled elastic tube – I: The linear approximation for long waves. *Philosophical Magazine Series 7*, 46(373):199–221, 1955.

- [205] J.R. Womersley. Oscillatory flow in arteries: the constrained elastic tube as a model of arterial flow and pulse transmission. *Physics in Medicine and Biology*, 2:178–187, 1957.
- [206] K.C. Wright, S. Wallace, C. Charnsangavej, C.H. Carrasco, and C. Gianturco. Percutaneous endovascular stents: an experimental evaluation. *Radiology*, 156(1):69–72, 1985.
- [207] X. Wu, V. Taylor, S. Garrick, D. Yu, and J. Richard. Performance analysis, modeling and prediction of a parallel multiblock lattice Boltzmann application using prophesy system. In *IEEE Conference on Cluster Computing*, 2006.
- [208] X. Xu and J.S. Lee. Application of the lattice Boltzmann method to flow in aneurysm with ring-shaped stent obstacles. *International Journal for Numerical Methods in Fluids*, 59:691–710, 2009.
- [209] K. Yamamoto, X. He, and G.D. Doolen. Simulation of combustion field with lattice Boltzmann method. *Journal of statistical physics*, 107(1):367–383, 2002.
- [210] C.J. Yoon, J.W. Chung, J.H. Park, S.H. Hong, S.Y. Song, H.G. Lim, and Y.S. Lee. A newly designed nitinol stent: early clinical experience in the treatment of iliac artery stenoses and occlusions. *Korean Journal of Radiology*, 2(3):145–150, 2001.
- [211] D. Yu, R. Mei, L.S. Luo, and W. Shyy. Viscous flow computations with the method of lattice Boltzmann equation. *Progress in Aerospace Sciences*, 39(5):329–367, 2003.
- [212] D. Yu, R. Mei, and W. Shyy. A multi-block lattice Boltzmann method for viscous fluid flows. *International Journal for Numerical Methods in Fluids*, 39:99–120, 2002.
- [213] M. Zamir. *The Physics of Pulsatile Flow*. Springer, New York, 2000.
- [214] C.K. Zarins, D.P. Giddens, B.K. Bharadvaj, V.S. Sottiurai, R.F. Mabon, and S. Glagov. Carotid bifurcation atherosclerosis. Quantitative correlation of plaque localization with flow velocity profiles and wall shear stress. *Circulation Research*, 53(4):502–514, 1983.

-
- [215] X. Zhang, A.G. Bengough, J.W. Crawford, and I.M. Young. A lattice BGK model for advection and anisotropic dispersion equation. *Advances in Water Resources*, 25(1):1–8, 2002.
- [216] D.P. Ziegler. Boundary conditions for lattice Boltzmann simulations. *Journal of Statistical Physics*, 71(5):1171–1177, 1993.
- [217] O.C. Zienkiewicz and R.L. Taylor. *The Finite Element Method for Solid and Structural Mechanics*, volume 2. Butterworth-Heinemann, 2005.
- [218] C.L. Zollikofer, F. Antonucci, M. Pfyffer, F. Redha, E. Salomonowitz, G. Stuckmann, I. Largiader, and A. Marty. Arterial stent placement with use of the Wallstent: midterm results of clinical experience. *Radiology*, 179(2):449–456, 1991.
- [219] C.L. Zollikofer, F. Antonucci, G. Stuckmann, P. Mattias, and E.K. Salomonowitz. Historical overview on the development and characteristics of stents and future outlooks. *Cardiovascular and Interventional Radiology*, 15(5):272–278, 1992.
- [220] Q. Zou and X. He. On pressure and velocity boundary conditions for the lattice Boltzmann BGK model. *Physical Fluids*, 9:1591–1598, 1997.

Curriculum Vitae

Personal information

| | |
|---------------|-------------------------------|
| Name | Xenia Descovich |
| Date of birth | May 8, 1983 |
| Nationality | Austria |
| Address | Hadikgasse 146/6 1140 Wien |

Education

| | |
|-----------------|--|
| since 10/2008 | Vienna University of Technology Doctoral program in Technical Sciences |
| 10/2001-06/2008 | Vienna University of Technology Diploma studies in Technical Mathematics Branch of study: Mathematics in Natural Sciences |
| 09/1988-06/2001 | Lycée Français de Vienne Primary and secondary education |

Work experience

| | |
|---------------|---|
| since 10/2008 | AIT Austrian Institute of Technology GmbH Health & Environment Department, Biomedical Systems Research Fellow, PhD Student |
|---------------|---|

| | |
|--|---|
| 11/2010-02/2011, 11/2011, 03/2012, 06/2012 | Consiglio Nazionale delle Ricerche, Rome Istituto per le Applicazioni del Calcolo Research Cooperation |
| since 03/2010 | Vienna University of Technology Institute of Analysis and Scientific Computing University Lecturer |
| 10/2008-02/2010 | Vienna University of Technology Institute of Analysis and Scientific Computing Teaching Assistant |

Language skills

| | |
|----------------|--|
| German | Native language |
| French | Fluently spoken and written (French <i>baccalauréat général</i> high school degree) |
| English | Fluently spoken and written |
| Czech | Basic knowledge |
| Italian | Basic knowledge |